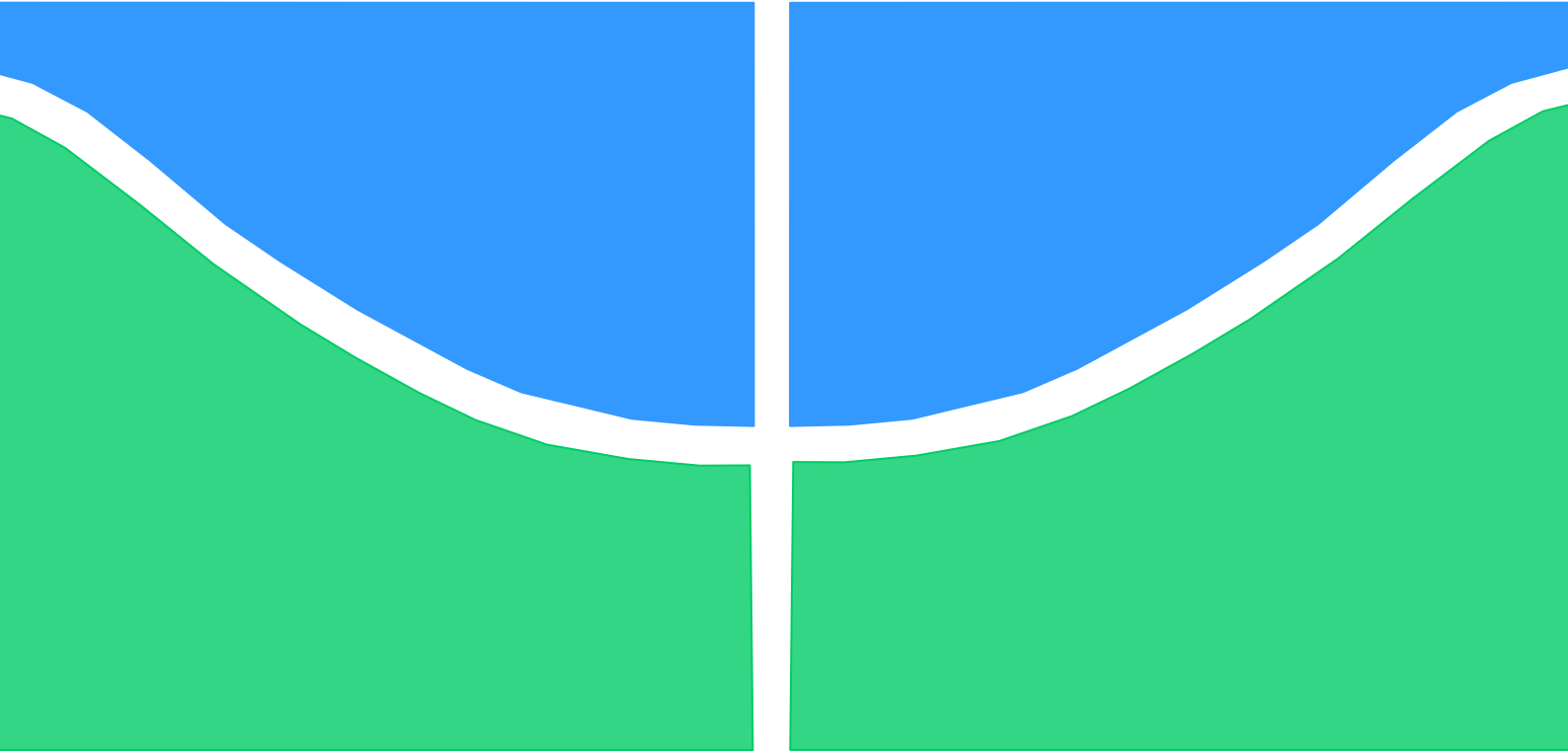

MASTER OF SCIENCE IN MECHANICAL ENGINEERING

EXTRACTION OF PLASTICITY PARAMETERS OF METALLIC MATERIALS FROM SPHERICAL INDENTATION TESTS AND FEM MODELLING

BY

LUCAS QUEIROZ MACHADO

UNIVERSITY OF BRASÍLIA

FACULTY OF TECHNOLOGY

MECHANICAL ENGINEERING DEPARTMENT

UNIVERSITY OF BRASÍLIA
FACULTY OF TECHNOLOGY
MECHANICAL ENGINEERING DEPARTMENT

MASTER OF SCIENCE IN MECHANICAL ENGINEERING

EXTRACTION OF PLASTICITY PARAMETERS OF METALLIC MATERIALS FROM SPHERICAL INDENTATION TESTS AND FEM MODELLING

A Dissertation
Presented to
The Faculty of Technology

by

Lucas Queiroz Machado

In Partial Fulfillment
of the Requirements for the Degree of
Master of Science in Mechanical Engineering
at the
UNIVERSITY OF BRASÍLIA / MECHANICAL ENGINEERING DEPARTMENT

PUBLICAÇÃO: ENM.DM - 300/2019

BRASÍLIA-DF: JANUARY - 2019

UNIVERSITY OF BRASÍLIA
FACULTY OF TECHNOLOGY
MECHANICAL ENGINEERING DEPARTMENT

MASTER OF SCIENCE IN MECHANICAL ENGINEERING

EXTRACTION OF PLASTICITY PARAMETERS OF METALLIC MATERIALS FROM SPHERICAL INDENTATION TESTS AND FEM MODELLING

Approved by:

Prof. Lucival Malcher, DSc. - Supervisor
ENM-FT-UnB
University of Brasília

Prof. Luciano Mendes Bezerra, Ph.D. - External Examiner
ENC-FT-UnB
University of Brasília

Prof. Fábio Comes de Castro, DSc. - Internal Examiner
ENM-FT-UnB
University of Brasília

BRASÍLIA-DF, 10 JANUARY 2019

FICHA CATALOGRÁFICA

MACHADO, LUCAS QUEIROZ

EXTRACTION OF PLASTICITY PARAMETERS OF METALLIC MATERIALS FROM SPHERICAL INDENTATION TESTS AND FEM MODELLING.

xvii, 84p., 210 x 297 mm (ENM/FT/UnB, Mestre, Ciências Mecânicas, 2019)

Dissertação de Mestrado – Universidade de Brasília, Faculdade de Tecnologia.

Departamento de Engenharia Mecânica.

1. Indentation Test
2. Parameter Identification
3. Multi-Image Analysis
4. Stress-Strain Curve
5. Optimization Process
6. Inverse Method

I. ENM/FT/UnB

II. Título (série)

REFERÊNCIA BIBLIOGRÁFICA

MACHADO, L. Q (2019). Extraction of Plasticity Parameters of Metallic Materials from Spherical Indentation Tests and FEM Modelling. Dissertação de Mestrado em Ciências Mecânicas, Publicação ENM.DM – 300/2019, Departamento de Engenharia Mecânica, Universidade de Brasília, DF, 84p.

CESSÃO DE DIREITOS

AUTOR: Lucas Queiroz Machado.

TÍTULO: Extraction of Plasticity Parameters of Metallic Materials from Spherical Indentation Tests and FEM Modelling.

GRAU: Mestre ANO: 2019

Lucas Queiroz Machado

lucasqmachado@gmail.com

BRASÍLIA-DF

To the Creator of all things, the Eternal and endlessly loving God

ACKNOWLEDGEMENTS

I would like to thank God for guiding my path and giving me much more than I can ask or imagine.

I would like to express my very great appreciation to my supervisor Professor Lucival Malcher for his guidance, enthusiastic encouragement, and all the opportunities that he created to benefit me.

My special thanks to my parents Antonio Machado and Maria José Machado for all the support, counseling, and for always being close to me.

I would like to thank my dear girlfriend for all her love, encouragement, help, and for making this trajectory more enjoyable.

I would like to thank my siblings Fernanda, Jeftali, Suzana, Cecília, Júlio, and Pedro for always having a great expectation about me and giving their best to help me.

I am particularly grateful for the assistance provided by Professor Thiago Doca for his valuable and constructive suggestions on the development of the FEM model.

I would like to thank MSc Leonel Morales and UDF for providing and manufacturing some of the specimens used in this work.

I wish to thank B.Eng. Pedro Rocha, MSc. Guilherme Ferreira, MSc. Felipe Canut, MSc Raniere Neves, MSc. Maycol Coutinho, and MSc. Cainã de Barros for all their help and constructive recommendations on this project.

I would also like to extend my thanks to the technicians of the laboratory for their help in processing the samples.

I wish to thank my church family, the SDA Ponte Alta Norte-DF, for all the prayers.

I am grateful to UnB, CAPES, and FAPDF for the financial support in the development of this project.

TABLE OF CONTENTS

LIST OF TABLES

LIST OF FIGURES

LIST OF SYMBOLS AND ABBREVIATIONS

Latin Letters

A_0	Initial cross-sectional area
A_i	Current cross-sectional area
a_c	Contact radius
a_p	Plastic radius
C	Indentation loading constant
c	Pile-up/sink-in indicator
D	Indenter diameter
d	Approach of two remote points
d_i	Indentation diameter
$\mathbb{D}$	Elastic modulus tensor
E	Young's modulus
E_{eq}	Equivalent Young's modulus
$f(\boldsymbol{p})$	Objective function
$\boldsymbol{H}$	Generalized hardening modulus
$\boldsymbol{H}_k$	Hessian matrix
H	Hardening modulus
h	Indentation depth
h_f	Final indentation depth
h_{max}	Maximum indentation depth
h_r	Surface displacement
I_1, I_2, I_3	Stress tensor invariants
J_1, J_2, J_3	Deviatoric stress tensor invariants
m	Indentation loading constant
m_k	Objective function model
$\mathbf{N}$	Flow vector
n	Hardening exponent
P	Applied load
P_Y	Load associated with initial yielding
P_{max}	Applied maximum load
P_m	Mean contact pressure

p	Pressure distribution
$\boldsymbol{p}$	Parameters
p_0	Peak contact pressure
p_{0_Y}	Peak contact pressure associated with initial yielding
R_{eq}	Equivalent radius
$\boldsymbol{R}_i^{FEM}$	FEM response
$\boldsymbol{R}_i^{EXP}$	Experimental response
r	Radial coordinate
$\boldsymbol{S}$	Deviatoric stress tensor
S	Indentation unloading stiffness
$\boldsymbol{s}$	Trial step of the optimization problem
s	Pile-up/sink-in height
W^p	Plastic work

Greek Letters

β	Indentation contact angle
Γ	Johnson parameter
$\dot{\gamma}$	Plastic multiplier
$\boldsymbol{\varepsilon}$	Strain tensor
$\boldsymbol{\varepsilon}^e$	Elastic strain tensor
$\boldsymbol{\varepsilon}^p$	Plastic strain tensor
$\boldsymbol{\varepsilon}_d^e$	Deviatoric strain tensor
ε_v^e	Volumetric strain
$\bar{\varepsilon}^{\boldsymbol{p}}$	Effective (or accumulated) plastic strain
ε_{rep}	Representative strain
ε	Engineering strain
$\bar{\varepsilon}$	True strain
μ	Friction coefficient
$\boldsymbol{\sigma}$	Cauchy stress tensor
$\sigma_1, \sigma_2\ e\ \sigma_3$	Principal stresses
$\sigma_{xx}, \sigma_{yy}, \sigma_{zz}$	Stress components
σ_y	Yield stress
σ_{y0}	Initial yield stress.

σ_{rep}	Representative stress
σ_{eq}	von Mises equivalent stress
σ	Engineering stress
$\bar{\sigma}$	True stress
σ_{y0}, ξ, σ_{∞}, δ	Kleinermann-Ponthot's hardening parameters
υ	Poisson's ratio
Φ	Yield function
Ψ	Plastic constraint factor
Λ	Flow potential
Ω_k	Trust region

Acronyms

ABNT	Associação Brasileira de Normas Técnicas
ASTM	American Society for Testing and Materials
CAX4R	4-node bilinear axisymmetric quadrilateral, reduced integration, hourglass control
CAX4	4-node bilinear axisymmetric quadrilateral
IRC	Indentation Reaction Curve approach
IP	Indentation Profile approach

ABSTRACT

The plastic behavior of a metallic material is resultant of non-linearities which leads to complex stress-strain fields, making it difficult to devise analytical relationships beyond the elastic domain. Traditionally, the material's stress-strain relationship has been acquired from uniaxial testing, which is widely used to describe its behavior under plastic deformation. However, there are samples that due to their configurations cannot be tested using the uniaxial tensile test. Furthermore, the hardness test is more versatile, operative, cheaper, and faster than the uniaxial test. When it comes to traditional hardness tests, such as in the Brinell, Knoop, Rockwell, and Vickers, they have been mostly used as a way to assess the capability a material has to resist plastic deformation. They relate the applied load to the resultant area or depth of indentation impressed in the material. The technique developed and presented here has gone beyond that by determining other material properties in addition to hardness. Therefore, this work presents two approaches to describe the hardening behavior of metallic materials from indentation hardness tests. The Brinell hardness test is the chosen method due to its simplicity and versatility. The methodology consists of performing three Brinell hardness tests in three distinct configurations, to have a representative material's response. A multi-image analysis of the indention impressions is performed in a confocal laser microscope, providing the experimental indentation responses. They are obtained to be a reference which with the predicted output of repeated FEM modeling is compared. In this process, several trial stress-strain curves are provided to minimize the discrepancy between numerical and experimental data in an iterative FEM modeling of the indentation process. The process runs until reaching the established tolerance and thus providing the hardening parameters that best fit the experimental data. As mentioned, two approaches were developed. The first, designated as Indentation Reaction Curve (IRC) approach, numerically replicates the load-final depth response of an experimental indentation test. The second, designated as Indentation Profile (IP) approach, numerically replicates the same indentation impressions left in the specimen by the indenter in an experimental indentation test. To facilitate the use of this resource by other users, a user-friendly interface was also built. A tutorial on how to use it is included in APPENDIX A. Lastly, the hardening curves obtained from uniaxial tests and the approaches presented here are compared. Four materials were analyzed: the SAE 1524, SAE 4340 A (annealed), SAE 4340 N (normalized), and Aluminum 6101. Their parameters were determined by IRC, IP, and tensile test approaches. However, with exception for the SAE 1524, the results showed that the curves obtained from uniaxial tensile tests for these materials were not adequate to use in compressive analyses because they were not able to predict the experimental indentation responses. Consequently, the hardening curves obtained from IRC and IP approaches did not match those from uniaxial tensile tests for the SAE 4340 A, SAE 4340 N, and Aluminum 6101. The hypothesis assumed is that these materials present distinct behavior under tension and compression.

Keywords: *parameter identification, indentation test, indentation multi-image analysis, stress-strain curve, optimization process.*

RESUMO

O comportamento plástico de materiais metálicos é resultante de não linearidades que conduzem a complexos campos de tensão-deformação. Isso torna difícil o desenvolvimento de relações analíticas aplicáveis além do domínio elástico. Tradicionalmente, a relação tensão-deformação da maioria dos materiais tem sido adquirida a partir de ensaios uniaxiais de tração, que é largamente utilizado para descrever seu comportamento quando submetido à deformação plástica. Entretanto, há certos componentes materiais que devido à sua configuração não podem ser ensaiados por ensaios uniaxiais de tração ou compressão. Além do mais, o ensaio de dureza é mais versátil, operativo, barato e rápido que os ensaios uniaxiais. Quando se fala em ensaios tradicionais de dureza, tais como Brinell, Knoop, Rockwell e Vickers, eles são majoritariamente utilizados como uma forma de avaliar a resistência do material à deformação plástica. Eles relacionam o carregamento aplicado à resultante área ou profundidade da calota impressa no material. As técnicas desenvolvidas e apresentadas aqui vão além ao determinar outras propriedades materiais em adição à medida de dureza. Portanto, este trabalho apresenta dois métodos para descrever o comportamento de endurecimento de materiais metálicos a partir de ensaios de dureza. O ensaio de dureza Brinell é o método escolhido devido sua simplicidade e versatilidade. A metodologia consiste na execução de três ensaios de dureza Brinell em três configurações distintas, para se ter uma resposta representativa do material. Análises de imagem da impressão resultante do ensaio de dureza são realizadas com o auxílio de microscópio confocal à laser. Daí são obtidas as respostas experimentais do material. Desta análise são extraídas as medidas dos perfis da calota impressa no material, as quais serão utilizadas como referência para os resultados numéricos previstos pela repetitiva análise em elementos finitos. Neste processo, várias tentativas de curvas tensão-deformação são providas com o intuito de minimizar a discrepância entre as respostas numérica e experimental. Como mencionado, dois métodos foram desenvolvidos. O primeiro é designado como IRC (Indentation Reaction Curve) e replica numericamente a resposta de carga-profundidade final obtida experimentalmente. O segundo método, designado como IP (Indentation Profile), replica numericamente as impressões deixadas no corpo de prova pelo teste de dureza. Para facilitar o uso deste recurso por outros usuários, uma interface gráfica foi construída. Um tutorial sobre seu uso é também anexado a este trabalho. Por fim, as curvas de encruamento obtidas a partir de ensaio de tração e pelos métodos apresentados aqui são comparadas. Quatro materiais foram analisados: SAE 1524, SAE 4340 N (normalizado), SAE 4340 A (recozido), e Alumínio 6101. Seus parâmetros plásticos foram determinados pelos métodos IRC, IP e por ensaio de tração. Entretanto, com exceção do SAE 1524, os resultados mostram que as curvas obtidas a partir do ensaio uniaxial de tração para esses materiais não são adequadas para uso em análises compressivas, devido ao fato de não serem capazes de prever as respostas experimentais de indentação. Consequentemente, as curvas de endurecimento obtidas a partir dos métodos IRC e IP não correspondem àquelas obtidas a partir do ensaio de tração para o SAE 4340 N, SAE 4340 A, e Alumínio 6101. A justificativa para essa ocorrência é de que esses materiais apresentam comportamentos distintos sobre tração e compressão.

Palavras-chave: *Identificação paramétrica, perfis de calotas esféricas, curva tensão-deformação, ensaio de dureza, processo de otimização.*

CHAPTER 1. INTRODUCTION

1.1 Background and motivation

Indentation hardness tests have been traditionally understood as a way to assess the capability a material has to resist plastic deformation by relating the applied load to the resultant area or depth of indentation, such as in Brinell, Knoop, Rockwell and Vickers hardness tests (Chandler, 1999). Over the past years, new techniques have been devised for probing the mechanical properties of materials by indentation tests. This is mainly due to the development of instruments able to provide the indentation load-displacement data. Properties such as the Young's modulus and Poisson's Ratio can be directly extracted by continuously measuring the depth of indentation while a normal load is being applied in the material. Thanks to numerical methods, such as the Finite Element Method, the determination of material hardening parameters by inverse analyses using indentation tests has become possible (Oliver and Pharr, 1992; Guillonneau *et al.*, 2012; Kang, 2013; Dean and Clyne, 2017).

The increasing scientific knowledge has enabled engineers to elaborate solutions for practical problems and, as result of that, they have a greater number of tools and resources that can help in the problem solving and comprehension of science. The understanding of the mechanical behavior of ductile materials is closely tied to the development of many devices that facilitate the life of many. It greatly induces progress in several sectors of the industry, such as transportation, housing, communication, safety, clothing, food production, and sports.

Launching a new product into the market requires careful planning in several areas, from its conception to its installation and operation. It happens due to the perception that scientific methods have great potential to provide functionality with low manufacturing costs. Therefore, the selection of the material to be applied in an engineering project is an important decision for the designer, especially when the material undergoes plastic deformation.

The increasing interest in optimizing manufacturing processes has stimulated the important development of methodologies for obtaining stress-strain curves from indentation tests to provide a more versatile and convenient way to extract the material's plasticity parameters (Oliver and Pharr, 1992; Giannakopoulos and Suresh, 1999; Bucaille *et al.*, 2003; Bobzin *et al.*, 2013; Kang, 2013; Njeugna *et al.*, 2016). The uniaxial test is traditionally performed to determine several material properties such as the plasticity parameters. However, difficulties arise in this method when the amount of material available is not enough to manufacture the specimen.

The indentation test approach is also justified when other uniaxial test limitations are exposed: first, it requires a standard specimen, which brings costs spending funds and time to manufacture it; and

second, the specimen can only be used once since the uniaxial test is destructive. These two conditions make the parameter identification process more expensive and thus incite the development of new methodologies to perform the same task. Having the situation exposed, the indentation test is suggested to replace the traditional uniaxial test in the parameter identification task, providing versatility and convenience, since it is simple, cheap and the same specimen can be used several times for micro indentations.

The link between indentation tests and the stress-strain curve of the material is seen, for example, when this stress-strain relationship is inserted into numerical models to simulate contact problems. Assuming that this curve can be multiaxially applied to the deviatoric components of stress and strain (von Mises), it is possible to predict the mechanical behavior of an indented material and extract its load-depth response and the resultant indentation geometry. This work, however, presents the inverse problem, i.e., inferring the stress-strain relationship from experimental responses of a material to indentation tests.

The extraction of the stress-strain relationship of the material is performed by repetitive FEM analysis. In principle, several stress-strain curves are generated until the best fit between predicted and experimental responses is given. To produce the stress-strain curve, the Kleinermann-Ponthot (2003) constitutive model is adopted. It is defined by four plasticity parameters; thus, they are the variables to be optimized. For this, a methodology coupling FEM modeling and optimization approach was developed. To a great extent, the efficiency of the method relies on the efficiency of the optimization algorithm, since it conducts the whole process.

Instrumented indentation devices, usually used for similar purposes, are not available. Consequently, the collection of rich indentation data, such as the loading-unloading curve, was not possible. However, the method and all the algorithms developed here are applicable to extract the plasticity parameters using the loading-unloading information as the target curve. Instead of an instrumented indentation device, a universal hardness machine is used. It has a wide range of applicable loads and indenter sizes. From it, two experimental indentation responses are obtained, which will be used as the target information during the optimization process. The first relates the applied load to the final indentation depth while the second relates the applied load to the indentation profile extracted from a laser confocal microscope. The load-final depth response was primarily thought to give a good start for the development of the technique. Using the profile as the target information comes as a refinement of the method since it provides other contact parameters that are related to the hardening behavior of the material.

Therefore, two approaches for the extraction of plasticity parameters of metallic materials are provided. They are designed according to the target experimental data used in the process as the Indentation Reaction Curve (IRC) approach and the Indentation Profile (IP) approach. By them, four

materials are evaluated: the SAE 1524, SAE 4340 N, the SAE 4340 A, and the Aluminum 6101, where N stands for normalized and A for Annealed.

1.2 Research Aims

The aim of this work is to provide a sound methodology for extraction of plasticity parameters of metallic materials. Toward this aim, several distinct goals are established building up to the overall proposal fulfillment:

1. The development of a numerical model for the indentation test in python to be read by Abaqus.

2. Understanding the material response to indentation under different contact conditions, e.g. for distinct friction coefficients, contact formulation, and meshing.

3. Adoption of an optimization algorithm and the establishment of communication between it and the FE model.

4. Evaluation of the capability of the methodology by comparing the hardening curves extracted from it with the ones obtained from the uniaxial tensile tests.

5. The development of a friendly-user interface to facilitate the use of the methodology by other users in the task of extracting material plasticity parameters of metallic materials from indentation tests.

1.3 Outline

This dissertation is dived into six chapters, a conclusion and two appendices. Each chapter is divided into subsections to provide a clear understanding of the distinct processes involved in the development of this work. A brief outline is given below:

CHAPTER 1 introduces the subjects addressed in this work. It includes a brief comment on the indentation background and on the aspects that motivated the development of the technique proposed here. It establishes a connection between the indentation techniques and the extraction of the plasticity parameters from its responses. Lastly, it gives an overview of the numerical aspects and experimental shortcomings presented in this analysis.

CHAPTER 2 addresses the elastic-plastic contact in a didactic path starting from the description of the Hertzian contact up to recent theoretical conclusions about indentations in the full-plasticity regime. It introduces the concept of representative stress-strain, which analytically correlates indentations experiments with the traditional uniaxial test. It also presents the main phenomena related to the indentation experiment, such as the shallowing effect and pile-up/sink-in. The theoretical relationships of the constitutive formulation adopted is presented. It describes the evolution laws for the elastic-plastic behavior of most metals.

CHAPTER 3 describes the experimental procedures adopted to promote and evaluate the methodologies presented here. First, the uniaxial tensile test is depicted showing all the steps for the extraction of the plasticity parameters by its means. Second, the Brinell hardness test is addressed. This is the test used to generate the target information to be compared with the FEM output.

CHAPTER 4 presents the indentation FEM model built for this analysis. It is depicted as it was built in ABAQUS, showing all the procedures and considerations for the analysis. It included decisions on contact formulation, frictional effects, and meshing, for example.

CHAPTER 5 uses empirical analytical formulations as a tentative to correlate indentation tests to the stress-strain data obtained from uniaxial tests. The experimental data extracted in CHAPTER 3 are then used to obtain the indentation parameters necessary for the analytical relationships. Representative stress-strain points are obtained from that which are plotted against the stress-strain curves obtained from traditional uniaxial tensile tests.

CHAPTER 6 is the main point of this work. Here, the two approaches are explained in detail and applied for four different materials. They both are, in general, a curve fitting process. In this, experimental resultant data is continually compared with the numerical output for different sets of plasticity parameters provided in the optimization process. The optimum plasticity parameters are determined once the best fit between numerical and experimental data has been provided. With this done, the optimum plasticity parameters are inserted in their respective constitutive model and the material stress-strain curve is generated. It is then compared with the ones obtained from traditional uniaxial tensile tests.

The Conclusion is presented making an overall consideration of the two approaches developed here for the extraction of plasticity parameters of metals. Their efficiency and limitations are compared based on the results obtained. It states the hypotheses for the discrepancies in the analysis and suggests how the methodology could be better assessed considering the compressive nature of the indentation test. It also mentions the shortcomings of the optimization algorithm adopted and points out solutions to be added to the optimization routine.

APPENDIX A is a brief tutorial of the user-friendly interface built to spread the use of this technique by other researchers and students. APPENDIX B shows the optimization routine adopted.

CHAPTER 2. ELASTIC-PLASTIC CONTACT

In several industrial applications, it is essential to predict the mechanical behavior of bodies that are brought into contact. It ranges from rollers and bearings to ultrasonic welding. Therefore, there has been an increasing focus on understanding and describing the nature of contact mechanics. Here, it is presented three main inquiries related to the body's reaction to an applied load. They encompass the resultant shape of the contact area and how it grows, the magnitude and distribution of the surface tractions across the interface and how to obtain the stress and strain fields in the vicinity of the contact region. When it comes to a frictionless and fully-elastic contact interaction, the mechanics of contacts are well known and described by Hertz (1881). However, a complete analytical solution for contact problems involving yielding has not yet been achieved (Hills, 1983).

2.1 Hertzian Contact

Hertz developed the analytical solution for the contact between two elastic bodies whose profiles can be described by a smooth surface. Here, the sphere-flat contact pair will be exclusively addressed, since the scope of this work is about ball indentation tests. The sphere-on-flat contact configuration can be studied from the perspective of the contact of two spheres (Figure 1), where one of them has an infinite radius of curvature and, thus, is a true half space (Hills, Nowell and Sackfield, 1993).

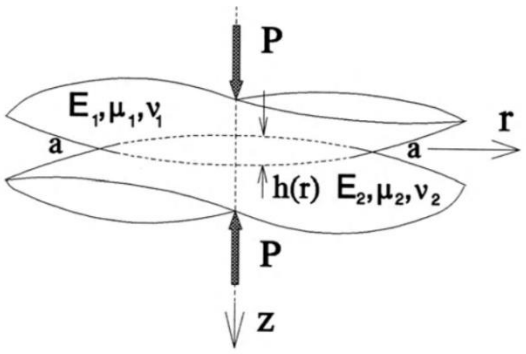

Figure 1 Contact of two spheres. (Hills, Nowell and Sackfield, 1993)**.**

In his theory, Hertz presents the relationship between the load applied to the indenter and other parameters that will describe the specimen response to an indentation within the elastic domain. There are four main considerations assumed in the elastic contact theory derived by Hertz: first, it must be assured that the contact area is sufficiently small when compared to the characteristic dimensions of the bodies in contact, i.e., $a \ll R$, where a is the contact radius and R_{eq} is the equivalent radius of curvature. This condition requires continuous and non-conforming surfaces. Second, the deformation applied to

the elastic bodies must guarantee a stress state ruled by Hooke's elastic law. Third, the solids can be considered as an elastic half-space. It means that the resultant contact area must be smaller than the radii and the significant dimensions, both laterally and in depth, of each body in contact. Last, the Hertz theory admits only normal pressure transmitted between the surfaces in contact. Therefore, there is no tangential resistance which leads to a frictionless contact (Hertz, 1881; Johnson, 1985).

To understand the basics of the Hertz's contact theory, consider surface forces acting upon an elastic half-space, deforming it. According to Hertz's theory, the displacement (h_r) experienced by the surface is given by Equation 1.

$$h_r = \frac{1}{E_{eq}} \frac{3}{2} p_0 \frac{\pi}{4a} (2a^2 - r^2), \qquad r \leq a \ , \tag{1}$$

which is led by the resultant pressure distribution (p) caused by the surface forces, as given by Equation 2.

$$p = p_0 \left\{ 1 - \left(\frac{r}{a} \right)^2 \right\}^{\frac{1}{2}}, \tag{2}$$

where a is the contact radius, r is a radial coordinate. The term p_0 is the peak contact pressure, expressed in Equation 3:

$$p_0 = \frac{3P}{2\pi a^2}. \tag{3}$$

and E_{eq} is the equivalent Young's modulus defined in terms of the Young's modulus and the Poisson's ratio of each body ($E_1, E_2, \upsilon_1, \upsilon_2$), expressed in Equation 4:

$$E_{eq} = \left(\frac{1 - \upsilon_1^2}{E_1} + \frac{1 - \upsilon_2^2}{E_2} \right)^{-1}, \tag{4}$$

Still, from Equation 1, the contact radius (a) is given by Equation 5:

$$a = \left(\frac{3PR_{eq}}{4E_{eq}} \right)^{1/3}, \tag{5}$$

where R_{eq} is the equivalent radius defined in terms of the radius of each body (Equation 6):

$$R_{eq} = \left(\frac{1}{R_1} + \frac{1}{R_2} \right)^{-1}. \tag{6}$$

The total force exerted on the contacting surface is obtained by integrating the pressure (p) over the contact area, as given by Equation 7:

$$P = \int_0^a p(r) 2\pi r dr = \frac{2}{3} p_0 \pi a^2 \tag{7}$$

The third restriction stated by Hertz (1881) (i.e. the contacting bodies touch each other over a small portion of their surface area, when compared to their dimensions) makes possible to describe the physical surface profile as a rotated parabola (Equation 8):

$$h_r = d - \frac{r^2}{2R_{eq}}, \tag{8}$$

where d is the approach of two remote points. By substituting Equation 1 into 8, it is possible to describe the total force (Equation 7) in terms of the rigid body approach d, as seen in Equation 9:

$$P = \frac{4}{3} E_{eq} R_{eq}^{\frac{1}{2}} d^{\frac{3}{2}} \tag{9}$$

So far, the contact pressure has been addressed and the answer has been provided regarding the shape of the contact and how it grows. Now the attention is turned to the development of the stress fields across the interface and inside the material for a purely normal indentation.

Huber (1904) detailed the stress field for the normal contact of two spheres in an axis-symmetric configuration where no shear tractions arise. The stress field is ($\sigma_{xx}, \sigma_{yy}, \sigma_{zz}, \tau_{yz}, \tau_{zx}, \tau_{xy}$) described from Equations 10 to 14

$$\frac{\sigma_{xx}}{-p_0} = \frac{1-2v}{3}\left(\frac{a^2}{r^2}\right)\left[1 - \left(\frac{z}{u}\right)^3\right] + \frac{z}{u}\left[2v + \left(\frac{(1-v)u^2}{a^2+u^2}\right)\right] - (1+v)\left(\frac{u}{a}\right) atan\left(\frac{a}{u}\right) \tag{10}$$

$$\frac{\sigma_{yy}}{p_0} = \frac{1-2v}{3}\left(\frac{a^2}{r^2}\right)\left[1 - \left(\frac{z}{u}\right)^3\right] + \left(\frac{z}{u}\right)^3 \frac{a^2 u}{u^4 + a^2 z^2} + \frac{z}{u}\left[\left(\frac{(1-v)u^2}{a^2+u^2}\right) + (1+v)\frac{u}{a} atan\left(\frac{a}{u}\right) - 2\right] \tag{11}$$

$$\frac{\sigma_{zz}}{-p_0} = \left(\frac{z}{u}\right)^3 \frac{a^2 u^2}{u^4 + a^2 z^2} \tag{12}$$

$$\frac{\tau_{yz}}{-p_0} = \frac{rz^2}{u^4 + a^2 z^2} \frac{a^2 u}{a^2 + u^2} \tag{13}$$

$$\tau_{zx} = \tau_{xy} = 0 \tag{14}$$

where u^2 is

$$u^2 = \frac{1}{2}\left(r^2 + z^2 - a^2 + \sqrt{(r^2 + z^2 - a^2)^2 + 4a^2z^2}\right) \qquad (15)$$

Having defined the stresses at a general point (r, z) , where $r = x^2 + z^2$, (Equations 10 to 14), contours for the von Mises equivalent stress (Equation 16) are represented in Figure 2 for v = 0.30.

$$\sigma_{eq} = \frac{1}{\sqrt{2}}\left[\left(\sigma_{xx} - \sigma_{yy}\right)^2 + (\sigma_{xx} - \sigma_{zz})^2 + \left(\sigma_{zz} - \sigma_{yy}\right)^2 + 6(\tau_{xy}^2 + \tau_{xz}^2 + \tau_{yz}^2)\right]^{1/2} \qquad (16)$$

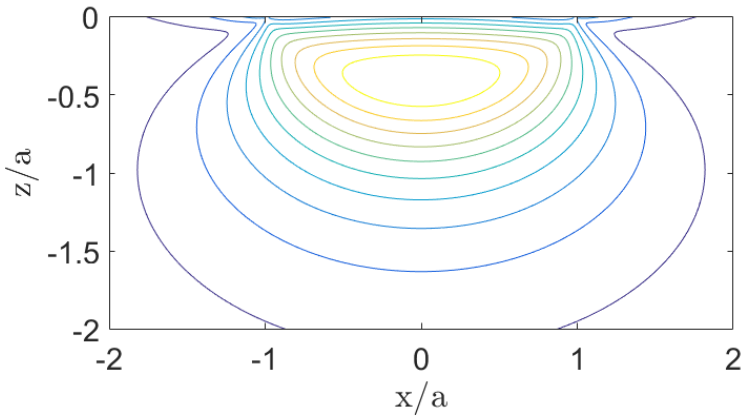

Figure 2. Contours of the von Mises equivalent stress for the spherical Hertzian contact.

Figure 2 shows that the critical stress state lies on the axis of symmetry. Therefore, by looking at Figure 3, which shows the internal stresses distribution for r = 0, the maximum shear stress and the equivalent von Mises stress have their critical value at a depth of 0.481a.

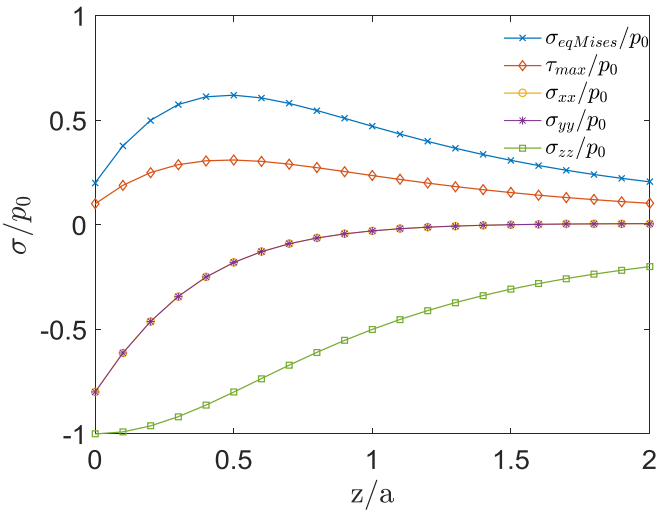

Figure 3. Internal stresses along the axis of symmetry (r = 0) for the Hertzian pressure distribution.

2.2 Post-yielding contact in metals

The severest stress state point of an indentation is distinguished out as the location where plastic yield begins. Therefore, there is a specific load associated with the transition from a totally elastic state to a regime that admits yielding. To find out the applied load (P) that leads to yielding, the maximum equivalent von Mises stress is considered as the yield criterion. For the Hertzian contact, the maximum equivalent von Mises stress is $0.62p_0$ and takes place at a depth of $0.481a$ on the axis of symmetry (r = 0) (Figure 3). Therefore, yield occurs when the peak contact pressure reaches $p_{0_Y} = 1.613\sigma_Y$, where σ_Y is the material yield strength. To relate the applied load P with the yield strength, Equation 5 first is substituted into Equation 3 to produce a relationship that links the applied load with the peak contact pressure, as shown in Equation 17 :

$$p_0 = \left(\frac{6PE_{eq}^2}{\pi^3 R_{eq}^2}\right)^{1/3}. \tag{17}$$

From Equation 17, the load associated with initial yielding is then given:

$$P_Y = \frac{\pi^3 R_{eq}^2}{6E_{eq}^2}\left(p_{0_Y}\right)^3. \tag{18}$$

At this stage, the elastic zone is still predominant as it surrounds the plastic zone. However, as the load increases, the plastic zone expands until breaking out to the free surface. Consequently, there is a redistribution of the surface contact pressure to the point of reaching the state of full plasticity, which is characterized by the dominant plastic material under the indenter (Hills, 1983; Johnson, 1985). At the state of full plasticity, the yield pressure is independent of the load and of the size of indentation (for fully work-hardened materials), which makes the contact pressure become uniform and provides appropriate means of measuring hardness (Tabor, 1951).

The evolution of the plastic zone in the indented material happens in three stages (Figure 4). The first is purely elastic (Figure 4a), where no plastic deformation is present. The second starts when the peak contact pressure assumes the critical value of $p_{0_Y} = 1.613\sigma_Y$, which is equivalent to the mean contact pressure of $P_m \approx 1.075\sigma_Y$. At this state, plasticity initiates, but is kept contained by the elastic material (Figure 4b), therefore it is a regime of transition from the elastic to the fully-plastic. Once the plastic flow becomes uncontained (Figure 4c), the third indentation stage takes place. Experimental analysis carried out by Tabor (1951) on several work-hardened metals led him to conclude that the fully-plastic stage initiates when $P_m \approx 3\sigma_Y$.

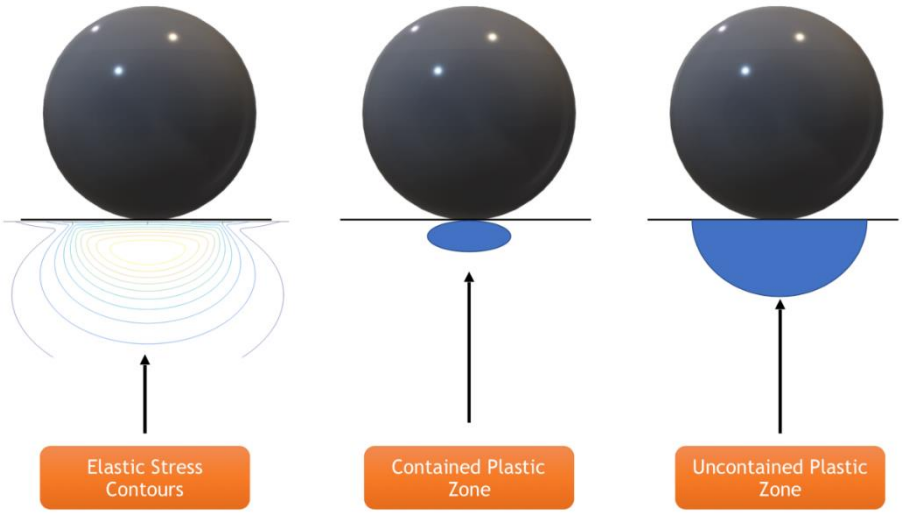

Figure 4. Evolution of plastic zone for ball indentation in three regimes: (a) elastic, (b) elastic-plastic, and (c) fully plastic. Adapted from Ahn and Kwon (2001).

Johnson (1970, 1985) then proposes a parameter Γ to govern the indentation pressure, whereby the plastic zone develops. He first considers that the indentation is idealized as an expanding cavity where its volumetric expansion is equivalent to the volume displaced by the indenter. This assumption leads him to admit that the amount of strain experienced by the solid is proportional to the contact angle β between the indenter and the specimen (β kept small), as shown in Figure 5.

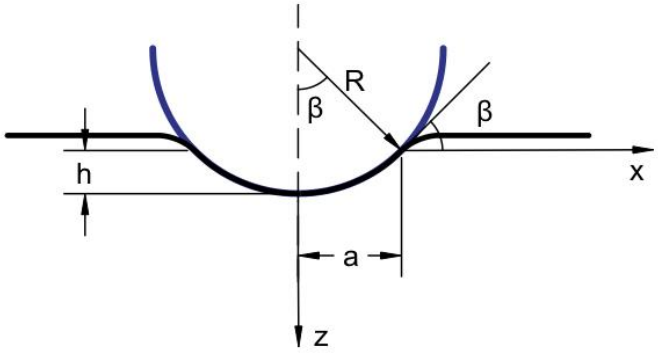

Figure 5. Ball indentation of a surface and influence of the angle β.

The parameter (Γ) proposed by Johnson (1970, 1985) is defined in terms of the contact angle β and the yield strain of the material σ_Y/E. It then provides the ratio

$$\Gamma = \frac{\tan(\beta)}{\frac{\sigma_Y}{E}}, \tag{19}$$

which informs the amount of strain experienced by the indented material to its elastic strain capacity. With this consideration, he correlates the ratio of the mean contact pressure to yield stress (P_m/σ_Y) with the proposed parameter Γ, in order to level the indentation in the elastic, elastic-plastic or fully-plastic regimes. According to Johnson (1970, 1985), the indentation behavior is elastic if $\Gamma < 3$, elastic-plastic if $3 \leq \Gamma < 40$ and fully-plastic for $\Gamma \geq 40$. This correlation is shown in Figure 6.

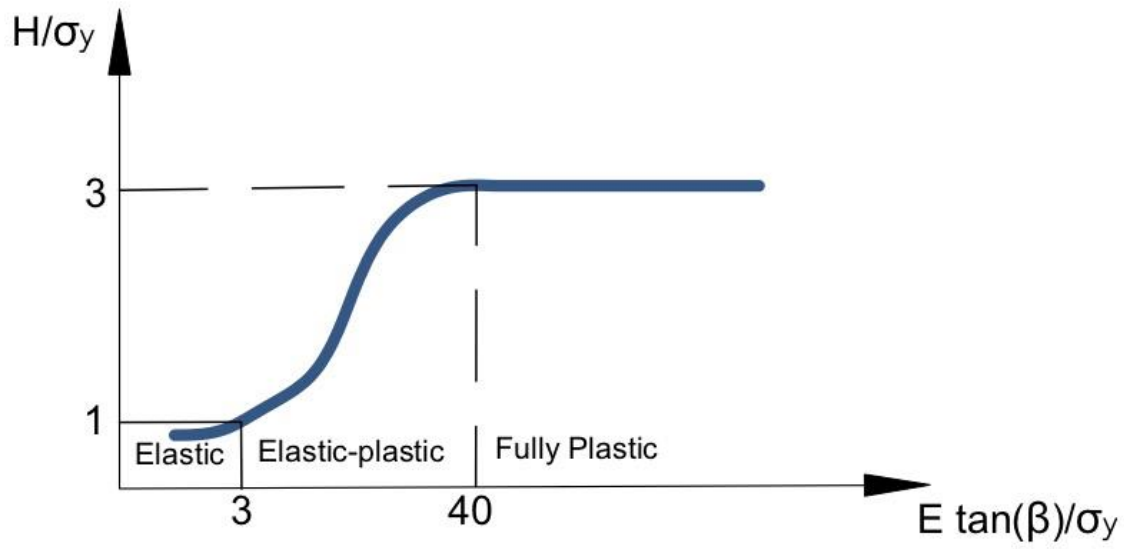

Figure 6. Schematic correlation of spherical indentation testing of elastic-plastic materials proposed by Johnson (1970, 1985). Adapted from Olsson and Larsson (2013)

2.3 Representative stress

Equation 19 does not consider materials capable of work-hardening, i.e. materials whose yield stress evolves under plastic deformation. To overcome this limitation Tabor (1951) suggests a representative stress σ_{rep} related to the elastic limit measured at a representative strain ε_{rep}, given as

$$\varepsilon_{rep}(x/a, y/a) = 0.2\tan(\beta). \tag{20}$$

In the full plasticity state, the mean contact pressure P_m is now related to the representative stress σ_{rep} according to Equation 21 (Tabor, 1951):

$$P_m = \Psi\, \sigma_{\mathrm{rep}}, \tag{21}$$

where Ψ is a plastic constraint factor expected to be related with the plastic zone expansion (Ahn and Kwon, 2001). This parameter assumes a constant value of 1.11 in the elastic regime, a linear function of ln(Γ) during the elastic-plastic transition, and a constant value ranging from 2.8 to 3.0 in the fully-plastic regime (Johnson, 1970; Li *et al.*, 2016).

Thus, the representative stress expression assumes the form shown in Equation 22:

$$\sigma_{rep} = \frac{1}{\Psi}\frac{P}{\pi a^2}, \tag{22}$$

From the definitions in Equations 20 and 21, the Johnson parameter (Γ) assumes the form expressed in Equation 23. The Johnson parameter considers materials able of work-hardening through the representative stress.

$$\Gamma = \frac{E}{\sigma_{rep}}\tan(\beta). \tag{23}$$

For work-hardening materials, the increasing indentation load will cause yield stress and plastic strain evolution. Unlike wedge, cone, and pyramid shaped indenters, spherical indenters are not geometrically similar. It means that $\tan(\beta)$ is not constant and thus change as a function of the indentation depth. Because the shape of the indentation changes as an increasing load is applied, it is possible to determine how the yield stress evolves with the amount of deformation. This excludes the use of different indenters' size to obtain distinct strain levels.

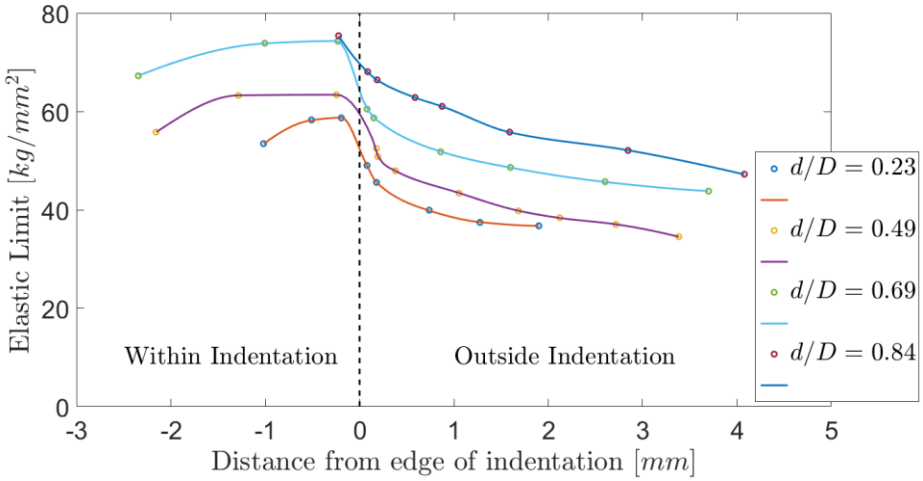

Figure 7. Variation of the yield stress along the indentation area

As Figure 7 illustrates, the plastic deformation is not uniform in the free surface inside and around the indentation. As a result of that, the material is hardened at different levels in the surrounding area of the indentation. Indeed, Tabor (1951) showed through several measurements on mild steel that the yield stress gradually rises as the edge of the indentation is approached (Figure 7). Even though the yield stress varies around the indentation, Equations 20 and 21 were empirically devised after concluding that the yield stress at the edge of the indentation stands as a representative quantity for the entire indentation area. It allows a direct correlation between hardness and true stress-strain curves, as shown in Figure 8.

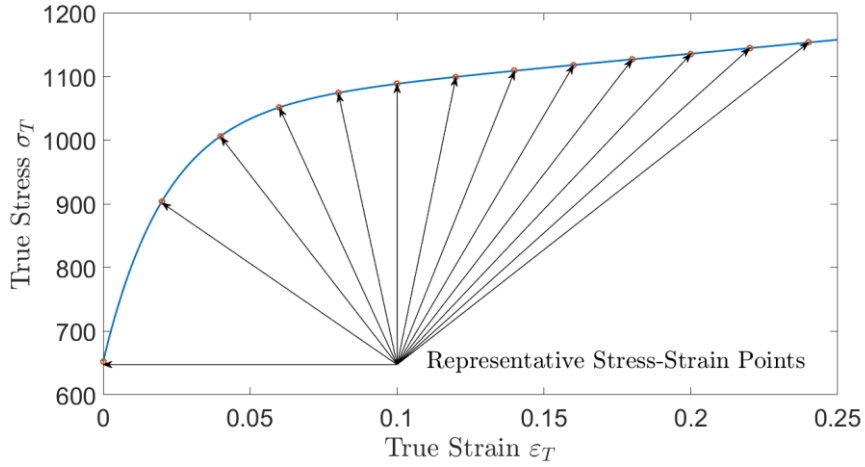

Figure 8. Hardening curve obtained from hardness measurements. Adapted from Li et al (2016)

The increasing yield pressure accompanying the size of indentation is a useful feature of spherical indentations. Not only the yield stress growth can be deduced from it but the amount of work-hardening as well. Therefore, each indentation depth will lead to a stress-strain point of the hardening curve of the material. This provides a suitable means to estimate the stress-strain characteristics of the indented material.

However, the analysis of post-yield indentation is not an easy task due to the complexity of the stress and strain fields beneath the indenter. For this reason, a theoretical treatment of this problem has not yet been achieved successfully, although many analyses have been performed through FEM and yielded more accurate results (Mesarovic and Fleck, 1999; Olsson and Larsson, 2013; Li *et al.*, 2016). Thus, equations 19 to 23 present analytical relationships devised empirically for the post-yield contact. Consequently, they are limited and only represent a correlation of indentation experiments.

2.4 Indentation Response

The impressed profile from spherical indentation does not solely depend on the material's hardness but is also strongly influenced by its strain-hardening behavior, indentation depth, and contact friction (Oliver and Pharr, 2004; Taljat and Pharr, 2004; Karthik *et al.*, 2012). Three main effects that accompany the indentation are shallowing, piling-up and sinking-in. Indentation shallowing happens as a result of the elastic recovery after the material is unloaded. Pile-up and sink-in happen around the edge of the indentation due to material flow.

2.4.1 Shallowing effect

During indentation unloading, there is a release of the elastic stresses in the material around the indentation. As a result, the impression shallows and yields a permanent curvature radius greater than the radius of the indenter. Figure 9 shows this effect through an illustration of the unloading process. In

(a), the indenter is brought into contact with the specimen. In (b), the indenter is pressed against the specimen and an impression is formed. In (c), the indenter is removed yielding a spherically shaped indentation impression with a radius of curvature ρ greater than that of the indenter R.

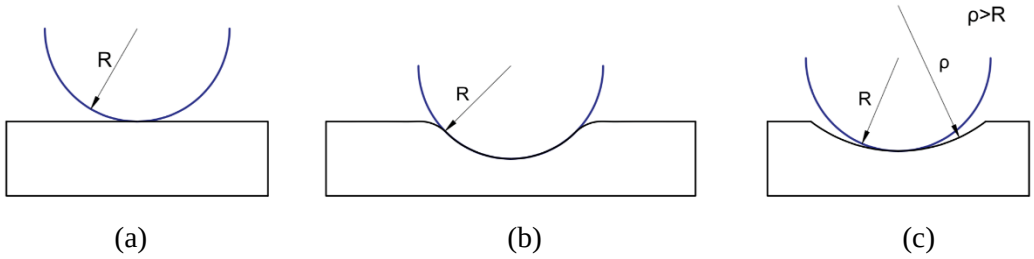

Figure 9. Unloading a spherical indenter. Adapted from Johnson (1985)

Figure 10 shows the shallowing effect from the perspective of the loading-unloading indentation curve. As it can be seen, the indenter displacement at peak load (h_{max}) considerably decreases when the load is fully withdrawn (h_f).

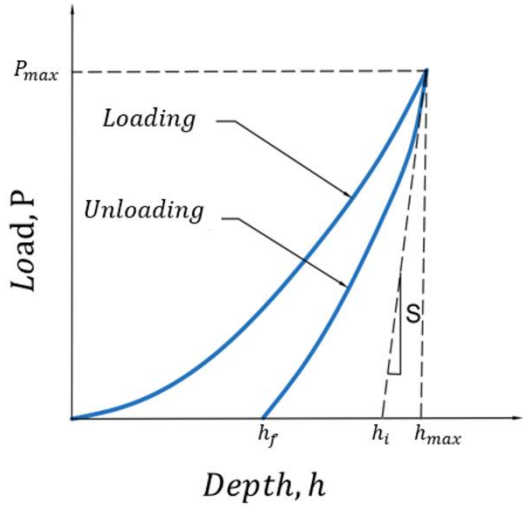

Figure 10. Indentation load-displacement data.

Since unloading is essentially elastic, Equation 9 can be modified to represent it. This is achieved by replacing the depth d that appears in this equation by $h - h_f$, as shown in Equation 24:

$$P = \frac{4}{3} E_{eq} R^{\frac{1}{2}} (h - h_f)^{\frac{3}{2}} \qquad (24)$$

From Figure 10, two important relationships can be derived. The first is the Kick's law expressed in Equation 25, which is used to describe the loading portion of the indentation reaction curve (Kang, 2013).

$$P = Ch^m, \tag{25}$$

where P is the applied load, h is the indentation depth and C and m are constants. Usual values for some common geometries are $m = 1$ for flat cylinders, $m = 2$ for cones, $m = 1.5$ for spheres considering small displacements and $m = 1.5$ for paraboloids of revolution (Oliver and Pharr, 1992).

The second important relationship derived from the indentation reaction curve is the initial unloading stiffness S. S is obtained by differentiating Equation 24 with respect to h, as expressed in Equation 26 (Oliver and Pharr, 2004).

$$S = \frac{\mathrm{dP}}{dh} = 2\sqrt{R}E_{eq}\left(h - h_f\right)^{\frac{1}{2}}, \tag{26}$$

where P is the load being continuously withdrawn.

2.4.2 Piling-up and sinking-in

When an indenter is pressed against a specimen with a load P, the plastic flow around the indenter may cause the surrounding material to pile-up or to sink-in. Pile-up happens when the plastic zone beneath the indenter and the surrounding elastic volume are not able to accommodate the volume change that occurs as the indenter penetrates the specimen (Karthik *et al.*, 2012). This reallocation due to volume change causes the material to pile-up at the contact edge. Sink-in is present in strongly hardening materials, indicating that this effect happens due to the constraint imposed by the surrounding material, making the plastic zone and the elastic volume to accommodate the volume change due to the indentation. Other factors, such as penetration depth, also influences the indentation contact area. These effects may be characterized by the parameter s, which is a height related to the undeformed surface. If $s > 0$, the material experiences piling-up; If $s < 0$, the material experiences sinking-in. These conditions are illustrated in Figure 11, where both pile-up (left-hand side) and sink-in (right-hand side) effects are shown.

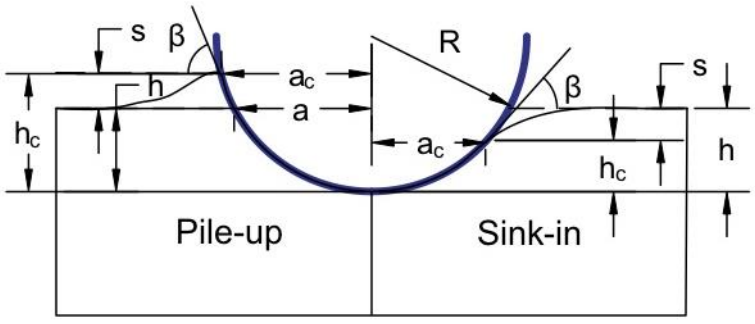

Figure 11. Spherical indentation contact geometry.Adapted from Taljat and Pharr (2004)

The determination of the contact area in indentation tests can be severely affected by the amount of pile-up/sink-in experienced by the material. Bolshakov and Pharr (1998) concluded that the true contact area can be underestimated by as much as 60% if pile-up is not taken into account. Figure 11 also shows the discrepancy in the measurement of the contact radius (a_c) and the contact height (h_c), which respectively varies from a and h depending on the amount of pile-up or sink-in.

2.4.3 Influence of the hardening exponent and friction on profile geometry and loading-unloading curve

According to Tabor (1951), pile-up and sink-in will be led by the work-hardening state of the material. Therefore, it is shown that the level of piling-up or sinking-in can be described by a numerical invariant $c^2 = a_c^2/(2Rh)$ dependent on the material hardening exponent n alone. Hill et all (1989) relates c^2 and n based on a power-law hardening of the form $\sigma = H\varepsilon^{p^n}$, where H is the hardening modulus. This relationship is then given according to Equation 27:

$$c^2 = \frac{5}{2}\left(\frac{2-n}{4+n}\right). \tag{27}$$

The parameter c^2 then represents the ratio of the contact depth to the total depth of penetration and is applicable for small penetration depths only. Thus, $c^2 > 1$ indicates that the material will pile-up while $c^2 < 1$ indicates that the material will sink-in. When $n \cong 0.28$, neither piling-up nor sinking-in will occur and $c^2 = 1$.

The contact friction is present in the interaction indenter-specimen due to their asperities. For the indentation contact configuration, the resistance to sliding is influenced by the material strain hardening, and the real contact area ratio (Leu, 2011). On the other hand, friction will influence the distribution of plastic strain beneath the indenter, the load-depth response, and the resultant profile (Mesarovic and Fleck, 1999; Karthik *et al.*, 2012).

According to Taljat and Pharr (2004), materials that strain harden are less sensitive to friction. This happens because, when indented, the surrounding material hardens (Figure 7). The evolution of the yield stress at the contact edge works as a barrier against plasticity at that region. Consequently, the plastic zone is driven deeper into the material instead of radially outward. A good way to visualize this effect is looking at the amount of pile-up of an indented material. Figure 12 shows how friction influences the resultant profile for a material with $E/\sigma_y = 200$ considering (a) an elastic perfectly plastic behavior and (b) an elastic strain-hardening-plastic material with $n = 0.5$ for six different friction coefficients: 0.0, 0.1, 0.2, 0.3, 0.5 and 1.0.

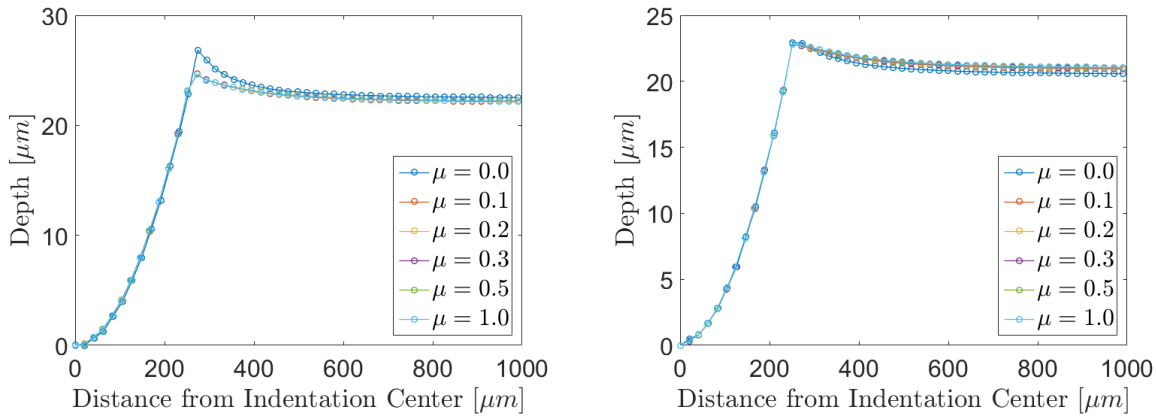

Figure 12. Influence of contact friction on unloaded indentation profile considering (a) an elastic perfectly plastic behavior and (b) an elastic strain-hardening-plastic material with $n = 0.5$ for six different friction coefficients: 0.0, 0.1, 0.2, 0.3, 0.5 and 1.0.

As concluded by Taljat et all and Karthik et all (2004; 2012), friction has a small effect on the indentation profile for strongly hardening materials. Furthermore, the profile is shown to be affected only for friction coefficients below 0.2. For those materials affected by friction, it acts toward diminishing pile-up and indentation depth.

Figure 13 shows the effect of friction on the loading-unloading indentation response. It is noted that the higher the load applied, the higher is the discrepancy caused by friction. As for the profile response, friction has no discernable effect for coefficients above 0.2.

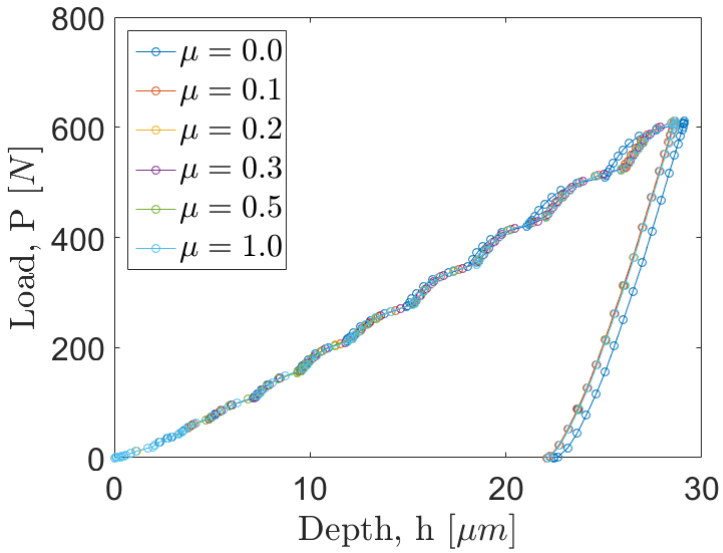

Figure 13. Effect of friction on the indentation loading-unloading curve.

The plastic strain distribution beneath the indenter is also affected by friction as shows in Figure 14. When considering a frictionless relationship between indenter and specimen, the specimen material is free to move relative to the indenter and the maximum effective plastic strain is nearer the surface. If friction is included, it acts as a radial constraint for the material relative motion near the contact site. Consequently, the strain distribution along the indentation axis of symmetry start at low values near the contact area and reaches its maximum values at a depth of $0.2a$. By comparing their results with Chaudhri's (1996), Mesarovic and Fleck (1999) concluded that this is a frictional effect.

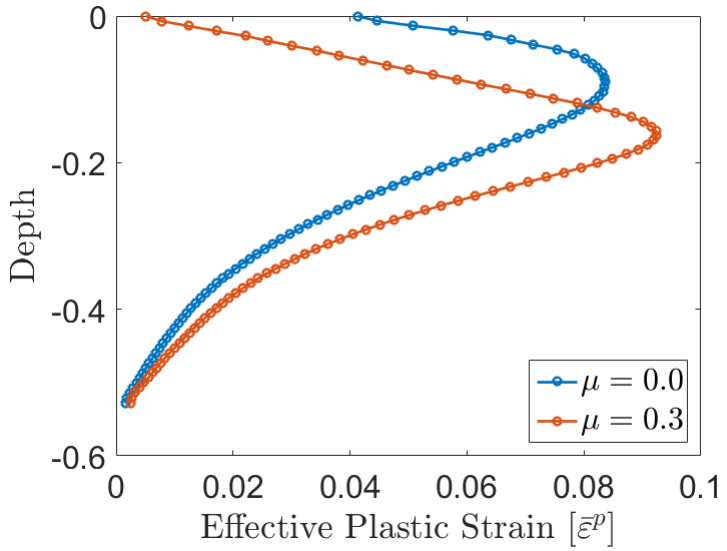

Figure 14. Distribution of effective plastic strain on the axis of symmetry beneath the indenter for an elastic-perfectly plastic material. with $E/\sigma_y = 200$.

Tabor (1951) states that experimental results reveal that surface roughness has little effect on the indentation profile geometry as long as the indentation is large enough when compared with the dimensions of the asperities. He concludes that there is no necessity to produce a high degree of surface finishing to obtain satisfactory hardness measurement on a metal sample.

2.4.4 Determination of the contact radius from indentation morphology

As mentioned above, the determination of the right contact radius is a difficulty task that arises when using the empirical relationships for the post-yield contact. This limitation is increased if the elastic deflection and pile-up/sink-in are included. One way to overcome it would be to optically measure the contact radius. However, a more convenient way is to obtain the contact radius from the indentation morphology.

If pile-up/sink-in are neglected, the contact depth h_c^* can be defined as:

$$h_c^* = h_{max} - h_d, \tag{28}$$

where h_{max} is the maximum indentation depth, and h_d is the elastic deflection depth at the contact perimeter. For a more realistic relationship, the pile-up/sink-in effect is included by a representation that changes the contact depth of the indentation. The contact depth h_c then can be calculated from Equation 29:

$$h_c = h_{max} + s, \tag{29}$$

where s is the displacement of the surface at the perimeter of the contact.

For the perfectly elastic response, there is no residual deformation after unloading. Therefore, h_c is equal to $^1/_2\, h_{max}$, as defined according to the Hertz equations for a rigid indenter. Consequently, h_d is also equal to $^1/_2\, h_{max}$ and there is no pile-up or sink-in. For the perfectly plastic case, there is no elastic recovery and $h_d = 0$. However, pile-up/sink-in effects have to be considered for a realistic analysis. (Ahn and Kwon, 2001). These conclusions show that both the elastic deflection and pile-up/sink-in phenomena must be included into the elastic-plastic indentation relationships. Thus, for the elastic-plastic indentation, the elastic deflection depth (h_d) is defined as:

$$h_d = \omega(h_{max} - h_i), \tag{30}$$

where h_i is the intercept depth obtained by extrapolating the tangent line of the indentation unloading curve. ω is a constant dependent of the shape of the indenter. For a paraboloid of revolution, ω is 0.75.

Since the parameter c^2 then represents the ratio of the contact depth to the total depth of penetration, it can be also defined in terms of the contact radius, where:

$$c^2 = \frac{a^2}{a^{*2}}, \tag{31}$$

where a^* is the contact radius neglecting pile-up/sink-in phenomena. Using the geometric relationship between contact depth and contact radius for spherical indentation: $a^* = 2Rh_c^* - {h_c^*}^2$, Equation 32 is derived and delivers the real contact radius with no need to use optical measurements. However, an instrumented indentation device must be available.

$$a^2 = \frac{5}{2}\frac{(2-n)}{4+n}(2Rh_c^* - {h_c^*}^2), \tag{32}$$

2.5 Non-linear mathematical models for material hardening

The behavior of materials in the plastic domain is very complex. Occasionally, it is necessary to idealize the plastic behavior of materials by means of simplifying the solution of a boundary condition problem. The suitability of a particular idealization depends on the real application (Khan, Akjtar S.;Huang, 1995). For this work, it is considered that the material's hardening process occurs in a non-linear manner, which is the case most observed in practice. Table 1 presents from Equations 33 to 40 some empirically obtained non-linear mathematical models for material hardening that are presented in the literature. Some of them are well known, such as the Kleinermann-Ponthot, which is used in this work.

Table 1: Empirically obtained non-linear mathematical models for material hardening.

Mathematical Model	Parameters	Reference	
$\sigma_y = \sigma_{y0} + H\bar{\varepsilon}_p^n$	$\sigma_{y0}, H, \bar{\varepsilon}_p^n$	Ludwick, 1909 (Khan, Akjtar S.;Huang, 1995)	(33)
$\sigma_y = \sigma_{y0}\, tanh(\frac{E}{\bar{\varepsilon}_p})$	$\sigma_{y0}, \bar{\varepsilon}_p$	Prager, 1938 (Khan, Akjtar S.;Huang, 1995)	(34)
$\bar{\varepsilon}_p = \frac{\sigma_y}{E} + H\left(\frac{\sigma_y}{E}\right)^n$	E, H, n	(Osgood and Ramberg, 1943)	(35)
$\sigma_y = H\bar{\varepsilon}_p^n$	H, n	(Hollomon, 1945)	(36)
$\sigma_y = H(\varepsilon_s + \bar{\varepsilon}_p)^n$	H, ε_s, n	(SWIFT, 1962)	(37)
$\sigma_y = \sigma_{y0} + (\sigma_s - \sigma_{y0})(1 - e^{-n\bar{\varepsilon}_p})$	σ_{y0}, σ_s, n	(Voce, 1948)	(38)
$\sigma_y = \sigma_{y0} + q_m(1 - e^{-b\bar{\varepsilon}_p}) + H\bar{\varepsilon}_p$	σ_{y0}, q_m, b, H	(Mahnken, 2002)	(39)
$\sigma_y = \sigma_{y0} + \xi\bar{\varepsilon}_p + (\sigma_\infty - \sigma_{y0})(1 - e^{-\delta\bar{\varepsilon}_p})$	$\sigma_{y0}, \xi, \sigma_\infty, \delta$	(J. P. Kleinermann and Ponthot, 2003)	(40)

2.6 Constitutive formulation

In this contribution, the hardening curve is approximated by an exponential function, according to Equation 40. This equation is chosen due to its capability to provide appropriate fitting to the hardening curves of the materials analyzed here. In fact, its design provides considerable control of the shape of the curve, which means flexibility to represent various hardening behaviors.

The accumulated plastic strain, $\bar{\varepsilon}^p$, is adopted as the internal variable associated with isotropic hardening, which is defined as:

$$\bar{\varepsilon}^p = \int_0^t \sqrt{\frac{2}{3}\dot{\boldsymbol{\varepsilon}}^{\boldsymbol{p}} : \dot{\boldsymbol{\varepsilon}}^{\boldsymbol{p}}}\ . \tag{41}$$

Thus, the accumulated plastic strain evolution rate is determined considering the work-hardening description, where plastic work can be mathematically defined as:

$$W^p = \int_0^t \boldsymbol{\sigma} : \dot{\boldsymbol{\varepsilon}}^{\boldsymbol{p}}\ , \tag{42}$$

and its evolution is given by:

$$\dot{W}^p = \boldsymbol{\sigma} : \dot{\boldsymbol{\varepsilon}}^{\boldsymbol{p}}, \tag{43}$$

In general, yield criteria are formulated in terms of an equivalent stress (σ_{eq}), which describes general multiaxial stress states by a scalar quantity. Considering Eq. (43) for plastic yielding, i.e. when the equivalent stress equals to the material's yield stress $\left(\sigma_{eq} = \sigma_y(\bar{\varepsilon}^p)\right)$, it can be rewritten as:

$$\dot{W}^p = \boldsymbol{\sigma} : \dot{\boldsymbol{\varepsilon}}^{\boldsymbol{p}} = \sigma_y(\bar{\varepsilon}^p)\dot{\bar{\varepsilon}}^p\ , \tag{44}$$

or rewritten in terms of equivalent stress:

$$\boldsymbol{\sigma} : \dot{\boldsymbol{\varepsilon}}^{\boldsymbol{p}} = \sigma_{eq}\dot{\bar{\varepsilon}}^p\ , \tag{45}$$

For associative plasticity, strain-hardening and work-hardening descriptions are equivalent (Souza Neto, Peric and Owen, 2008). For associative models, the so-called yield function is used as a flow potential or dissipation potential, i.e.:

$$\Lambda = \Phi, \tag{46}$$

where Λ represents the flow potential and Φ is the material yield function.

In this case, associative plasticity implies that the plastic strain rate is a tensor normal to the yield surface in the deviatoric plane. Thus, the evolution equation for the plastic strain, $\dot{\boldsymbol{\varepsilon}}^{\boldsymbol{p}}$, is obtained as follows:

$$\dot{\boldsymbol{\varepsilon}}^{\boldsymbol{p}} = \dot{\gamma}\ \boldsymbol{N}, \tag{47}$$

where $\dot{\gamma}$ represents the plastic multiplier and $\boldsymbol{N}$ is the plastic flow vector, given by:

$$N = \frac{\partial \Phi}{\partial \boldsymbol{\sigma}}. \tag{48}$$

Therefore, replacing the relation presented in Equation 47 in Equation 45 and after some mathematical manipulation, the accumulated plastic strain evolution rate expression is obtained:

$$\dot{\bar{\varepsilon}}^p = \frac{\boldsymbol{\sigma}:\dot{\boldsymbol{\varepsilon}}^{\boldsymbol{p}}}{\sigma_{eq}} = \dot{\gamma}\frac{\boldsymbol{\sigma}:\boldsymbol{N}}{\sigma_{eq}}, \tag{49}$$

Regarding the constitutive formulations for a description of the mechanical behavior of ductile materials, the von Mises approach with isotropic hardening is used. The formulation is resumed in Box 1.

Box 1: Mathematical Model for Hosford's (2013) and Gao et al.'s (2010) yield criteria.

Elastic-plastic split of the strain tensor

$$\boldsymbol{\varepsilon} = \boldsymbol{\varepsilon^e} + \boldsymbol{\varepsilon^p}, \tag{50}$$

Elastic law

$$\boldsymbol{\sigma} = \mathbb{D}^e : \boldsymbol{\varepsilon^e}, \tag{51}$$

Yield Function

$$\Phi = \sigma_{eq} - \sigma_y(\bar{\varepsilon}^p), \tag{52}$$

with: $\sigma_{eq} = \sqrt{3J_2}$

$\sigma_y(\bar{\varepsilon}^p)$ is the hardening rule of the material.

Plastic flow rule and evolution equation for $\dot{\bar{\varepsilon}}^p$

$$\dot{\boldsymbol{\varepsilon}}^p = \dot{\gamma}\boldsymbol{N} \tag{53}$$

$$\dot{\bar{\varepsilon}}^p = \frac{\boldsymbol{\sigma}:\dot{\boldsymbol{\varepsilon}}^{\boldsymbol{p}}}{\sigma_{eq}} = \dot{\gamma}\frac{\boldsymbol{\sigma}:\boldsymbol{N}}{\sigma_{eq}},$$

$$\text{with } \boldsymbol{N} = \sqrt{\frac{3}{2}}\frac{\boldsymbol{S}}{\|\boldsymbol{S}\|}.$$

Complementary conditions:

$$\dot{\gamma} \geq 0, \qquad \Phi \leq 0, \qquad \dot{\gamma}\Phi = 0 \tag{54}$$

2.7 Parameter Identification

The parameter identification is carried by an optimization algorithm that minimizes the discrepancy between numerical and experimental load versus displacement data. The Trust-Region-Reflective Least Square Algorithm is a solver method for optimization problems. For this case, it is used to determine the minimum of an objective function $f\ (\boldsymbol{p})$, where $\boldsymbol{p}$ represents the plasticity parameters. The objective function takes vector arguments, representing the responses whose discrepancy is to be minimized, and returns a scalar quantity representing the overall discrepancy. The closer this discrepancy gets to zero or to the established tolerance, the better the suggested parameter set is. Therefore, the goal is to find the solution for the problem stated at Equation 55:

$$\underset{\boldsymbol{p} \in \mathbb{R}^n}{minimize}\, f(\boldsymbol{p}), \tag{55}$$

It is considered an iterative technique producing a sequence of iterates $\{\boldsymbol{p}_k\}$ that will minimize the objective function. At each iteration $\boldsymbol{p}_k$, a model m_k is adopted to approximate the objective function within a proper neighborhood of $\boldsymbol{p}_k$, called trust-region. Usually, the model m_k is defined by the first two terms of the Taylor approximation to $f(\boldsymbol{p})$, as shown in Equation 56 (Conn, Andrew R.; Gould, Nicholas I. M.; Toint, 2000).

$$m_k(\boldsymbol{p}_k + \boldsymbol{s}) = m_k(\boldsymbol{p}_k) + \langle \boldsymbol{g}_k, \boldsymbol{s} \rangle + \frac{1}{2}\langle \boldsymbol{s}, \boldsymbol{H}_k \boldsymbol{s} \rangle, \tag{56}$$

where $\boldsymbol{s}$ is the trial step for the trial point $\boldsymbol{p}_{k+1} = \boldsymbol{p}_k + \boldsymbol{s}$, whose goal is to minimize m_k. We also have that $m_k(\boldsymbol{p}_k) = f(\boldsymbol{p}_k)$, $\boldsymbol{g}_k = \nabla_x f(\boldsymbol{p}_k)$ and that $\boldsymbol{H}_k = \nabla_{xx} f(\boldsymbol{p}_k)$ is the Hessian matrix.

The trust-region is then defined as shown in Equation 57:

$$\Omega_k = \{\boldsymbol{p} \in\ \mathbb{R}^n, |\ \|\boldsymbol{p} - \boldsymbol{p}_k\|_2 \leq \Delta_k\}, \tag{57}$$

where Δ_k is the trust region radius and $\|\cdot\|$ is the 2-norm.

A crucial procedure in the trust region implementation is the determination of the trial step $\boldsymbol{s}$, which seeks to reduce the model m_k in the trust-region. This procedure is equivalent to solve the trust-region subproblem, as stated in Equation 58 .

$$\begin{aligned} &minimize\ m_k(\boldsymbol{p}_k + \boldsymbol{s}) \\ &subject\ to\ \ \|\boldsymbol{s}\|_2 \leq \Delta_k \end{aligned} \tag{58}$$

MATLAB's optimization toolbox restricts the trust-region subproblem to the computation of a two-dimensional subspace $\boldsymbol{S}$, which is defined as the linear space spanned by the direction of the gradient g and an approximate Newton direction.

For the case adopted in this work, where f is treated with a nonlinear least-squares function, the problem to be solved instead is stated at Equation 59

$$\min_{\boldsymbol{p}} \sum_i f_i^2(\boldsymbol{p}) = \min_{\boldsymbol{p}} \ \|m(\boldsymbol{p})\|_2^2, \tag{59}$$

where $m(\boldsymbol{p})$ is a vector-valued function.

For the computation of the two-dimensional subspace $\boldsymbol{S}$, an approximation Gauss-Newton direction is used. It means to find the solution **s** for the Equation 60.

$$min \ \|J\boldsymbol{s} + m\|_2^2, \tag{60}$$

Therefore, the optimization procedure minimizes the function f ($\boldsymbol{p}$) which is the response of the discrepancy between FEM and experimental data, being based on the least-squares-root method, as it can be seen in the Equation 61 and Figure 15.

$$f(\boldsymbol{p}) = \sqrt{\frac{1}{n}\sum_{i=1}^{n}\left(\frac{\boldsymbol{R}_i^{FEM}(\boldsymbol{p}) - \boldsymbol{R}_i^{EXP}}{\boldsymbol{R}_i^{EXP}}\right)^2}, \tag{61}$$

where, $\boldsymbol{R}_i^{FEM}$ and $\boldsymbol{R}_i^{EXP}$ are, respectively, the numerical and the experimental responses.

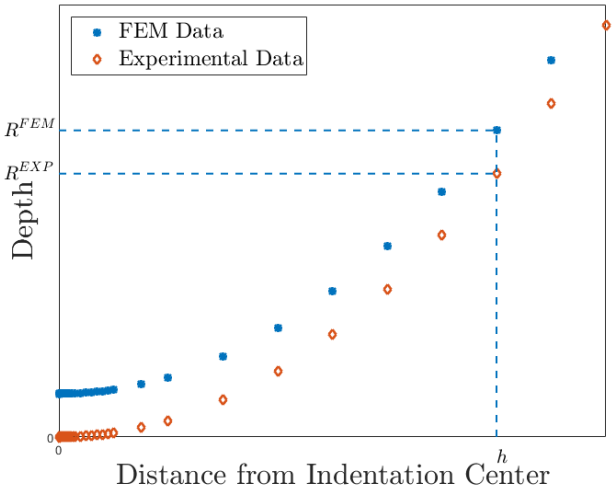

Figure 15. Optimization Approach.

CHAPTER 3. EXPERIMENTAL PROCEDURES

Both traditional tensile tests and indentation hardness tests are addressed in this chapter. The tensile test is the forward way to determine the hardening parameters of the material, while the indentation hardness test is part of an inverse method of parameter identification aided by numerical methods. Therefore, to have a way of comparison and to validate the indentation methodology, uniaxial tensile tests are also performed in parallel with the indentation hardness tests. In this contribution, the hardening curve is approximated by a function according to Kleinermann-Ponthot (2003), and represented as:

$$\sigma_y(\bar{\varepsilon}^p) = \sigma_{y0} + \xi\varepsilon_p + (\sigma_\infty - \sigma_{y0})(1 - e^{-\delta\bar{\varepsilon}_p}) \tag{62}$$

where σ_{y0} is the initial yield strength, and ξ, σ_∞, and δ are the hardening parameters of the model. This equation is chosen due to its flexibility in providing appropriate fitting to experimental data of various shapes.

The materials analyzed are the SAE 1524, SAE 4340 N (normalized), SAE 4340 A (annealed), and Aluminum 6101.

3.1 Uniaxial Tensile Test

Important parameters are extracted from the curve generated by the tension test, which can be later used to describe the material behavior through different hardening models (Equations 33 to 40). These results optimize the alloy development process and quality control, allowing comparisons between different materials. In the tension test, a specimen - manufactured according to the standard specifications addressed in the ASTM Int. E8/E8M (2009) - is submitted to uniaxial tensile stresses. A force versus strain data is produced, which will provide information about the material's mechanical behavior, such as its strength and ductility.

Here, the uniaxial test is performed to characterize the elastic-plastic behavior of the materials mentioned above. The experimental data provided will be used to determine a set of parameters that are part of Kleinermann-Ponthot's mathematical model that describes the material's stress-strain behavior. Thus, the uniaxial test yields the plasticity parameters values wherewith the IRC and IP approaches will be evaluated.

3.1.1 Specimen

It is desirable that the materials present certain characteristics, such as high strength and good ductility. To achieve such attributes, the SAE 1524 undergoes quenching and tempering heat treatments processes. Quenching is applied by heating the specimen for 90 min up to 890 ºC and keeping it in this

temperature for more 30 min until it is austenitized. The specimen is then cooled down to room temperature in water. Next, the specimen is tempered by being heated for 50 min until reaching 500 ºC and kept at this temperature for more 60 min. Next, the specimen is cooled down in water.

Two specimens of the SAE 4340 are manufactured and each one is submitted to a heat treatment distinct from the other: annealing and normalization. During annealing, the material is heated to 850 ºC and kept under that condition for one hour for every 25 mm of diameter bar. Next, the material is slowly cooled down inside the oven. Through this process the material has its ductility improved, so it becomes softer and acquires better machinability.

Normalizing is the process by which the material is heated above the upper critical temperature (860ºC – 900ºC) and kept under that condition for one hour for every 25 mm of diameter bar until the grains are totally converted into austenite. Next, the material is cooled down in open air. As a result, an alloy with refined grains is obtained. It produces a tougher material when compared to the annealed one, however, less ductile.

3.1.2 Data acquisition

The tensile tests were conducted in an MTS machine (Figure 16) with a 100 kN load capacity, where the specimen was elongated until it broke. The deformation was measured aided by a clip gauge of 25 mm of gauge length (5 mm in tension / −2.5 mm in compression).

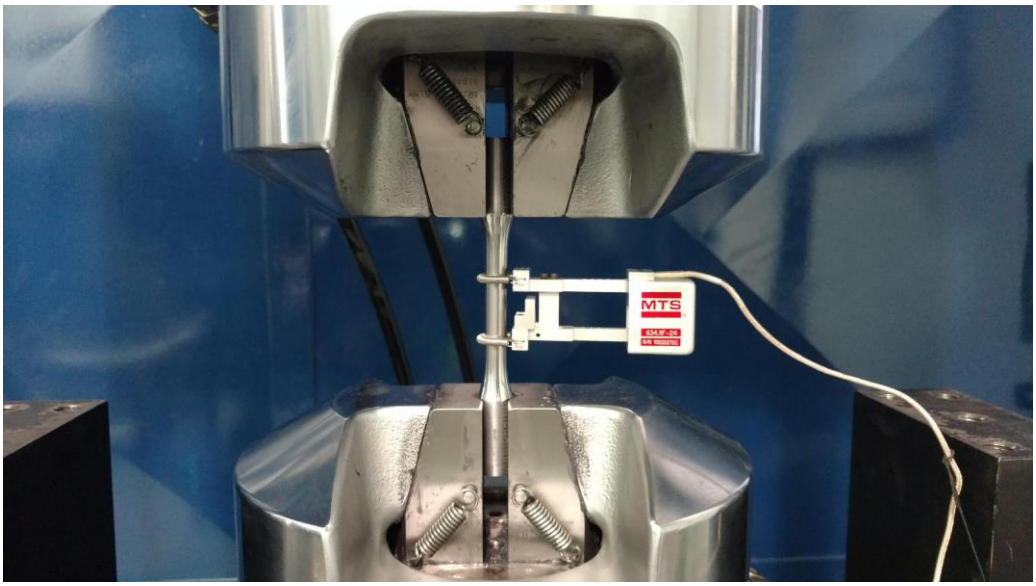

Figure 16: MTS with Clip Gauge Used for Tensile Test.

Figure 18 shows the reaction curves obtained from the uniaxial tensile for each material:

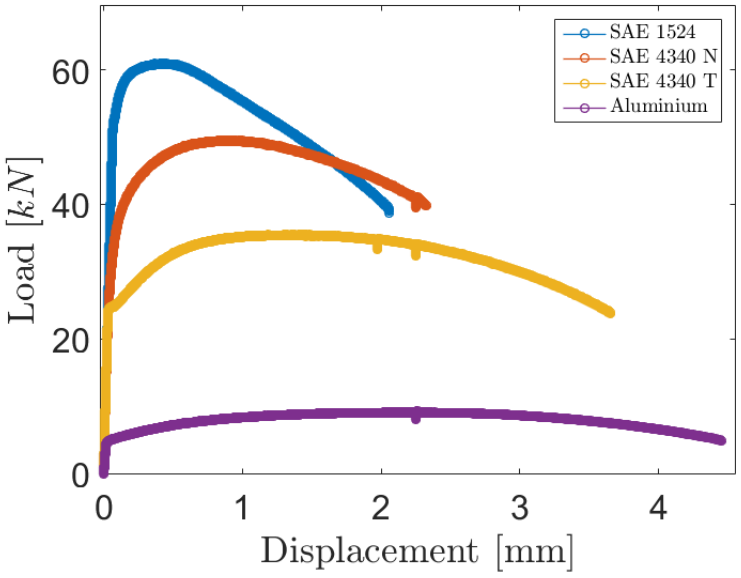

Figure 17. Reaction curves produced by uniaxial tension tests for the SAE 1524, SAE 4340 normalized and SAE 4340 annealed.

Taking the SAE 1524 as an example, the data assessment is shown in detailed for this specimen and then applied to the other materials. Figure 18 shows the data obtained by the measurement done by the clip gauge, which automatically converts the displacement of the specimen into strain.

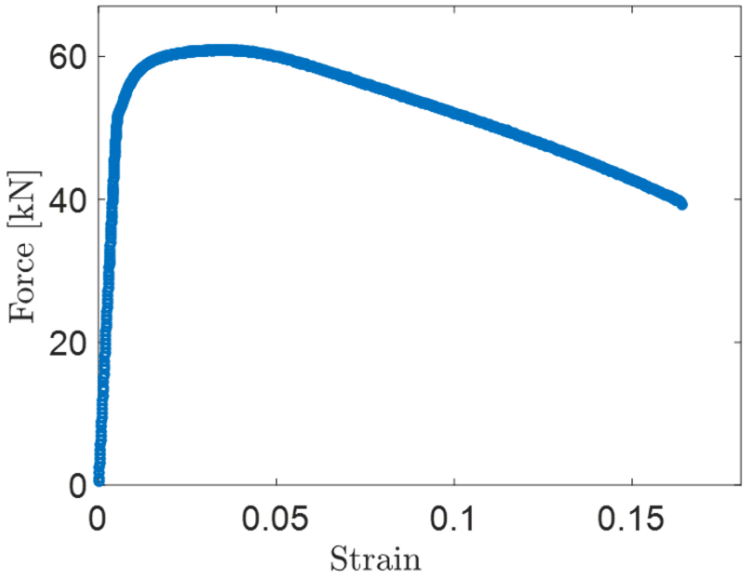

Figure 18. Reaction curve produced by uniaxial tension tests for the SAE 1524 in terms of the strain provided by the clip gauge.

From the tension test, important phenomenological aspects can be identified. Neto et al. (2008) point out three main aspects: the existence of an elastic domain, plastic flow, and hardening. Before we can address the main aspects of the tension test, let us define the curve shown in Figure 18 in terms of a stress-strain relationship ($\sigma - \varepsilon$). The so-called engineering stress is obtained by dividing the applied uniaxial Force (P) by the initial or the undeformed cross-sectional area (A_0) of the specimen (Equation 63).

$$\sigma = \frac{P}{A_0}, \tag{63}$$

Once Equation 63 is applied to the acquired data, the experiment then bears the engineering stress-strain curve shown in Figure 19:

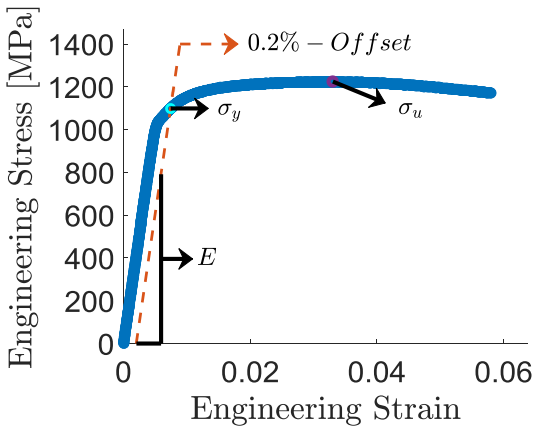

Figure 19. Engineering stress-strain relationship.

Now, we are able to assess some of the main aspects extracted from the tension test. First, we have the elastic domain, which is defined within the range where the material behaves linearly, which is, while the load applied is proportional to the deformation according to a constant E, known as Young's modulus (Figure 19). In this definition, every deformation suffered by the material is fully recovered after unloading and is governed by Hook's law. The Young's modulus and Poisson's ratio measured for the analyzed materials are shown in Table 2.

Table 2. Elastic Properties of the Specimens.

Materials	E $[GPa]$	ν
SAE 1524	200	0.3
SAE 4340 N	206	0.3
SAE 4340 A	200	0.3
Al 6101	66	0.3

When the proportionality between load and deformation is lost, yielding occurs and the material experiences plastic deformation, which is permanent. In this case, during unloading, the specimen will only partially recover its dimensions. The deformation extent recovered is the elastic component of the total deformation while the extent remaining is the plastic component. By convention, the transition from the elastic region to the elastoplastic regime is said to occur when plastic deformation averages 0.2 %. This is known as the offset method, which is applied to determine the yield strength (σ_y) - the engineering stress at which the elastoplastic regime takes place (ASTM Int., 2009) – as it can be seen in Figure 19.

As plastic flow occurs, the material undergoes hardening, which is characterized by the yield stress evolution. The analyzed specimens are made of materials with high ductility and, therefore, experience considerable changes in their dimensions as they are being deformed. For this reason, the stresses can no longer be determined assuming the initial cross-sectional area of the specimen. To overcome this limitation, we have the true stress-strain definition, which takes into consideration finite changes in area and length. With the assumption of deformation at constant volume, the true stress-strain curve can be determined from the engineering stresses and strains, as shown in Equations 64 and 65. However, Equations 64 and 65 are only valid up to the highest value of engineering stress, which is known as tensile strength or ultimate strength (σ_u) (ASM International, 2004), shown in Figure 19.

$$\bar{\sigma} = \sigma(1 + \varepsilon), \tag{64}$$

$$\bar{\varepsilon} = ln(1 + \varepsilon), \tag{65}$$

The engineering stresses and strains are only suitable for small deformations – Dowling (2013) suggests an arbitrary value of twice the strain related to the yield strength ($2\varepsilon_{y0}$). Figure 20 shows both engineering and true stress-strain curves where we can see that, for twice the strain related to the yield strength, engineering and true stress-strain curves present little discrepancy. As the curves move away from $2\varepsilon_{y0}$, the difference between them increases.

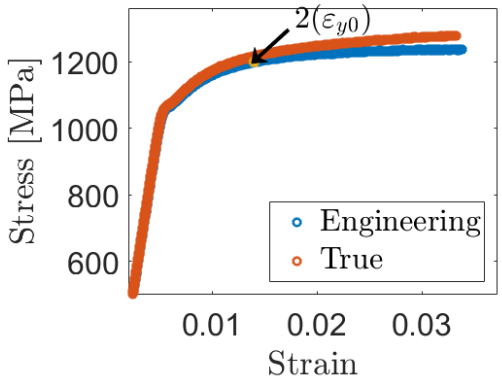

Figure 20. Engineering and true stress-strain relationships.

Beyond the tensile strength, changes in area and length must be considered to determine the true stress-strain relationship ($\bar{\sigma} - \bar{\varepsilon}$). From this point on, the specimen starts to experience necking as a result of the reduction of its cross-sectional area. Also, the assumption of deformation at constant volume is no longer valid (Dowling, 2013). Therefore, to obtain the true stress-strain relationship ($\bar{\sigma} - \bar{\varepsilon}$) the current cross-sectional area (A_i) in the necked region must be directly measured so that the stresses and the strains are evaluated at each increment according to Equations 66 and 67.

$$\sigma = \frac{P}{A_i}, \tag{66}$$

$$\varepsilon = \frac{A_0}{A_i}, \tag{67}$$

For large strains, however, the uniaxial tensile test does not represent the intrinsic tensile behavior of the specimen. This leads us to call on numerical approaches to determine the full true stress-strain relationship of the material under analysis.

3.1.3 Parameter identification

The parameters that describe the hardening curve of each material analyzed is are determined by an inverse optimization approach aided by FEM analysis. The uniaxial tensile test is numerically modeled and the reaction curves from Figure 17 are taken as the target curves in the process.

The reaction curve fitting shown in Figure 21 was generated by the optimum parameters listed in Table 3 for each material assessed.

Table 3. Material parameters obtained from the numerical inverse optimization process for Kleinermann-Ponthot's model.

$Model$	$\sigma_y(\bar{\varepsilon}^{\mathrm{p}}) = \sigma_{y0} + \xi\varepsilon_p + (\sigma_\infty - \sigma_{y0})(1 - e^{-\delta\varepsilon_p})$				
Materials	σ_{y0} $[MPa]$	ξ [MPa]	σ_∞[MPa]	δ	$\bar{\varepsilon}^p_{max}$
SAE 1524	1046.56	100.53	1297.47	77.17	0.46
SAE 4340 N	652.2	439.4	1048.0	47.569	0.66
SAE 4340 A	463.7	401.3	774.8	23.847	1.20
Al 6101	96.13	63.2	220.87	12.147	1.51

Repeated FEM modeling is performed until the suggested parameters produce a numerical reaction curve that fits the experimental one. The best fit provided for each material is shown in Figure 21.

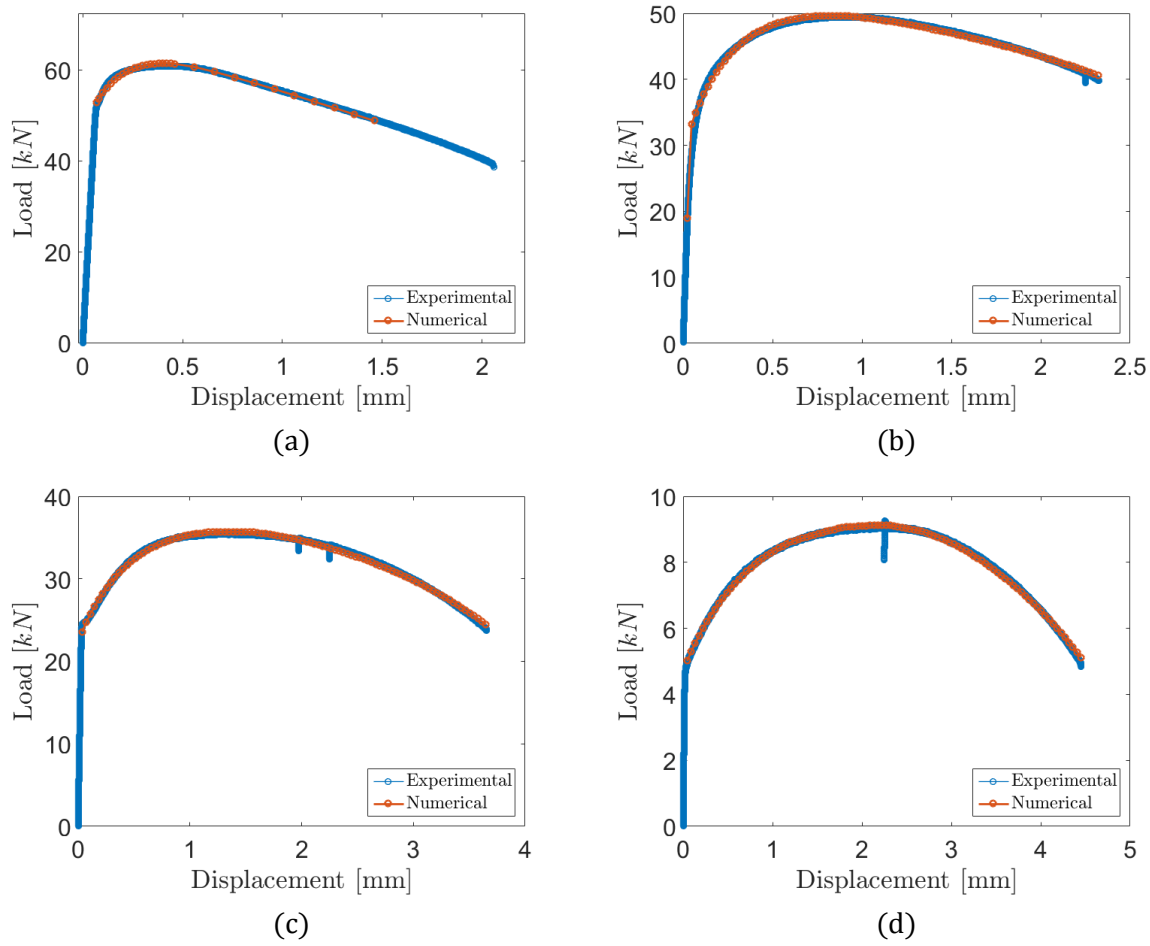

Figure 21. Reaction curve fitting provided by the optimization procedure to determine the optimum plasticity parameters for the (a) SAE 1524, (b) SAE 4340 N, (c) SAE 4340 A, and (d) Aluminium 6101.

The hardening curves in Figure 22 are generated with the parameters listed in Table 3 inserted in the Kleinermann-Ponthot's constitutive model. For each stress-strain curve, it is considered the maximum effective plastic strain reached during simulation. It provides a full representation of the strain field inside the material and not only its average response as obtained experimentally. Consequently, it is reasonable to consider these numerical values as the maximum strain reached within the material before collapsing.

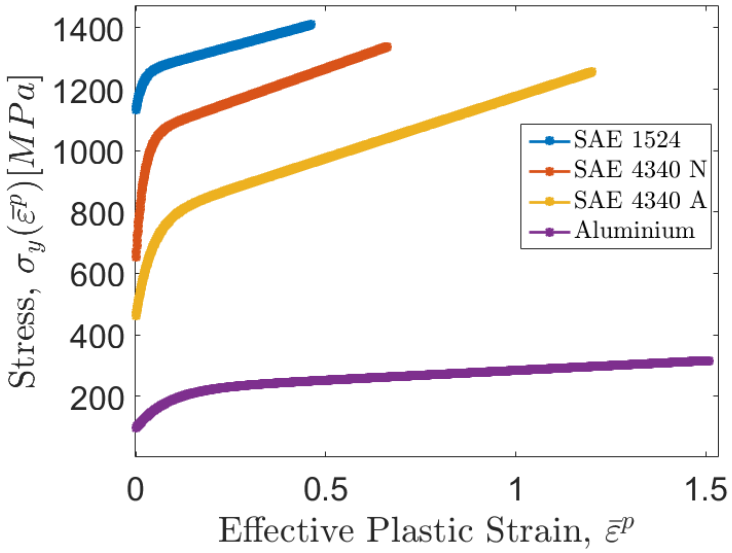

Figure 22. Hardening curves determined from the uniaxial tensile test

3.2 Brinell Indentation Hardness Test

The hardness test is essentially a way to assess the plastic properties of ductile materials, providing information about their capacity to resist a local deformation (Tabor, 1970). The test is carried out by pressing a hard indenter against the surface of the material and measuring the dimensions of the permanent impression formed. The Brinell hardness test was the first of many other modern techniques for measuring the hardness of metals and will be considered in this application due to its versatility and convenience.

The Brinell hardness test may be performed in several configurations covering a wide range of materials, from very soft to very hard. It provides useful information that can be correlated to other physical characteristics besides its hardness, e.g., tensile strength, wear resistance and ductility (ASTM Int., 2012). In this test, a hard tungsten carbide ball, with $E = 645\ GPa$, is pressed into a flat surface generating an impression whose profile is a segment of a sphere.

The Brinell test consists of two major steps: first, the indenter is brought into contact with the specimen and the load is applied. Second, the diameter of the impression (d_i) is measured twice at right angles. These indentation diameters are used to determine the Brinell hardness number by dividing the applied load (P) by the curved surface area of the indentation, according to Equation 68.

$$HBW = \frac{P}{\pi D h} = \frac{2P}{\pi D\left(D - \sqrt{D^2 - d_i^2}\right)}, \tag{68}$$

where D is the indenter diameter and h is the penetration depth of the indentation.

3.2.1 Specimen

Regarding the dimensions of the specimen, there is not a standard size or shape for the Brinell hardness test. There are, however, recommendations and limitations that establish some characteristics that the specimen must have to produce accurate results. The basic characteristics are related to thickness and width. The thickness of the material should be at least ten times the depth of the indentation h. The minimum width must attend the requirements of indentation spacing, that establish a minimum distance of three times the impression diameter between the center of two adjacent impressions. That works to minimize any alteration of the surface hardness for adjacent indentations (ASTM Int., 2012). The specimens under analysis are shown in Figure 23

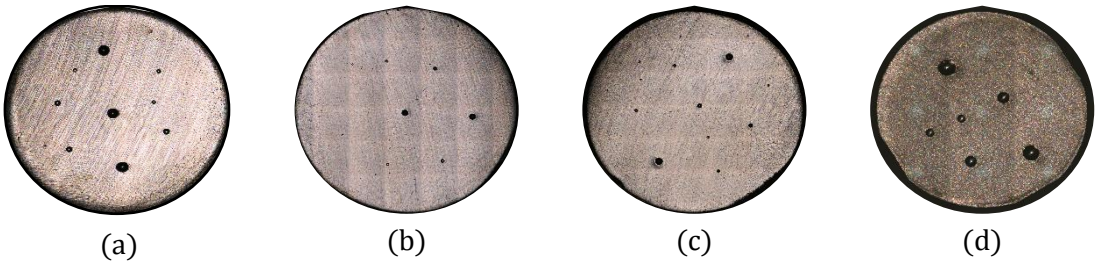

Figure 23. Specimens: (a) SAE 1524, (b) 4340 N, (c) 4340 A, and (d) Aluminum 6101.

3.2.2 Data acquisition

The Brinell indentation method is used as a way to correlate an applied load to the resultant geometry impressed in the specimen. Since the indentation mark is a result of plastic flow (Tabor, 1948), the material behavior may be described by a plasticity model. The characterization of any plasticity model encompasses the definition of a plasticity law for the internal variables associated with hardening. In this manner, it is possible to define material parameters to represent the dependence of the yield stress level upon the history of plastic straining experienced by the specimen under analysis.

The uniaxial tensile test can be directly related with all the essential concepts of the mathematical theory of plasticity (de Souza Neto, Peri and Owen, 2008), as shown in Section 3.1. To correlate the material plasticity parameters with a ball indentation test, two approaches are attempted. The first is based on empirical analytical relationships while the second is based on an inverse methodology aided by numerical methods, as will be presented in CHAPTER 5 and CHAPTER 6 respectively. Most approaches have been widely applied since the development of instrumented indentation devices which are able to continuously measure the indentation depth while an increasing load is being applied. Unfortunately, such device was not available for the analyses presented here. Instead, traditional hardness tests were conducted with the Zwick/Roell ZHU250 hardness machine shown in Figure 24.

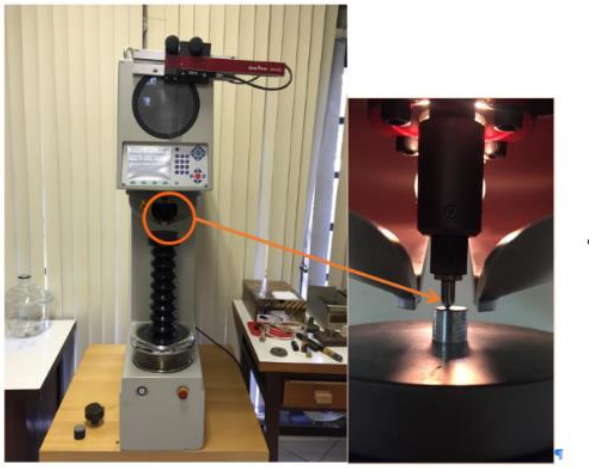

Figure 24. Zwick/Roell ZHU250 Universal Hardness Machine.

While the instrumented indentation devices provide a rich data set, each Brinell test procedure produces only one point which correlates the applied load to the resultant indentation profile. In order to produce more points, more indentation impressions must be produced from different configurations of the Brinell hardness test. Therefore, three configurations of the Brinell hardness test are applied using a tungsten carbide indenter of 2.5 mm diameter. The three loads applied are selected based on the considerations that it is high enough so that plasticity is predominant beneath the indentation but low enough to produce shallow indentations ($h_f \leq 0.06D$). They are the HBW 187.5/2.5, HBW 62.5/2.5, and HBW 31.25/2.5 for the steel samples. For the aluminum sample, they are the HBW 62.5/2.5, HBW 31.25/2.5, and HBW 15.625/2.5. Figure 25 to Figure 27 show the results for the materials under analysis.

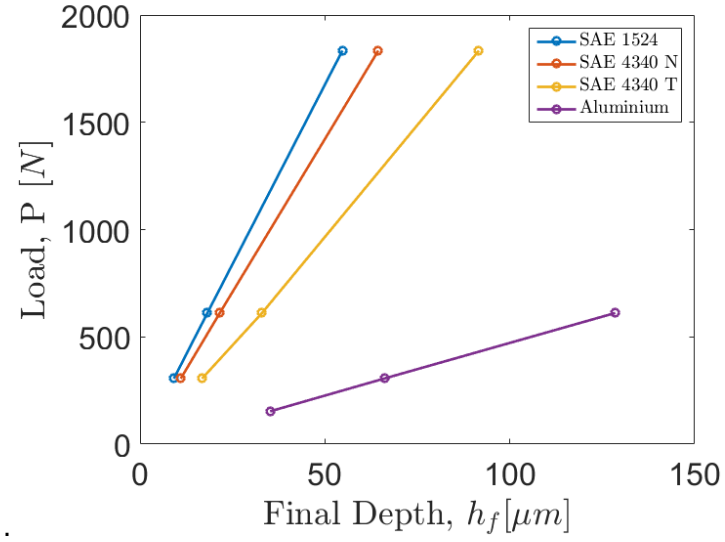

Figure 25. Experimental Indentation reaction data from Brinell Hardness tests for three different loads applied to the materials under analysis.

Each of these configurations will form distinct profiles with different levels of strain hardening. To extract the resultant indentation profile, a dimensional verification is also conducted using the *LEXT OLS4100* laser confocal microscope. From the *LEXT OLS4100* laser confocal microscope, Figure 26 is generated. It shows an example of a top and 3D indentation impression.

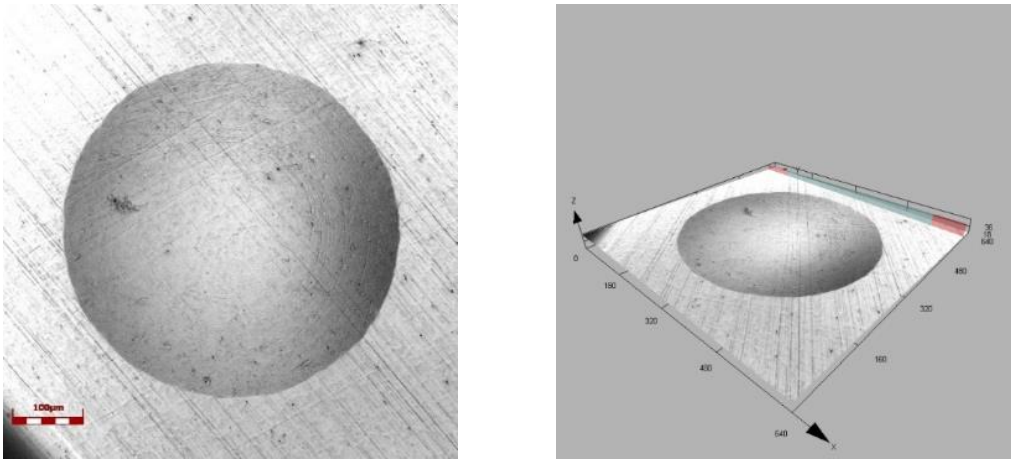

(a) (b)

Figure 26: Images from LEXT OLS4100 of the impression left in the specimen after indentation test for a steel alloy. (a) 2D Top view; (b) 3D view.

Two indentations are made for each of the configurations adopted for the Brinell hardness test. Thus, a total of six indentations is performed for each material assessed. Two measurements of the indentation profile at right angles are performed for every imprint. Therefore, considering the symmetry of the problem, 8 axisymmetric profiles become available from the measurements at each configuration load, as shown in Figure 27. Table 4 gives information about the mean indentation parameters measured for each profile configuration of Figure 27.

Table 4. Mean values for final indentation depth and radius.

Material	$\bar{h}_f$			$\bar{a}_p$		
	Load 1	Load 2	Load 3	Load 1	Load 2	Load 3
SAE 1524	54.5 μm	18.2 μm	9.1 μm	383.4 μm	232.1 μm	169.6 μm
SAE 4340 N	64.2 μm	21.7 μm	11.0 μm	412.3 μm	250.7 μm	183.9 μm
SAE 4340 A	91.5 μm	32.7 μm	16.7 μm	480.0 μm	295.6 μm	215.3 μm
Aluminum	128.6 μm	65.7 μm	35.2 μm	553.5 μm	404.3 μm	297.3 μm
Loads 1, 2, 3 are respectively 187.5 kgf, 62.5 kgf, and 31.25 kgf for the steel samples. For the aluminum sample, Loads 1, 2, 3 are respectively 62.5 kgf, 31.25 kgf, and 15.625 kgf.						

The standard deviation for the final depth measurements was in the order of 10^{-17}, which can be considered zero. For the indentation radius, the standard deviation was kept under 2 % for all indentations.

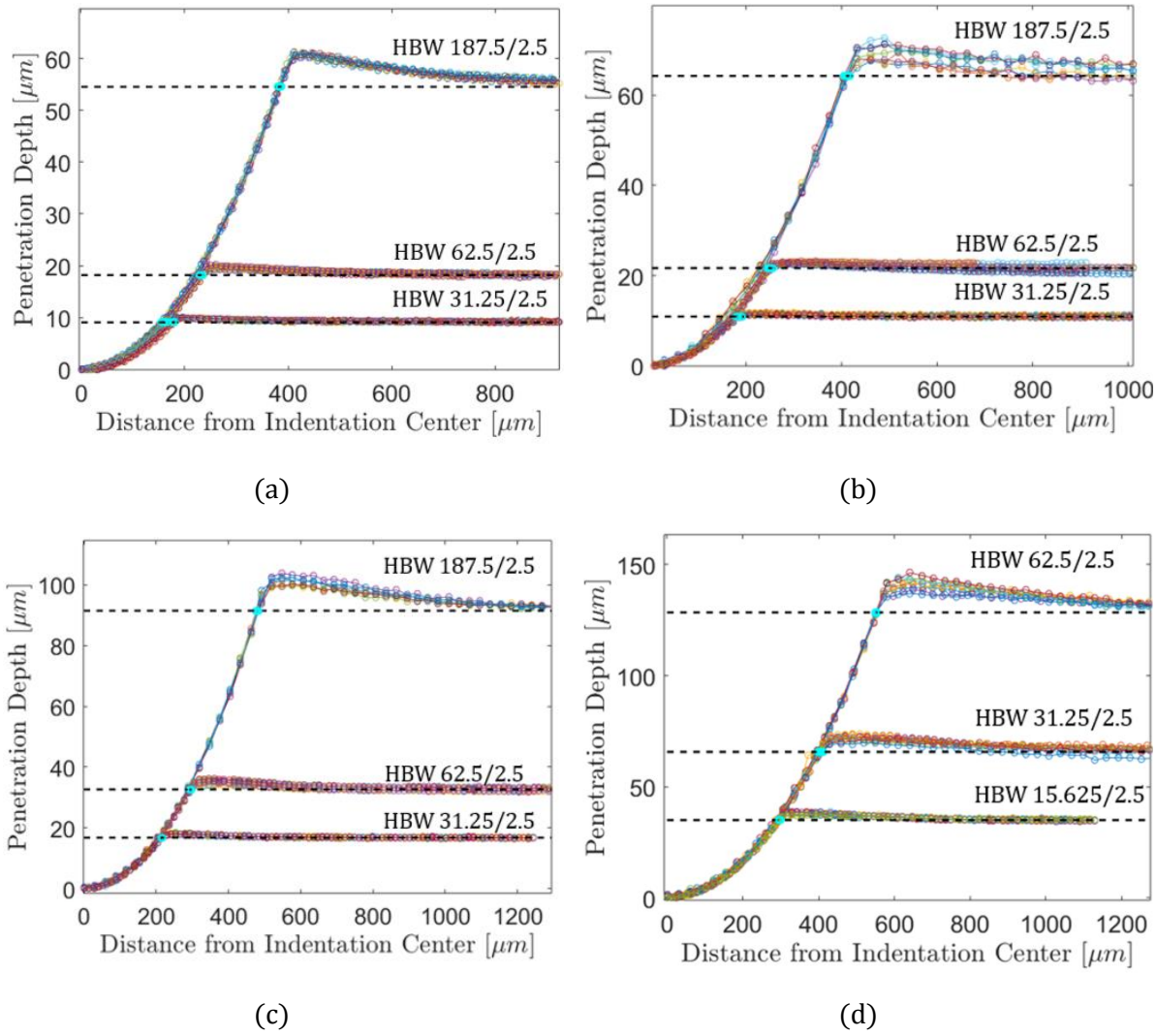

Figure 27. Resultant indentation profiles from Brinell hardness tests for the (a) SAE 1524, (b) SAE 4340 N, (c) SAE 4340 A, and (d) Aluminium 6101.

CHAPTER 4. NUMERICAL APPROACH

The indentation numerical analysis was carried out in a Finite Element Environment using ABAQUS. This software is licensed by Dassault Systèmes, 2012 and is widely used by engineers to solve diverse problems encompassing a wide range of industrial applications. This section presents a discussion on contact formulation and mesh convergence to decide the most suitable model configuration. Therefore, comparisons are made in terms of contact pressure, penetration depth and simulation time for procedures comprising the elastic and the elastic-plastic domain. For simulations purely elastic, the predicted output is compared to the analytical solution provided by Hertz's theory while the elastic-plastic numerical response is used for mesh convergence purposes. The elastic analyses are performed for a rigid indenter while the elastic-plastic assumes a Tungsten Carbide deformable indenter with Young's modulus of $645\ GPa$ and Poisson's ratio of 0.22. The specimen is a SAE 1524 U2 marine grade steel with Young's modulus of $200\ GPa$ and Poisson's ratio of 0.3.

4.1 Part Module

The sphere-flat contact is modeled in a 2D axisymmetric configuration. Both bodies are defined as deformable shells, however, in order to grant a rigid characteristic to the sphere, to its Young's modulus is assigned a value four orders greater than the specimen's Young's modulus (when applicable).

In Figure 28, it can be seen that both, specimen and indenter, were partitioned into different regions. It was done to facilitate meshing, making it possible to have suitable refinement in the contact region and, at the same time, to avoid unnecessary elements in other regions less affected by the stress field due to the contact.

a. **b.**

Figure 28. (a) Indenter; (b) Specimen.

4.2 Property Module

Each defined part indenter and specimen is made of a different material, both isotropic. Depending on the studied specimen, the indenter's material properties may change to guarantee it behaves as a rigid body when compared to the specimen, although it has been defined as a deformable body in the Part Module. To define the indenter's material properties is enough to consider it has only a linear elastic behavior, which is done by informing its Young's modulus and Poisson's ratio. To agree with the consideration of a rigid behavior for the indenter, whatever the specimen's Young's modulus is, the indenter's Young's modulus is four orders grater. The specimen may or may not behave elastically depending on the applied load it bears; therefore, it is necessary to perform an elastic-plastic analysis. The elastic-plastic analysis requires different fields depending on the plasticity model. For this case, besides the elastic definition, the classical metal plasticity model was adopted, which requires the knowledge of the stress-plastic strain data representing the material hardening behavior.

To every part must be assigned a material property. Once the materials are defined, sections are created to attend the parts' specifications. Since each part is made of one material kind, one section is created for each part and the correct material property is associated with its respective section. Respecting the pre-established conditions, the section is defined as homogeneous solid with a thickness of $1\ mm$.

4.3 Assembly Module

In the assembly, the part instances are created and positioned relative to each other in a global coordinate system, as shown in Figure 29, in a way where the lowest point of the indenter is in contact with the leftmost upper point of the specimen.

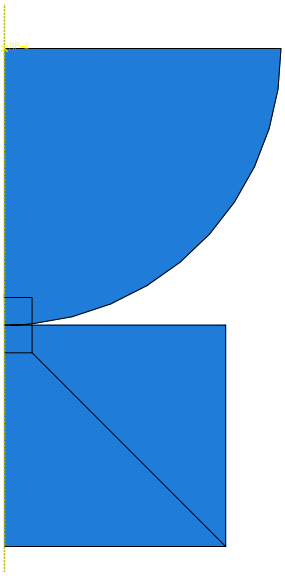

Figure 29. Contact configuration

4.4 Step Module

The simulation was carried out in three steps, defining in this manner the indentation test. In the initial step, the contact interaction between indenter and specimen is defined. The boundary conditions establish that the specimen is fully restrained at its base and that there is a symmetry about a plane X = constant. The next step, called Penetration, defines that the indenter can only move vertically relative to the specimen, deforming it. This vertical displacement is caused by a load applied to the indenter. Thereafter, the last step establishes that the indenter returns to its initial position, which allows the specimen to spring back so that the impression's maximum depth is not the final depth. The conditions of each step are propagated to the following step, with exception of the load established on the Penetration step that is not propagated to the next step.

During Penetration, instabilities in the model may arise causing local velocities to increase due mainly to mesh size and material behavior. If that happens, part of the strain energy needs to be dissipated, which can be achieved by adding a viscous force to the global equilibrium equations. This viscous force is proportional to a damping factor that in turn is proportional to the nodal velocities. Therefore, an automatic stabilization method with a constant damping factor is considered. However, defining the appropriate damping factor is not an easy task and depends on results from previous runs. An optimal damping factor is found when the converged solution is obtained and the dissipated stabilization energy is sufficiently small.

4.5 Interaction Module

The interaction module is used to define contact interactions, tie constraints and coupling constraints in the model. Addressing firstly the contact interactions, ABAQUS/Standard makes it possible to define contact in three main ways: general contact, contact pairs, and contact elements. The main approaches are the general contact and contact pairs, which use surfaces to define contact. When these two options are not suitable for the model, contact elements are provided, however, it is frequently recommended to avoid this last one.

The model analyzed here counts with the contact of two bodies defined as deformable in a two-dimensional configuration. The physical proximity of these two bodies in the assembly does not indicate interaction, therefore it is necessary to specify what kind of interaction exists between their surfaces and its properties. The contact pair is the most suitable type of interaction for this case because there are only two surfaces that may interact with each other. Also, having a pairwise specification of the contact results in a more robust analysis. To help the interaction, in the Part Module the indenter and the specimen were divided into regions for contact definition and efficiency purposes so that the extension of their contacting surfaces are appropriate.

4.5.1 Contact Formulation.

Once the contact interaction type is determined, the contact formulation defined subsequently will have a considerable impact on how the surfaces interact. It is based on master and slave definitions, contact discretization and tracking approach. Since the indenter is stiffer and may have coarser mesh, its contact surface is defined as master while the contact surface from the specimen acts as the slave surface. The contact discretization is defined as surface-to-surface and accounts for the way that conditional constraints are applied to interacting surfaces. For a given mesh refinement, the surface-to-surface discretization tends to provide more accurate stress and pressure results than the node-to-surface discretization. It happens because the surface-to-surface discretization resists penetrations in an average perspective over finite regions of the slave surface while the node-to-surface allows master nodes to penetrate the slave surface causing forces to concentrate at the slave nodes, resulting in an uneven distribution of pressure over the surface (ABAQUS/Standard User's Manual (6.14), 2014). Figure 30 shows the contact pressure response along the ratio of contact radius (r/a) for both contact discretization methods: surface-to-surface (a) and node-to-surface (b) for the same mesh refinement.

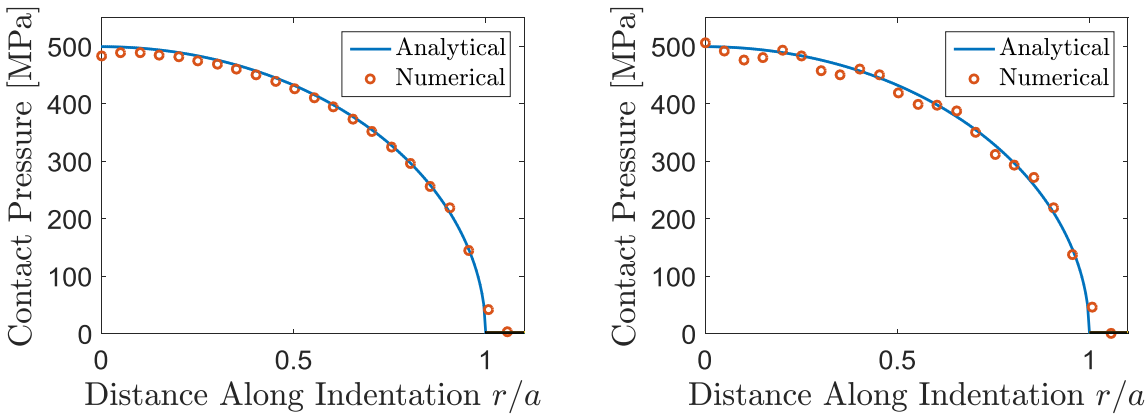

a. b.

Figure 30. Contact pressure response from surface-to-surface (a) and node-to-surface (b) contact discretization methods.

Along the numerical responses for contact pressure, the chart shows also the analytical result, as described by Hertz (Johnson, 1985; Williams and Dwyer-Joyce, 2001). While the surface-to-surface method provides contact pressure values uniformly distributed along the analytical solution, the node-to-surface method provides values fluctuating up and down near the analytical values.

To have a better idea of which discretization method is more appropriate, a point to point scalar relative error is calculated comparing the exact and numerical results, which is shown in Figure 31:

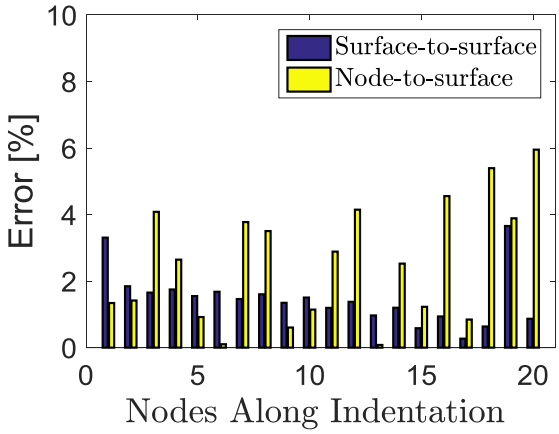

Figure 31. Contact pressure error for each node along indentation.

Figure 31 gives a clear understanding of the nodal pressure error distribution along indentation for the surface-to-surface and node-to-surface discretization methods. As can be seen, the node-to-surface nodal errors oscillate from 0.08% to almost 6 % in the contact pressure prediction, while the surface-to-surface nodal errors do not oscillate as much. Thus, to decide which model is more appropriate, a second error calculation is performed measuring the Frobenius norm of the error and exact vectors, as shown in Equation 69:

$$Error = \frac{\left\| R_i^{FEM} - R_i^{Exact} \right\|_F}{\left\| R_i^{Exact} \right\|_F} \tag{69}$$

where R_i^{FEM} and R_i^{Exact} are the numerical and the analytical responses for each analyzed node i. Equation 23 evaluates the numerical responses as a whole and yields a relative error of 1.69 % for the surface-to surface and 2.67 % for the node-to-surface contact discretization models. Since the computational time is not an issue for these analyses, the surface-to-surface contact discretization is the one that provides the best results.

The tracking approach can be defined as finite-sliding or small sliding, being responsible for dictating the relative motion relationships between the interacting surfaces. For the case where the relative motion of the contact surfaces is small, the assumption of a contact pair defined from the undeformed body configuration is acceptable and the small-sliding tracking approach can be used. However, when facing significative relative motion, the finite-sliding is preferable since the contact pair is determined upon the relative tangential motion of the contacting surfaces. Using the small-sliding tracking approach represents computational savings, but also means less accuracy. For the same analyzed model, the small sliding tracking approach yielded a pressure error of 1.58 % and 1: 14 of computational time while the finite sliding tracking approach yielded 1.47 % pressure error and 1: 17 of computational time.

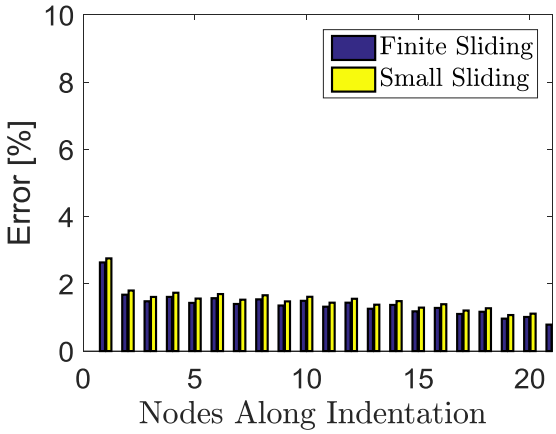

Figure 32. Contact pressure error for each node along indentation for finite and small sliding tracking approach.

For either case, when using the node-to-surface discretization method or the small sliding tracking approach, it was necessary to apply a damping factor to force convergence, otherwise, the simulation would fatally abort due to excessive node/element penetration. For all cases analyzed so far, the small sliding tracking approach was ignored. However, when the material being assessed is too soft and a high load is applied, convergence is more easily reached if a damping factor is considered for surface-to-surface discretization method as well.

The tracking approach analysis corroborates with the idea of frictionless tangential behavior, given that there is little discrepancy between the predicted output provided by finite and small sliding tracking approaches. For a more precise assumption, Figure 33 shows the material reaction response to the applied load for both approaches encompassing large deformations.

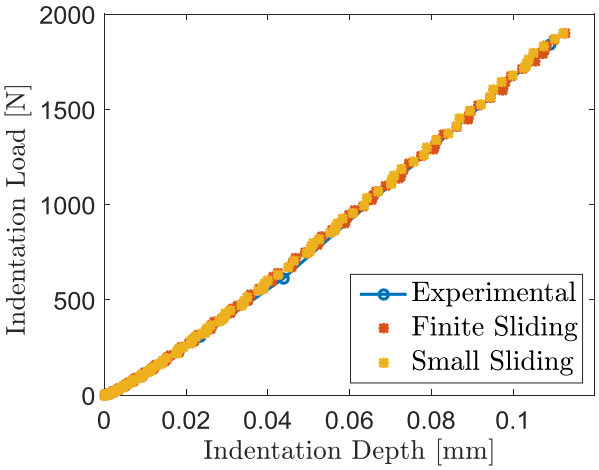

Figure 33. Material's response to applied load for finite and small sliding.

As can be seen, both tracking approaches provide very similar responses, presenting an error less than 3 % in comparison to the experimental data. From this perspective, it is reasonable to adopt a frictionless surface. However, even though the experiments performed by Tabor (1951) led him to conclude that surface roughness has little effect on hardness measurements, this is not the only aspect to be considered. As mentioned before, contact friction will affect the indentation results depending on material hardening characteristics and is more noticeable for low hardening materials.

Karthik (2012) points out that including an appropriate friction coefficient is important in two main aspects. First, to validate predicted FEM output with experimental load-depth data and, second, to formulate numerical methodologies for assessing material parameters based on loading-unloading curves. He limits his consideration to loading-unloading indentation data, but the same can be said regarding any predicted FEM output such as the indentation imprint and the strain distribution beneath the indenter.

However, Figure 12 and Figure 13 show that friction coefficients above 0.2 have no discernable influence on simulation outputs. For these reasons, the Coulomb friction contact is adopted, as employed in similar conditions by other authors (Taljat and Pharr, 2004; Karthik *et al.*, 2012). The friction coefficient is defined depending on the materials under analysis. Lee et al. (2005) state that friction coefficients range from 0.1 to 0.3 for contact of metals. For the case of tungsten carbide indenters to metal contact, friction coefficients are reported to be in the range of 0.4 to 0.6 (Smithells, 2004).

4.5.2 Contact Constraint Enforcement Methods.

One of the issues that arises when dealing with computational contact mechanics has to do with defining a relationship that establishes a rule for surface's motion. The chosen contact constraint enforcement method establishes how contact constraints are resolved in the analysis. Two main approaches are the Penalty and the Lagrange multiplier methods.

The penalty and the Lagrange multipliers methods provide the solution for the contact problem whose motion is constrained by the relationship expressed in Equation 70:

$$c(u) = h - u \geq 0, \tag{70}$$

where u is the displacement of a point mass and h the distance between the point mass and a rigid suport. The Lagrange multiplier method adds to the energy of the system a term that considers the constraining relationship of Equation 70, yielding the Equation 71:

$$\Pi(u, \lambda) = \frac{1}{2}ku^2 - mgu + \lambda c(u), \tag{71}$$

where λ is the Lagrange multiplier which is equivalent to the reaction force actuating on the point mass. From Equation 70 it is stated the equilibrium equation of a point mass and the fulfillment of Equation 71. The Penalty method adds a penalty term to the energy of the system. This term works like a spring of stiffness ϵ acting in the contact interface. The governing equation for this method is presented in Equation 72

$$\Pi(u) = \frac{1}{2}ku^2 - mgu + \frac{1}{2}\epsilon[c(u)]^2, \forall \epsilon > 0. \tag{72}$$

The penalty method in its formulation allows penetration whose amount depends on the stiffness that the penalty term grants to the system. The kinematical constraint expression (Equation 70) is fulfilled when $\epsilon \to \infty$, yielding the same solution given by the Lagrange multiplier method (Equation 71) (Wriggers, 2006). For this reason, the Lagrange multiplier method usually add more degrees of freedom to the model and requires more iterations to achieve the solution, hence the computational costs increase.

For protection and efficiency against numerical errors related to ill-conditioning, that can occur if a high contact stiffness is in effect, the Augmented Lagrange Multiplier method is adopted, which uses the same kind of stiff approximation as the penalty method but with augmented iterations to improve the accuracy of the approximation.

4.5.3 Constraints

Tie and coupling constraints are used in the model to define the relationships among part instances and references points. The tie constraint is used from the necessity to fuse two part-instances that belong to the same body but with dissimilar meshes, as can be seen in Figure 34 for the indenter (a) and the specimen (b):

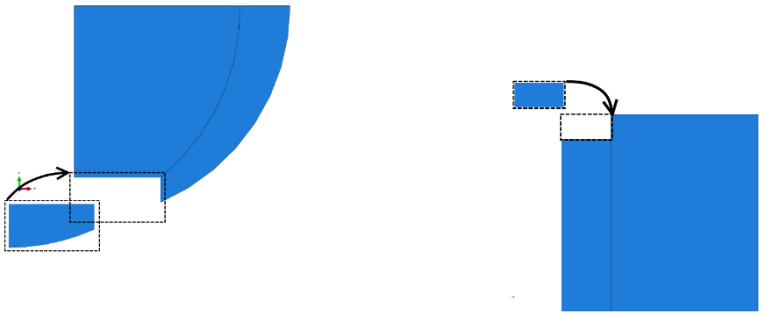

a. b.

Figure 34. Tie constraints applied to the indenter (a) and the specimen (b)

There are two references points whose motion constrain the motion of two surfaces, thus the necessity to use the coupling constraint to perform this task. The first reference point is used to transfer a concentrated force to the whole model by applying it to a reference point with a coupling constraint relationship with the indenter's upper surface, as shown in Figure 35.a. Second, the bottom of the specimen is totally constrained with an encastre, However, for output readings purposes, this condition is applied to the reference point and a coupling constraint between this point and the specimen's bottom surface is applied, as shown in Figure 35.b.

a. b.

Figure 35. Coupling constraints applied to the indenter (a) and to the specimen (b).

4.6 Load Module

Load and boundary conditions are applied to the model, and since they are step-dependent objects it is necessary to specify in which steps they are active, as it has been described in the Step Module section. At the initial step, the encastre boundary condition is applied to a reference point that is coupled to the specimen's bottom surface (Figure 35.b). The axisymmetry boundary condition is applied to the specimen's and indenter's surfaces lying on the symmetry line. The indenter's initial position is defined by allowing its motion in the vertical direction only. This is achieved by constraining the motion of the reference point that is coupled to the indenter's upper surface (Figure 35.a) in the horizontal direction and from rotating about the z-axis. In the subsequent step, a concentrated force is applied to the reference point coupled to the indenter's upper surface so that the load is transmitted to the whole model. The last step consists in bringing the indenter back to its initial position allowing the specimen to spring back, having an elastic recovery due to unloading.

4.7 Mesh Module

The process of generating meshes requires a convergence study to guarantee the needs of the analysis. First, for efficiency purposes, a region of contact was defined in the indenter and in the specimen to make it possible to assign dissimilar meshes to the same body without the need of a zone of transition between them, as shown in Figure 36.

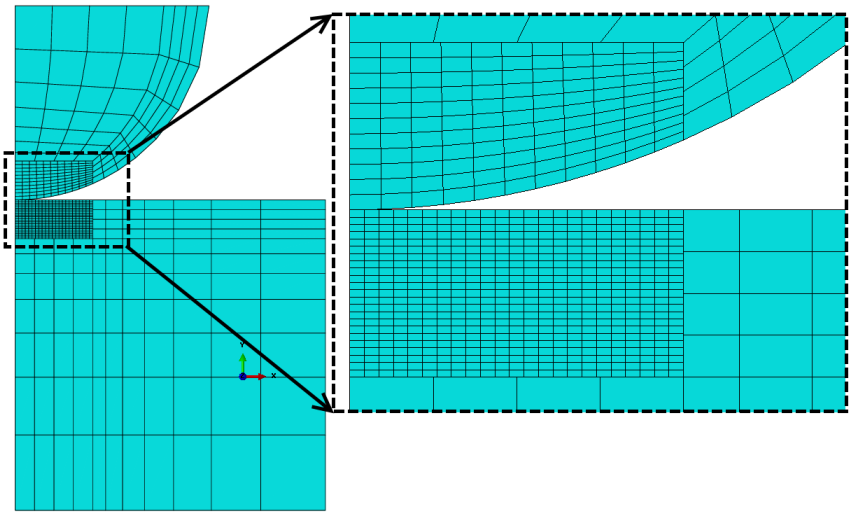

Figure 36. Meshing Assignment.

As it can be seen in Figure 36, the contact zone has a finer mesh than the other regions and the indenter's mesh is slightly coarser than the specimen's due to its greater stiffness and to minimize the penetration of the master surface nodes in case of choosing the node-to-surface contact. The number of nodes and elements varies depending on the contact length, which in turn depends on the load applied, material definitions and if the analysis is purely elastic or elastic-plastic. In general, the contact length is estimated analytically, when dealing with elastic analysis, or experimentally, when the analysis undergoes plastic deformations. However, despite the length of contact, the coarser mesh is programmed in a way where the elements in the vicinity of the contact zone have five times the size of the finer mesh with a bias applied to make it increase in size until reaching an element size five times greater than the first one defined for the coarser mesh.

Using the surface-to-surface contact discretization method, a mesh convergence assessment is carried out for two element types (Table 5) and five mesh refinement levels of the contact zone. The two element types are:

Table 5. Element types description.

Element Type	Description
CAX4R	A 4-node bilinear axisymmetric quadrilateral, reduced integration, hourglass control.
CAX4	A 4-node bilinear axisymmetric quadrilateral.

The refinement level takes into consideration the experimental contact length obtained from a Brinell Hardness test HBW 187.5/2.5 that yielded an indentation diameter of $1.03\ mm$. The number of

nodes in the contact zone depends of two definitions: the length of the contact region and the mesh element size. For a better analysis, the length of the contact region is not defined as being of the same as the experimental one but assumes a size two times longer than the analytical contact length. Once the length of the contact region is defined, the number of nodes in the contact region depends only of the mesh element size. The equivalent plastic strain and the von Mises equivalent stress convergence are the assessed variables used to define the best refinement level. To capture its distribution along the contact, the mesh is initially built with an element size ten times smaller than the adopted contact length, then fifteen, twenty, twenty-five, and thirty. For convergence purposes, computational time savings and master-slave definitions, the mesh element size in the indenter's contact region is 50 % longer than the specimen's.

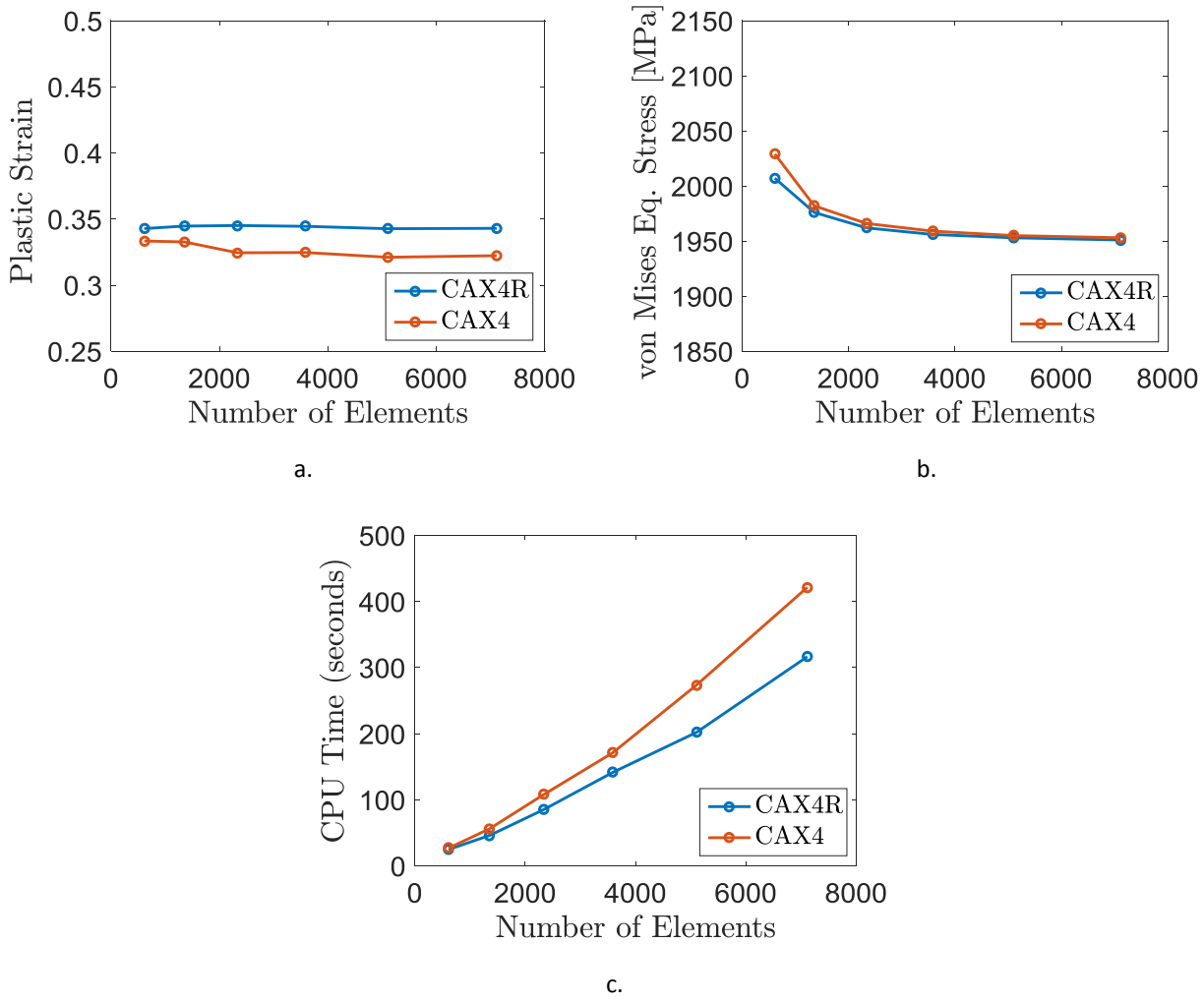

Figure 37. Mesh Convergence analysis in terms of plastic strain (a), von Mises equivalent stress (b) and CPU time (c).

Figure 37 shows that, even though the full integration is more expensive than the reduced integration, both converge to the same amount of von Mises equivalent stress and keep approximate

amounts of equivalent plastic strain for different refinement levels. On the other hand, when going from reduced to full integration, the discrepancy between them is not significative enough to pay back the computational cost when using full integration. Therefore, the mesh configuration that yields the appropriate response in a suitable amount of time is composed of 2335 4-node bilinear axisymmetric quadrilateral elements with reduced integration.

4.8 Parameter Identification

Initially, it is necessary to stipulate arbitrary values for the parameters being assessed. This initial parameter set is used to generate the first trial hardening curve. The generated hardening curve is read by ABAQUS and assigned to the appropriate part in the model. The indentation model is run and an output data with the predicted indentation curve is provided. With the data provided, the optimization algorithm is called to compare experimental and numerical responses and then decide if the parameters provided are appropriated.

The optimum stress-strain curve is obtained in the optimization process as new values for the assessed parameters are being provided at each iteration. From these new values, a new hardening curve is generated and inserted in the FEM model to simulate the Brinell hardness test. Once the stopping criterion is satisfied, the routine is stopped with the optimum parameters values defined. The complete routine is presented in the flowchart in Figure 38. The simulation was carried out in a Windows 8.1 Single Language operational system, 64 bits, x64 Intel(R) Core (TM) i7 processor, CPU @ 3.40 GHz, 14 GB RAM.

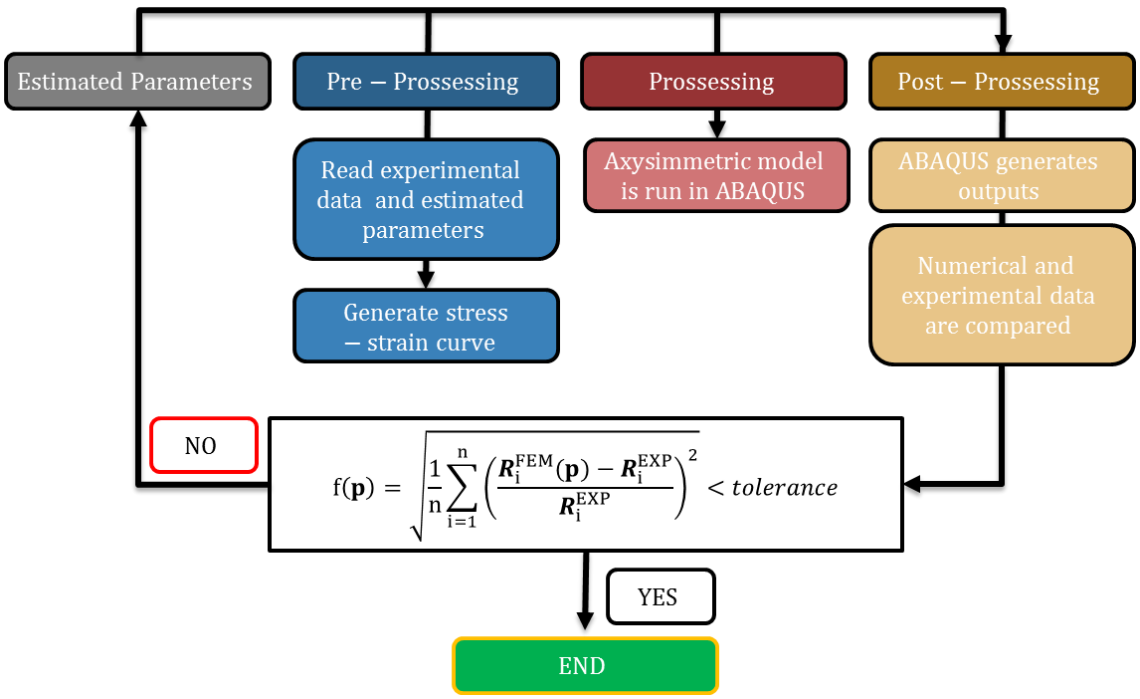

Figure 38: Optimization Process.

CHAPTER 5. EMPIRICAL CORRELATION OF SPHERICAL INDENTATION TESTS TO STRESS-STRAIN DATA

Many advocate that indentation tests have the potential to replace the traditional uniaxial test due to its versatility and convenience (Giannakopoulos and Suresh, 1999; Ahn and Kwon, 2001; Bucaille *et al.*, 2003; Guillonneau *et al.*, 2012; Kang, 2013; Fu *et al.*, 2015; Li *et al.*, 2016; Dean and Clyne, 2017). For these reasons, efforts have been made to represent the stress-strain relationship by means of indentation tests. Overall, these efforts fall into two main categories: the development of analytical relationships based on empirical observations and the development of inverse methods aided by FEM analysis and optimization algorithms. The first category is discussed in this chapter, where plastic stress-strain points are obtained from the concept of a representative stress-strain, as defined by Tabor (1951).

5.1 Representative stress-strain curves by spherical indentation

The spherical indenter has the advantage to not produce geometrically similar indentations, i.e., the effective plastic strain changes as a function of the indentation depth. Therefore, the contact angle β between the indenter and specimen from Equation 20 must change as a function of the indentation depth. Since the indentation has a chordal radius a and radius of curvature R, the resultant spherical shape can be defined by the ratio a/R, which defines the contact angle β. Therefore, Equation 20 assumes the form expressed in Equation 73:

$$\tan(\beta) = \frac{a}{R}. \tag{73}$$

All the materials are assessed based on the contact parameters measured after unloading since a means to acquire data at the loaded state is unavailable. However, to have an idea of the discrepancy between the measurements between these two states, the SAE 1524 is also numerically assessed. This numerical analysis is carried out so that the contact parameters can be measured at the loaded state and then compared to the unloaded state. The indentation profiles are generated using finite element analysis from a known stress-strain relationship. The method is assessed by verifying if the empirical relationships are capable of regenerating the stress-strain relationship inserted in the model.

In this contribution, the representative stress technique is assessed for three configurations of the Brinell hardness test. They are the HBW 187.5/2.5, HBW 62.5/2.5, and HBW 31.25/2.5 for the steel samples. For the aluminum sample, they are the HBW 62.5/2.5, HBW 31.25/2.5, and HBW 15.625/2.5. Stress-strain points are generated by measuring the contact parameters from each indentation. This

assessment follows the Dutch IIT guideline for evaluating tensile properties of metallic materials by means of instrumented indentation tests (ISO, 2008).

5.1.1 Determining the contact parameters from FEM analysis for the SAE 1524

Figure 39 shows the predicted indentation state at maximum load for each configuration of the Brinell hardness test run for the SAE 1524. They represent different load states in the regime of full plasticity. The indentation parameters are measured to later be inserted into Equations 20 and 22 and produce stress-strain points.

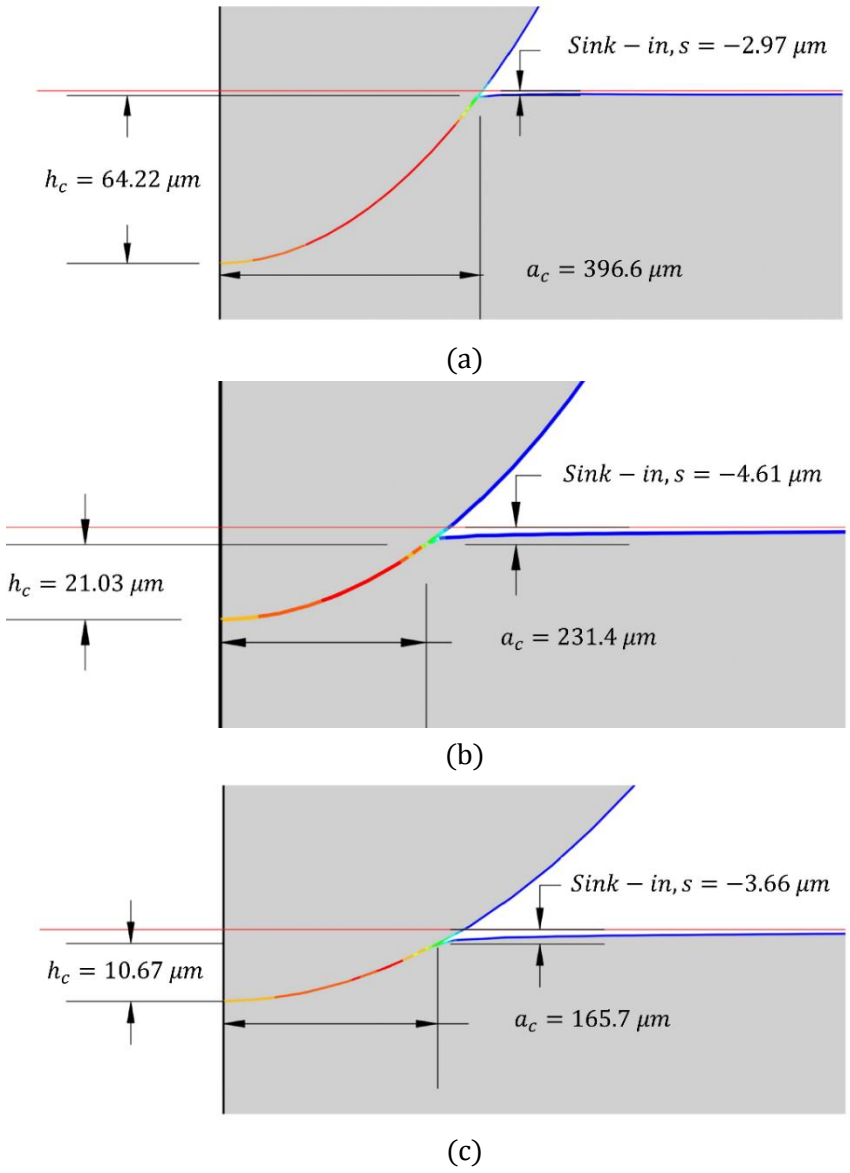

Figure 39. Predicted indentation profile parameters at a load of 187.5 kgf for SAE 1524.

Next, pile-up, sink-in and the elastic deflection phenomena are neglected while the same profile parameters are measured from the unloaded state. Figure 40 shows the predicted indentation state after unloading for each configuration of the Brinell hardness test run for the SAE 1524.

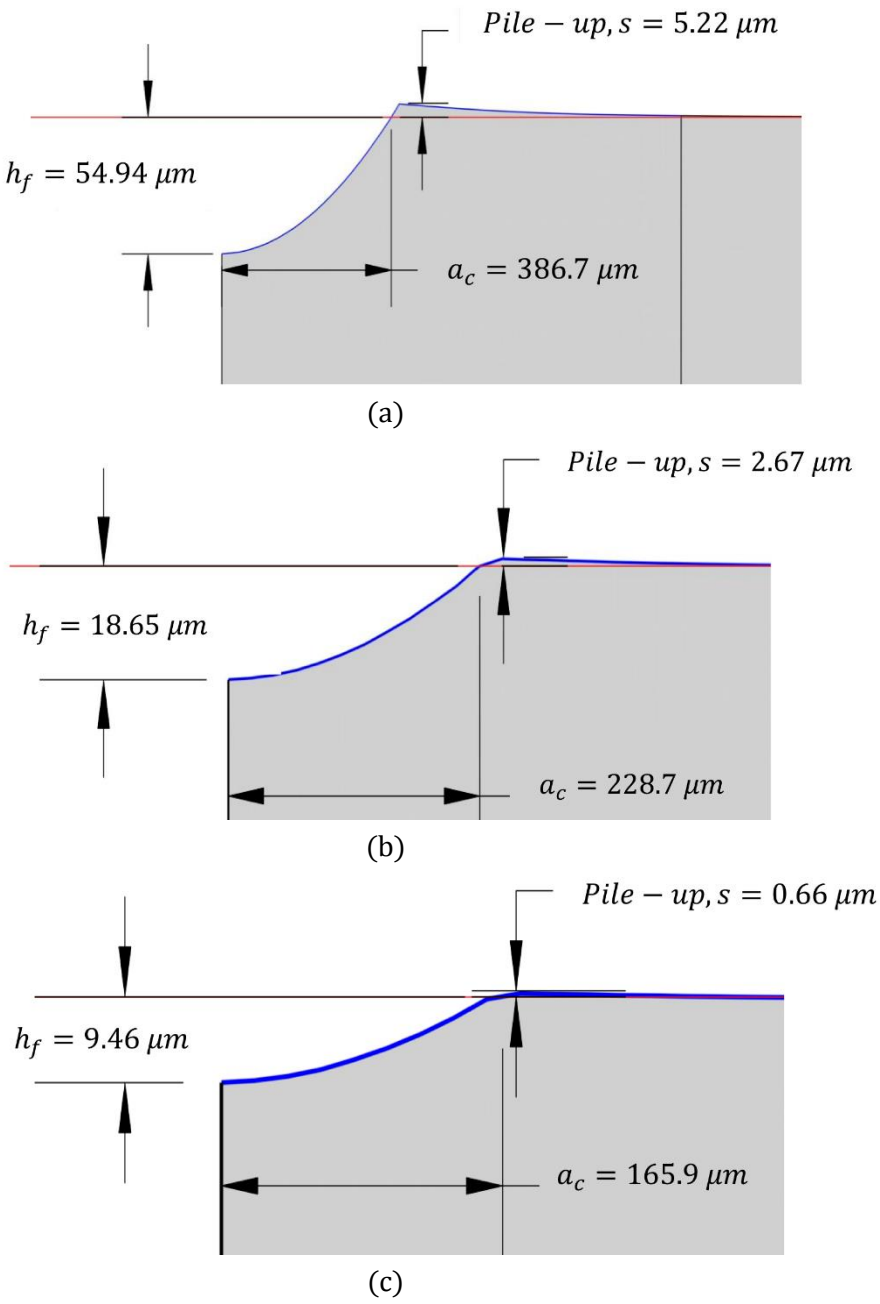

Figure 40. Predicted indentation profile parameters after unloading for (a) 187.5 kgf, (b) 62.5, and (c) 31.25 for SAE 1524.

Figure 39 and Figure 40 show the predicted indentation profile parameters in the loaded and unloaded states for three configurations of the Brinell hardness test: HBW 187.5/2.5, HBW 62.5/2.5, and HBW 31.25/2.5. The resultant indentation profile in the loaded and unloaded state present considerable difference due to elastic recovery. When loaded, the material presented the sink-in

phenomenon in all three configurations. However, the elastic recovery was able to revert this situation and leave a piled-up profile. The errors in the measurement of these two parameters were of 2.5 %, 1.16 %, and 0.09 % respectively to the configurations in the presented order. The error is smaller the lower are the loads applied. However, higher loads are needed to cover a wider range of the stress-strain curve and to maintain the indentation in the regime of full plasticity.

5.1.2 Determining the contact parameters from measurements of experimental indentation profiles

Figure 41 shows the experimental indentation profiles and the contact parameters measured after unloading for (a) SAE 1524, (b) SAE 4340 N, (c) SAE 4340 A, and (d) Aluminum 6101.

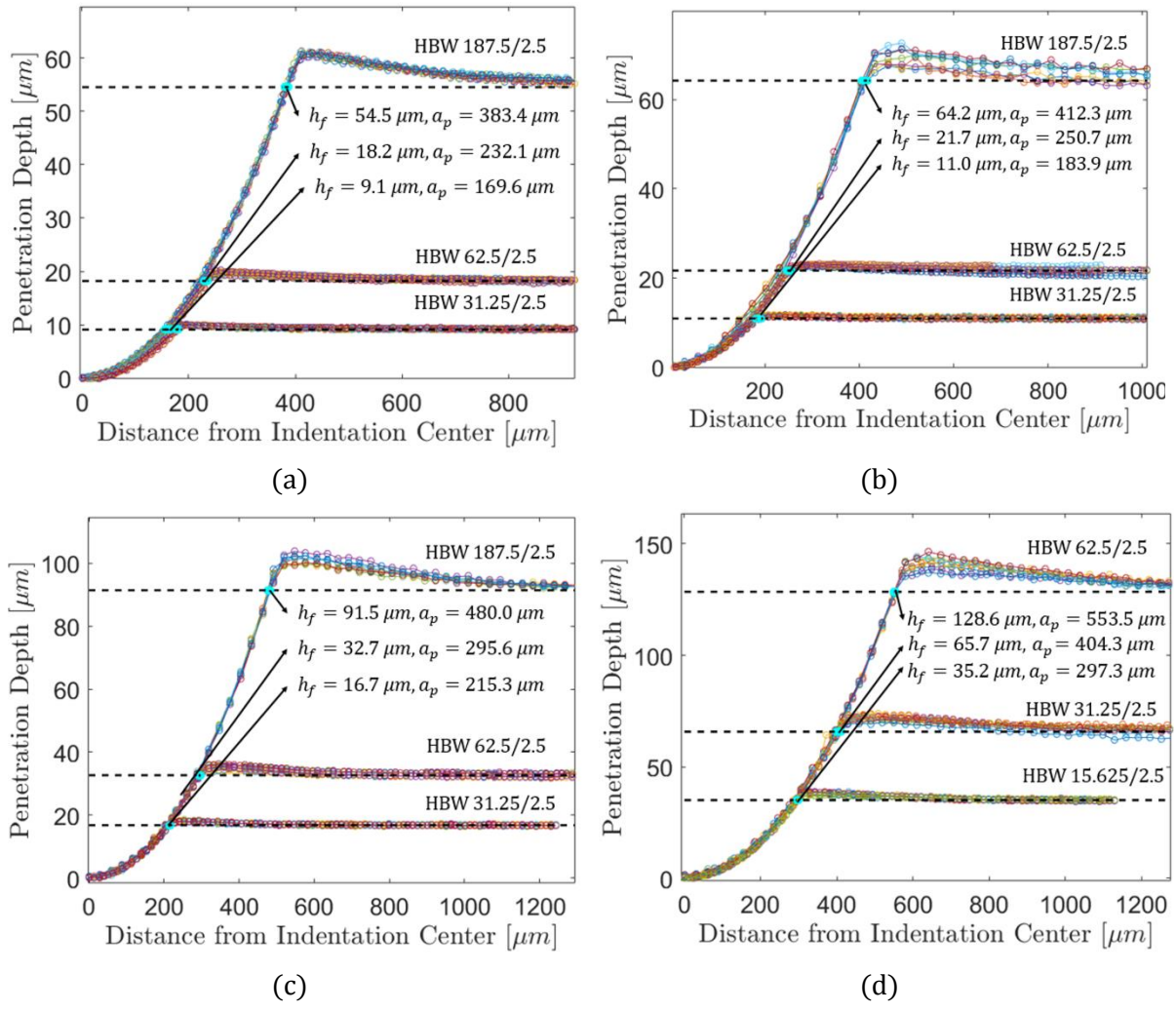

Figure 41. Experimental profiles and contact parameters for (a) SAE 1524, (b) SAE 4340 N, (c) SAE 4340 A, and (d) Aluminium 6101.

The real contact parameters h_c and a_c are measured at full load. The same is not possible when only the experimental unloaded profile is available, which is the case of most traditional hardness test. Here,

the contact parameters are determined by measuring the final depth (h_f) and the radius of the indentation (a_p) resulted from plastic deformation. In section 5.1.3, it will be used to correlate the indentation tests to the representative stress-strain relationship of the materials assessed. For the SAE 1524, it also provides a means of comparison for the numerical indentation profiles shown in section 5.1.1.

Even though Equation 32 presents a workaround to obtain the real contact radius from the indentation morphology, the strain hardening exponent of the material must be known. Unfortunately, for most cases, this information is not available. Conversely, it is one of the parameters to be determined in analysis such as this.

5.1.3 Defining the true stress-strain relationship

For the SAE 1524, Table 6 shows the numerical and experimental representative stress-strain points calculated using Equations 20 and 22. The stress-strain points are categorized into loaded (Figure 39), unloaded (Figure 40), and experimental (Figure 41.a) referencing to the profiles used to measure the contact parameters h_c and a_c. Plastic constraint factors (Ψ) of 3.0 and 2.8 are used in the calculations.

Table 6. Representative stress-strain relationship calculated from Brinell hardness tests for the SAE 1524.

HBW	Loaded		Unloaded		Experimental	
	σ_{rep}[MPa]	ε_{rep} [%]	σ_{rep} [MPa]	ε_{rep} [%]	σ_{rep}[MPa]	ε_{rep} [%]
$\Psi = 3.0$						
187.5/2.5	1236.9	6.35	1301.1	6.19	1312.0	6.16
62.5/2.5	1211.2	3.70	1240.0	3.66	1238.9	3.66
31.25/2.5	1181.1	2.65	1178.2	2.65	1179.6	2.65
$\Psi = 2.8$						
187.5/2.5	1325.2	6.35	1394.1	6.19	1405.7	6.16
62.5/2.5	1297.7	3.70	1328.6	3.66	1327.4	3.66
31.25/2.5	1265.4	2.65	1262.4	2.65	1263.9	2.65

The data obtained numerically and experimentally for the unloaded state match each other with an error of less than 0.1 % for the worst case (HWB 187.5/2.5). The representative stress-strain points calculated at the unloaded state provided a better approximation to the uniaxial stress-strain curve than the points obtained at full load if $\Psi = 3.0$ is used. This can be visualized by comparing Figure 42 with Figure 43.

For the other materials, only experimental data is available. Thus, the impression parameters obtained from them are used to calculate the representation stress-strain points using Equations 20 and 22.

Table 7. Representative stress-strain relationship calculated from Brinell hardness tests for the SAE 4340 N

HBW	$\Psi = 3.0$	$\Psi = 2.8$	ε_{rep} [%]
	σ_{rep} [MPa]	σ_{rep} [MPa]	
187.5/2.5	1144.6	1226.3	6.60
62.5/2.5	1031.9	1105.6	4.01
31.25/2.5	958.9	1027.3	2.94

Table 8. Representative stress-strain relationship calculated from Brinell hardness tests for the SAE 4340 A

HBW	$\Psi = 3.0$	$\Psi = 2.8$	ε_{rep} [%]
	σ_{rep} [MPa]	σ_{rep} [MPa]	
187.5/2.5	844.5	904.8	7.68
62.5/2.5	742.2	795.2	4.73
31.25/2.5	699.6	749.5	3.44

Table 9. Representative stress-strain relationship calculated from Brinell hardness tests for the Aluminum 6101

HBW	$\Psi = 3.0$	$\Psi = 2.8$	ε_{rep} [%]
	σ_{rep} [MPa]	σ_{rep} [MPa]	
187.5/2.5	211.7	226.8	8.86
62.5/2.5	198.4	212.5	6.47
31.25/2.5	183.4	196.5	4.76

For the SAE 1524, Figure 42 and Figure 43 show the representative stress-strain points obtained numerically, at the loaded and unloaded states, and experimentally, at the unloaded state. Figure 42 is generated using $\Psi = 3.0$, while and Figure 43 is generated using $\Psi = 2.8$. Figure 44 shows the representative stress-strain points for the SAE 4340 N, Figure 45 for the SAE 4340 A, and Figure 46 for the Aluminum 6101. For these materials, the representative stress-strain points calculated using $\Psi = 3.0$ and $\Psi = 2.8$ are shown in the same chart since they were not numerically assessed. Each chart also shows the hardening curves obtained from the uniaxial test (Figure 22) plotted against their respective representative stress-strain points determined by Equations 20 and 22. Thus, the representative stress-strain approach can be evaluated for each material.

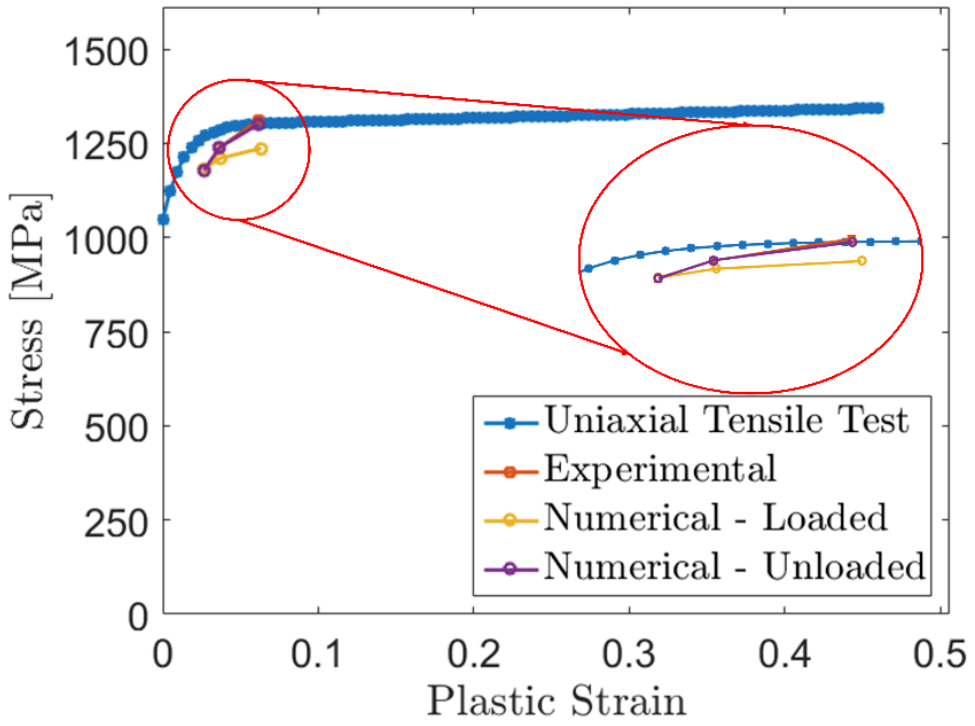

Figure 42. Representative stress-strain points ($\Psi = 3.0$) plotted in comparison with the hardening curve obtained from tensile tests.

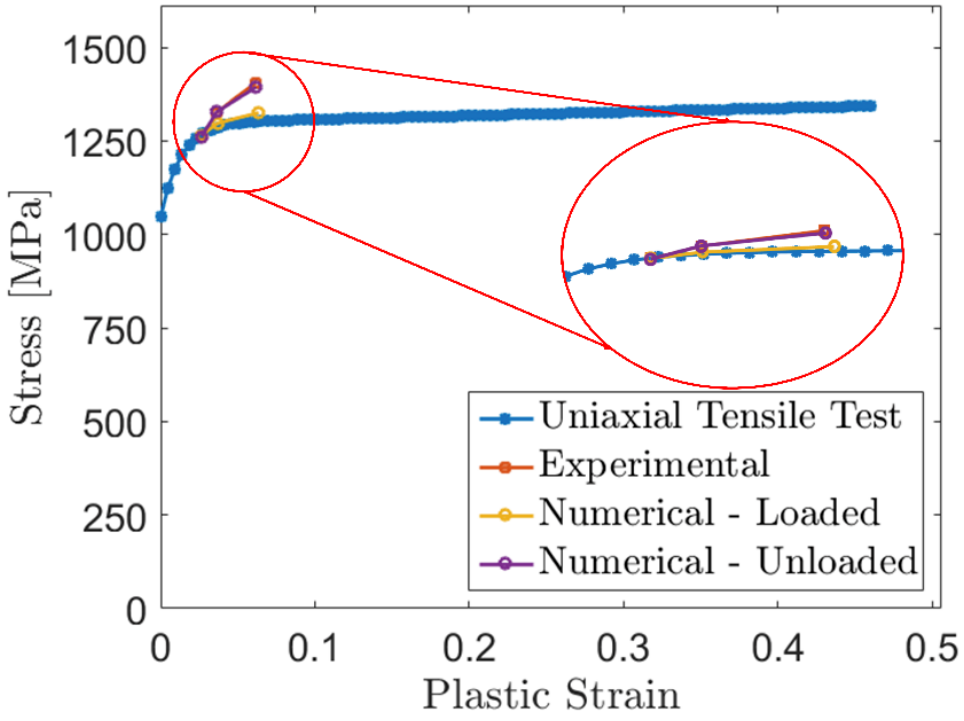

Figure 43. Representative stress-strain points ($\Psi = 2.8$) plotted in comparison with the hardening curve obtained from tensile tests.

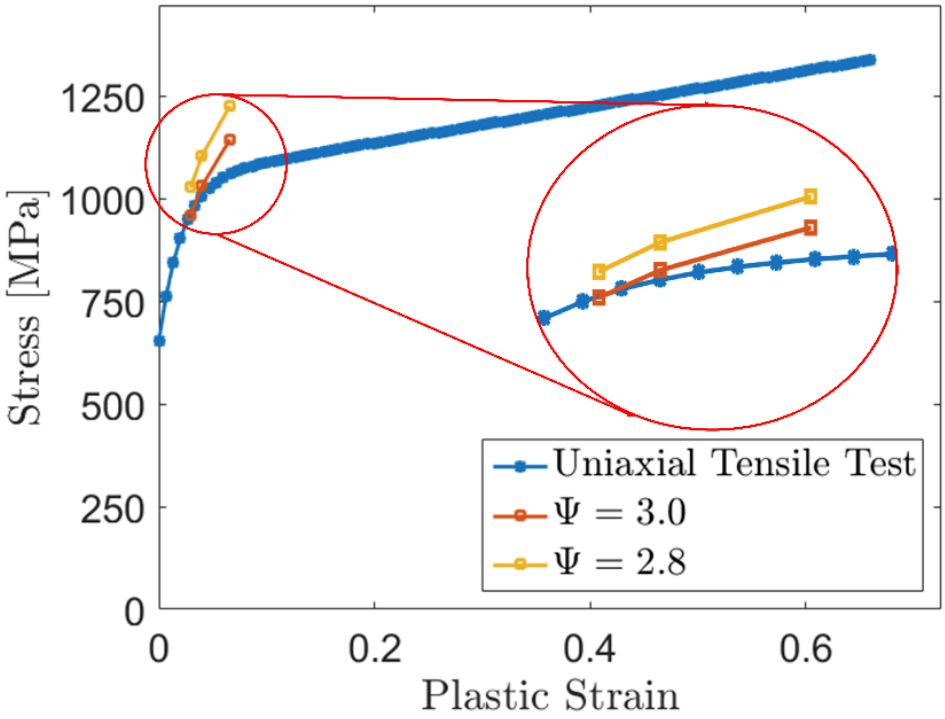

Figure 44. Representative stress-strain points plotted in comparison with the hardening curve obtained from tensile tests for SAE 4340 N.

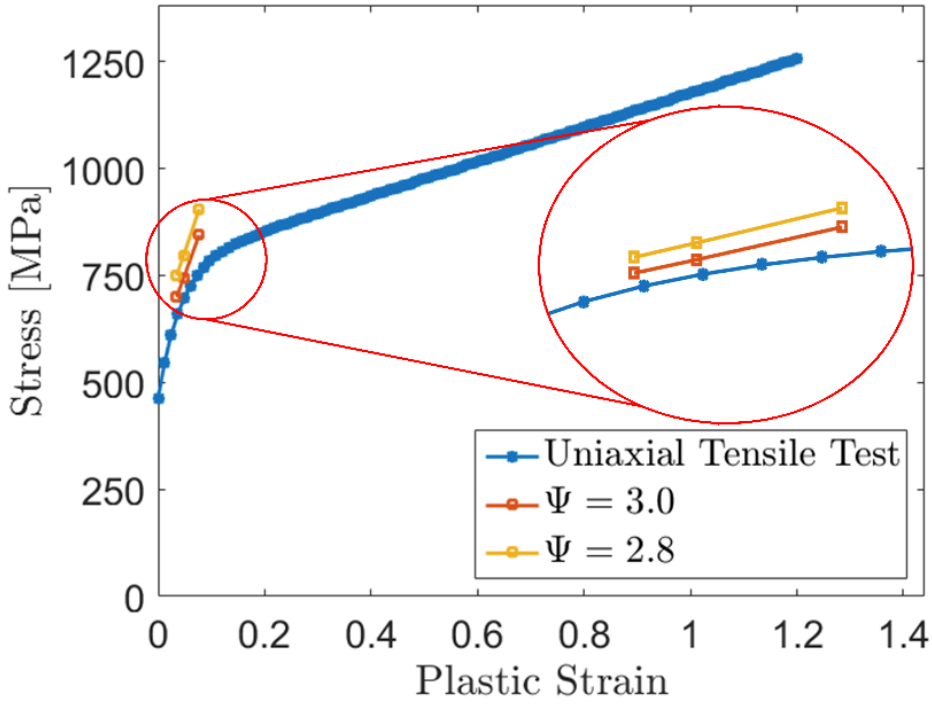

Figure 45. Representative stress-strain points plotted in comparison with the hardening curve obtained from tensile tests for SAE 4340 A.

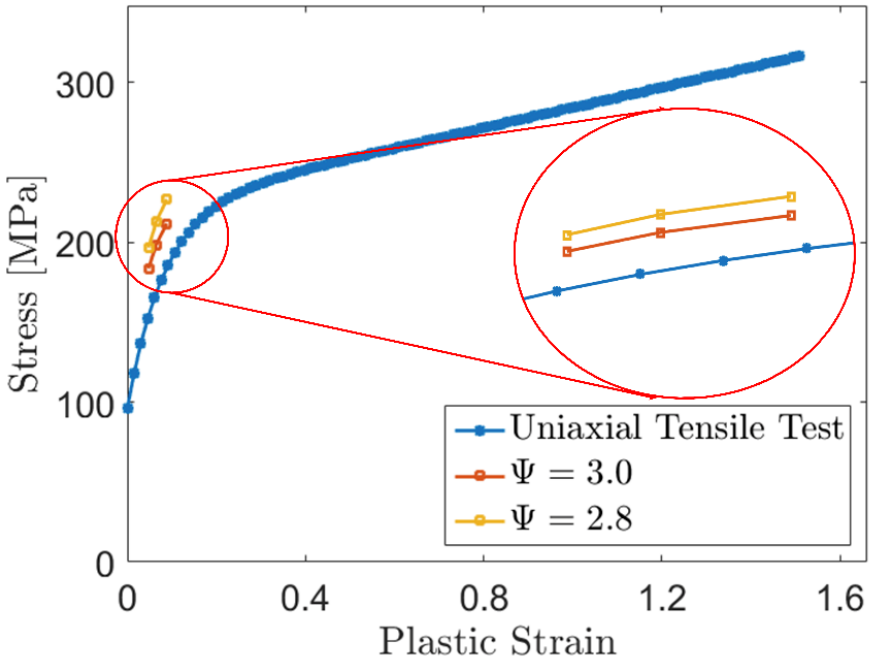

Figure 46. Representative stress-strain points plotted in comparison with the hardening curve obtained from tensile tests for Aluminum 6101.

The last step in the representative stress-strain approach would be to fit the representative stress-strain points to a constitutive hardening model, such as the ones shown in Table 1. Unfortunately, no realistic parameters can be drawn from such a small dataset. It would be necessary a cycling depth- or force-controlled indentation test to acquire enough representative stress-strain points to accomplish this task.

This analysis then shows the applicability of the empirical-analytical relationship devised by Tabor (1951). It considerably relies on the assumption of a correct plastic constraint factor. For most metals, Ψ ranges from 2.8 to 3.0. However, such a small range can lead to considerable error in the determination of the hardening curve. The representative stress-strain points were calculated considering $\Psi = 3.0$ and $\Psi = 2.8$ and yielded considerable distinct values (Table 6 to Table 9). If the plastic constraint factor is not appropriately chosen, the conclusions can be reverted due to this small variation.

A good aspect of this method is that there is no need for computational analysis. However, this method carries many uncertainties while it relies on empirical relationships with considerable variation of their constants. The main limitation dwells on how to determine in which regime the indentation is located. If in the elastic-plastic transition, it varies according to $\ln(\Gamma)$, which turns out to be a function of the representative stress. In the state where elastic effects are essentially negligible, the plastic constraint factor Ψ varies from 2.8 to 3.0 for most metals. Therefore, even if the indentation is in the regime of full plasticity, a small variation of the plastic constraint factor can lead to considerable discrepancies between calculated representative points and the stress-strain curve from a tensile test.

CHAPTER 6. ASSESSMENT OF INDENTATION HARDNESS TESTS FOR EXTRACTION OF PLASTICITY PARAMETERS OF METALLIC MATERIALS

CHAPTER 5 was introduced addressing the potential that many researchers think that indentation techniques have to replace the traditional uniaxial test. As said in that context, their efforts fall into two main categories: the development of analytical relationships based on empirical observations and the development of inverse methods aided by FEM analysis and optimization algorithms. The first category was addressed in the previous chapter through the concept of representative stress. Here, two aproaches that fall into the second category are discussed.

Finite element analysis has been extensively used to predict material response to a plethora of loading conditions. To accomplish this task, information about the material must be available. This information is inserted into the FEM model and the structural response is predicted. Extracting plasticity parameters of metals by means of indentation tests is exactly the inverse problem. The material response is known, which is represented by measurable information such as the load-depth curve, and the information about the material behavior is sought. An illustration of this problem is shown in Figure 47.

The two approaches presented here make use of an inverse methodology where experimental data from indentation tests are produced as a means of comparison for the predicted numerical outputs. The difference between them is the data being assessed. The first approach uses the loading-depth response of the material while the second approach uses the resultant indentation profile. Both approaches are novelties presented here and infers the material stress-strain relationship from the geometrical aspects of the resultant indentation profile. The inverse problem for both approaches is illustrated in Figure 47.

Repeated FEM analysis must be conducted in order to recover the material stress-strain information that led to the resultant material response. The FEM analysis is conducted by an optimization algorithm that assesses the predicted output against experimental data. At each iteration, the optimization algorithm is responsible for providing a new stress-strain curve that is fed back into the model. This process is repeated until predicted FEM output and the equivalent experimental data matches each other under a predetermined tolerance.

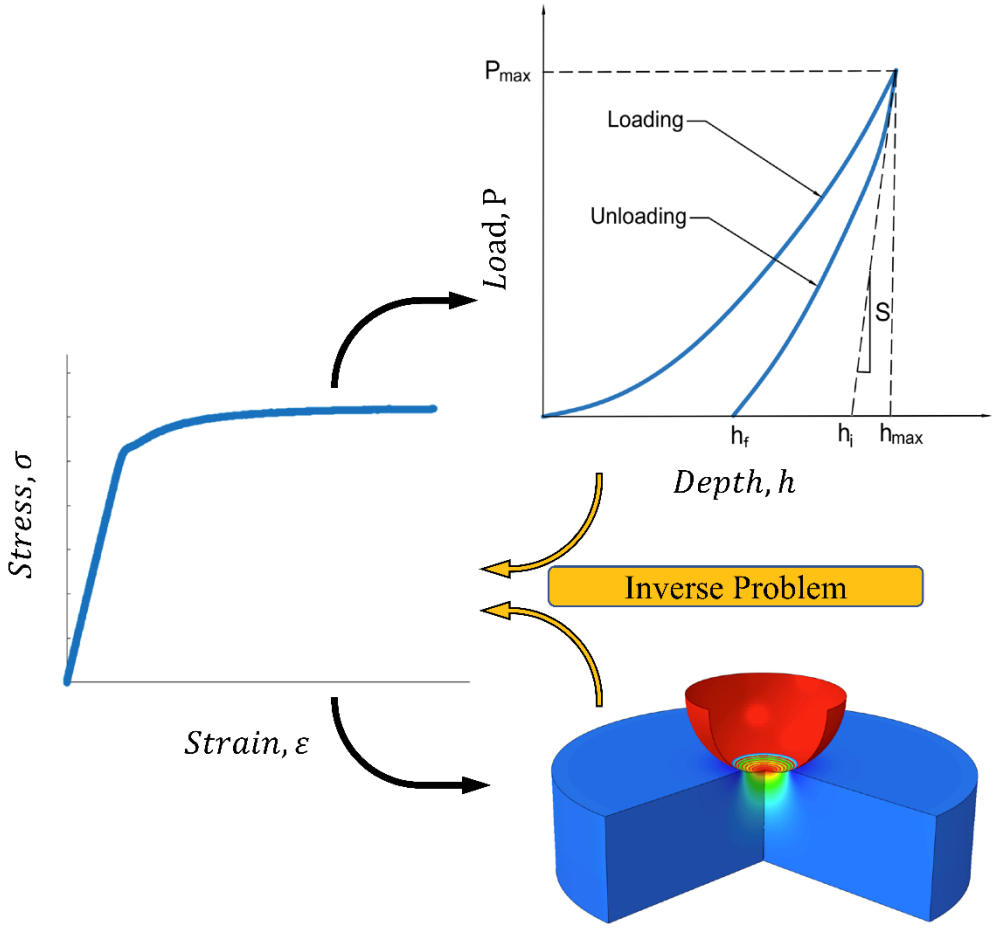

Figure 47. Inverse problem.

The relationship between the stress-strain fields is represented by a constitutive hardening model. This constitutive hardening model is characterized via a set of fitting parameters. The Kleinermann-Ponthot model is chosen, which gives the stress as a function of four parameters (σ_{y0}, ξ, σ_{∞}, and δ), as expressed in Equation 40.

6.1 Extraction of plasticity parameters from indentation load-depth curve.

The material response to an instrumented indentation test provides a rich data set like the one shown in Figure 48.a. Unfortunately, an equivalent dataset cannot be drawn from traditional hardness test devices. For this analysis, instead, the specimens are submitted to indentations covering three configurations of the Brinell hardness test. They are the HBW 187.5/2.5, HBW 62.5/2.5, and HBW 31.25/2.5, for the steel samples. For the aluminum sample, they are the HBW 62.5/2.5, HBW 31.25/2.5, and HBW 15.625/2.5. Because the indentation depth at maximum load is not available, the indentation depth is measured after the elastic recovery. The final indentation depth measured is then correlated to the load that led to it, as shown in Figure 48.

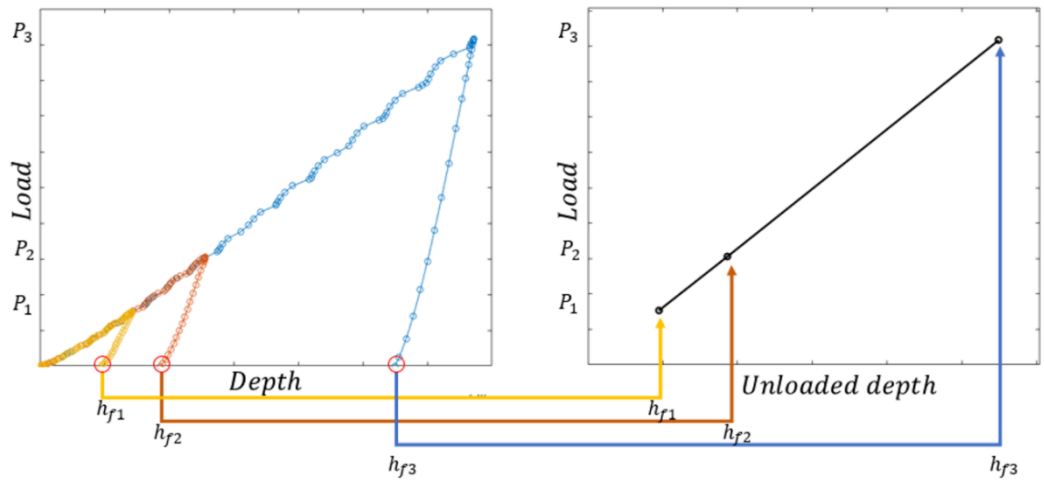

Figure 48. (a) Typical indentation loading-unloading curve and (b) adopted response for simulation.

The procedure adopted provides a curve of three points relating the applied load to the resultant indentation depth. The indentation depth can be calculated from Equation 68 or measured with a device having a profilometer function. Figure 48.b shows the example of an experimental indentation response adopted for simulation. Repeated FEM analysis is performed comparing the experimental indentation response to the predicted numerical output. The optimization algorithm is then responsible to minimize the discrepancy between them. The optimum hardening parameters are obtained when the step between iterations reaches a value lower than the tolerance value defined by MATLAB, which is $1e-8$ by default.

6.1.1 Parameter identification

As shown in the flowchart in Figure 38, the optimization procedure is a curve fitting process. Previously, it was presented the experimental reaction curve of a tensile test and the model (Equation 40) adopted to describe that curve. This model had four parameters, which were determined by an inverse optimization method applied to the data extracted from the uniaxial tensile test. The parameter identification process by means of the hardness test follows a similar optimization procedure, where the optimal parameters are determined when the stopping criterion is satisfied, which depends on the objective function.

As it was said in section 4.8, the objective function is a response of the discrepancy between the numerical and experimental indentation loading curves. The closer the objective function gets to zero, the more the provided stress-strain curve causes the numerical response to overlap the experimental data. Figure 49 shows the best fit between numerical and experimental indentation reaction curves provided in the optimization process using the load-final depth response of the indentation test.

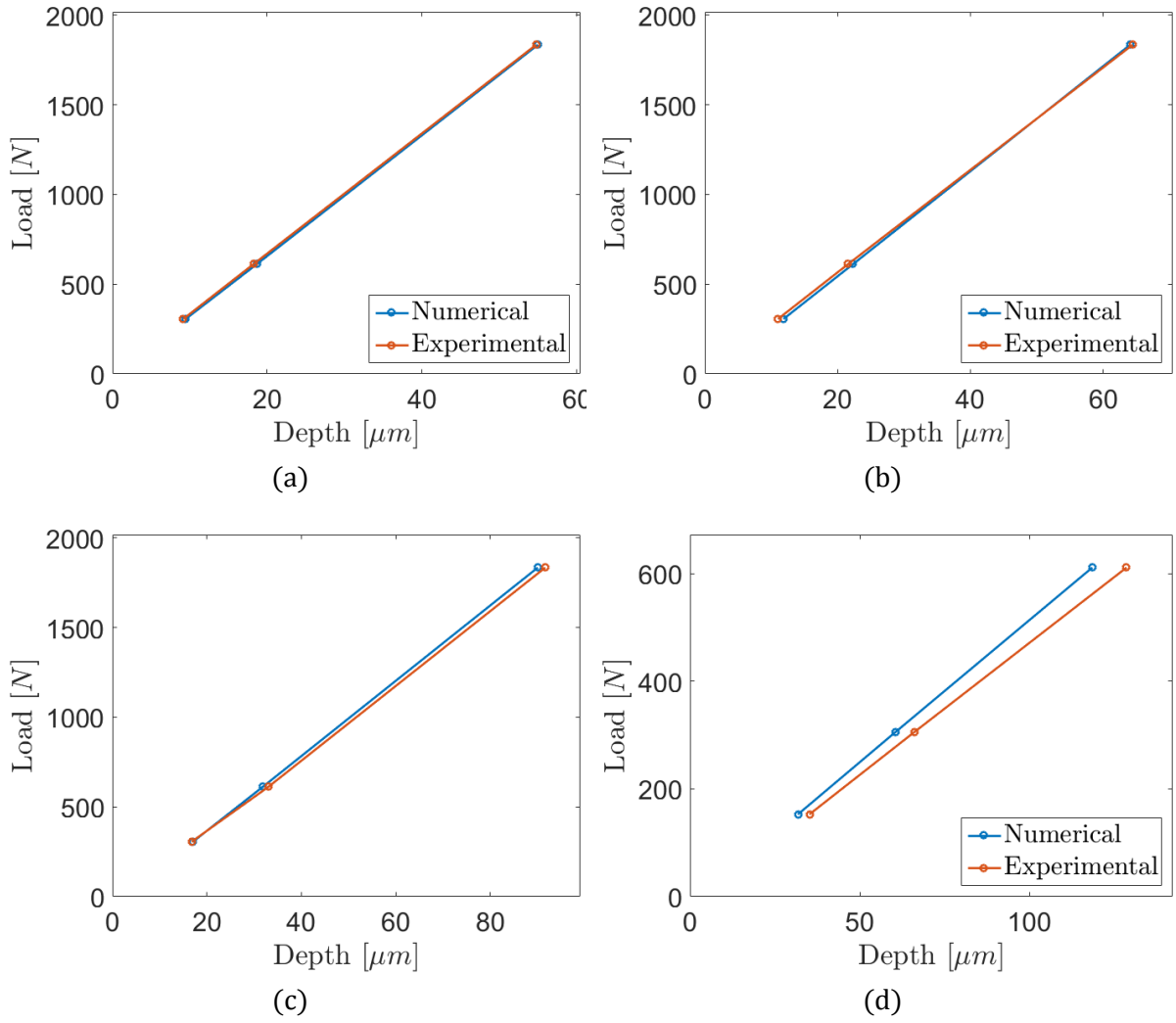

Figure 49. Reaction curves obtained numerically in comparison with experimental data for (a) SAE 1524, (b) SAE 4340 N, (c) SAE 4340 A, and (d) Aluminium 6101.

Figure 49 shows the result of the computational effort to match experimental and numerical data of indentation responses. The optimum hardening parameters determined in the optimization process are shown in Table 10 for each material under analysis.

Table 10. Material parameters obtained from the numerical inverse optimization process based on the indentation reaction curve.

Model	$\sigma_y(\bar{\varepsilon}^p) = \sigma_{y0} + \xi\varepsilon_p + (\sigma_\infty - \sigma_{y0})(1 - e^{-\delta\varepsilon_p})$				
Materials	σ_{y0} $[MPa]$	ξ [MPa]	σ_∞[MPa]	δ	$\bar{\varepsilon}^p_{max}$
SAE 1524	1079.1	100.5	1302.9	77.17	27.81 %
SAE 4340N	651.5	439.4	1268.5	47.57	25.66 %
SAE 4340 A	466.3	401.3	871.0	29.04	35.70 %
Al 6101	104.6	63.0	294.8	20.2	50.75 %

In order to evaluate the ability that the proposed method has to determine the material's hardening behavior, the parameters from Table 10 are used to generate the stress-strain relationship determined in the optimization process. These curves are then plotted (Figure 50) alongside with the respective stress-strain relationship determined by the uniaxial tensile test.

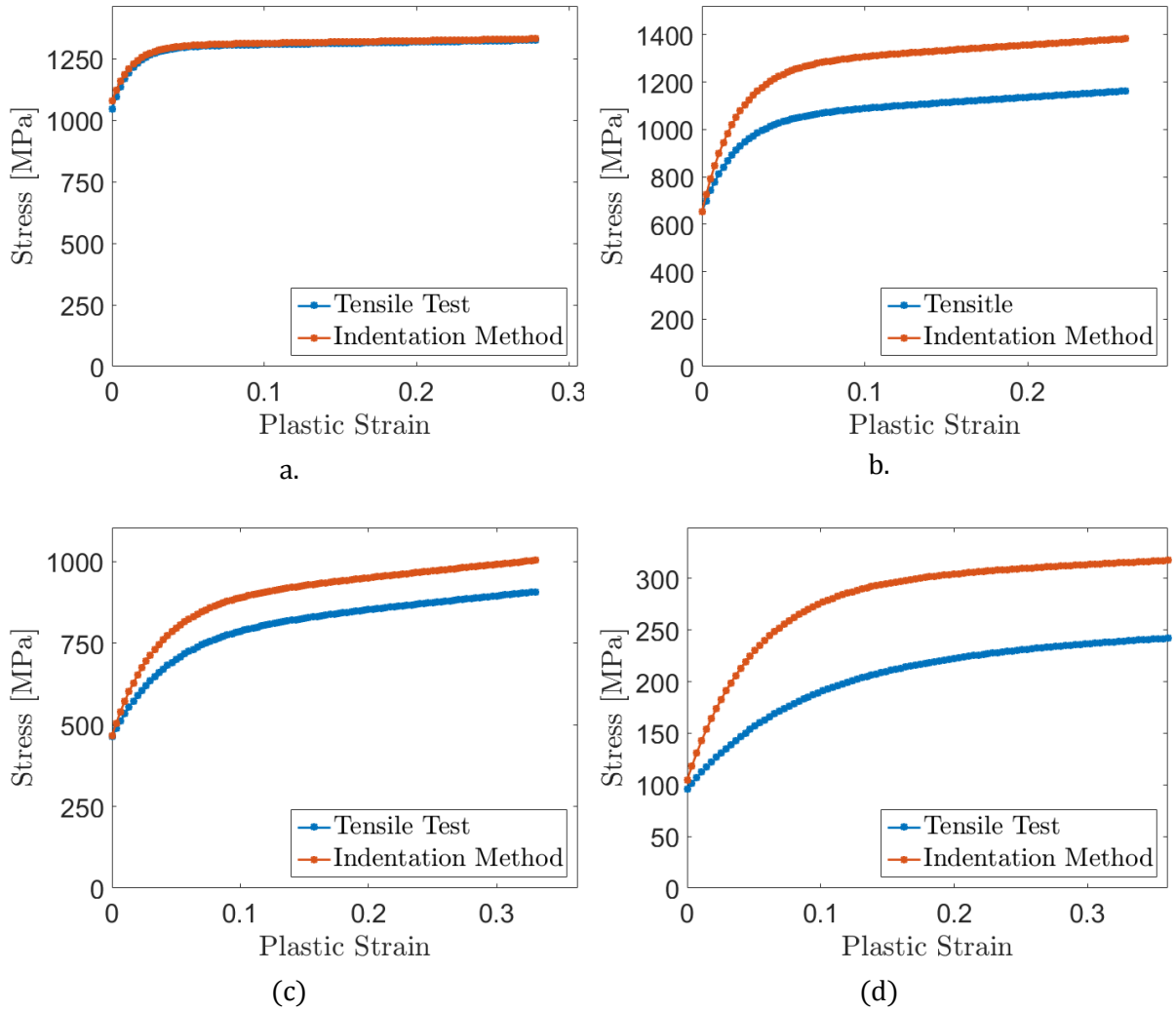

Figure 50: Comparison between hardening curves obtained from uniaxial tensile test and inverse method using the indentation reaction curve for (a) SAE 1524, (b) SAE 4340 N, (c) SAE 4340 A, and (d) Aluminium 6101.

Equation 69 is called to quantify the discrepancy between experimental and predicted hardening curves, bearing a difference of 0.56 % for the SAE 1524, 19.16 % for the SAE 4340 N, 11.74 % for the SAE 4340 A, and 37.15 % for the Aluminum 6101.

One of the interests in determining parameters to describe the material's hardening curve is in the possibility to predict the mechanical behavior of a specimen made of that material even when loaded in different configurations. Thus, another way to compare hardening curves obtained experimentally and numerically is by evaluating the predicted mechanical behavior of a specimen when submitted to

mechanical loadings encompassing plastic deformation. In the scope of an indentation hardness test, the hardening curves are used in the model and the resultant indentation profiles are extracted. These predicted indentation profiles are compared with the experimental ones from Figure 27. Table 11 lists the error in the prediction of indentation profiles from the stress-strain relationship obtained by the tensile test (TT) approach and by the indentation reaction curve (IRC) approach. The charts from Figure 51 to Figure 54 present the indentation profiles itself.

Table 11. Error in the prediction of indentation profiles from stress-strain relationship obtained by tensile test (TT) approach and by indentation reaction curve (IRC) approach.

Materials	Load 01		Load 02		Load 3	
	TT	IRC	TT	IRC	TT	IRC
SAE 1524	1.02%	1.04 %	2.24 %	1.25 %	4.93 %	4.88 %
SAE 4340 N	18.04 %	1.50 %	14.23 %	3.87 %	11.51 %	6.71 %
SAE 4340 A	4.45 %	4.32 %	6.94 %	4.20 %	6.94 %	1.63 %
Al 6101	8.54 %	7.14 %	10.61 %	10.11 %	10.14 %	9.12 %

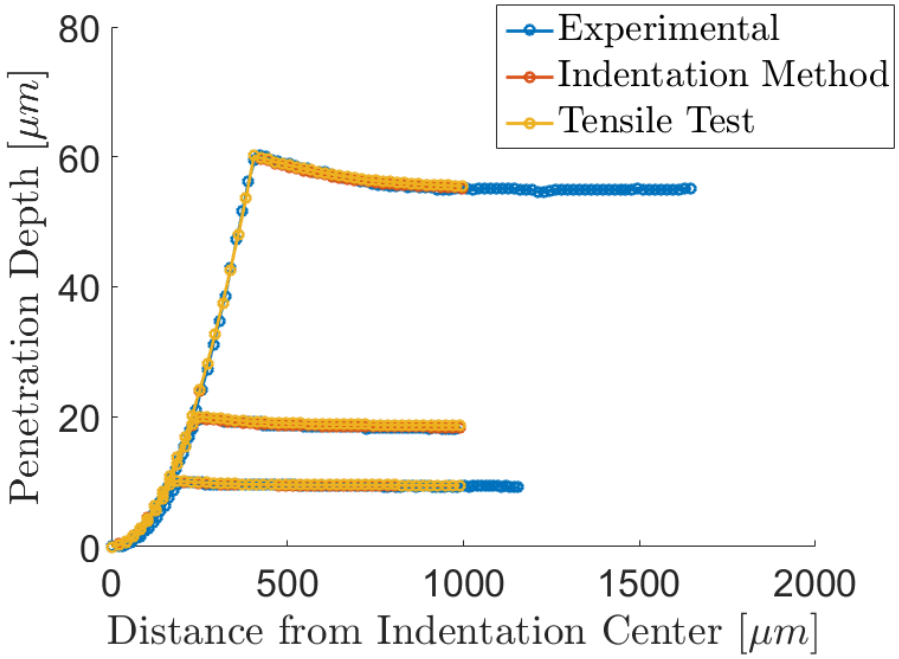

Figure 51. Predicted indentation profiles generated through the parameters generated from the tensile test (yellow), the indentation method (orange) in comparison with the experimental profiles (blue) for the SAE 1524.

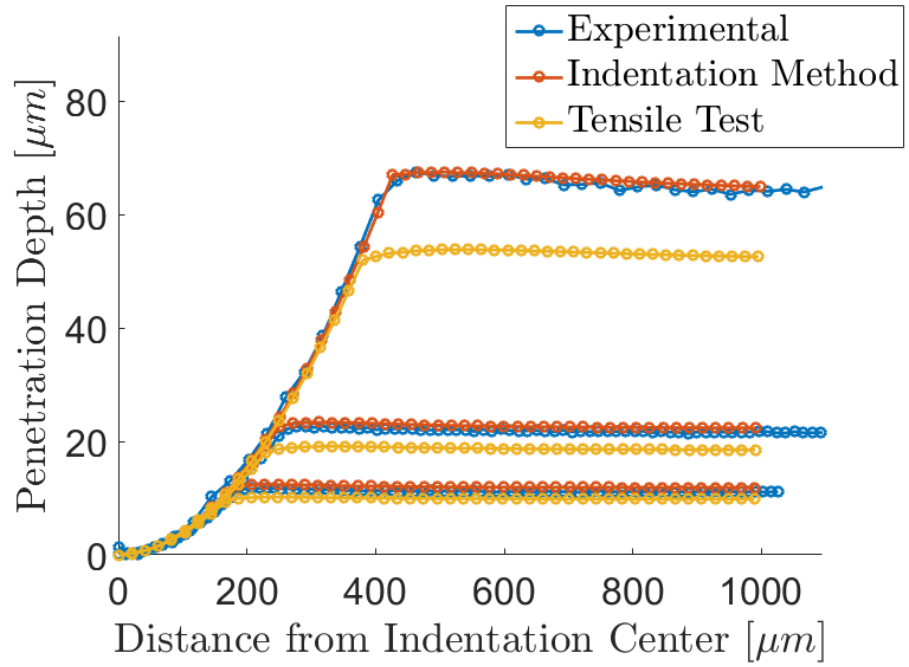

Figure 52. Predicted indentation profiles generated through the parameters generated from the tensile test (yellow), the indentation method (orange) in comparison with the experimental profiles (blue) for the SAE 4340 N.

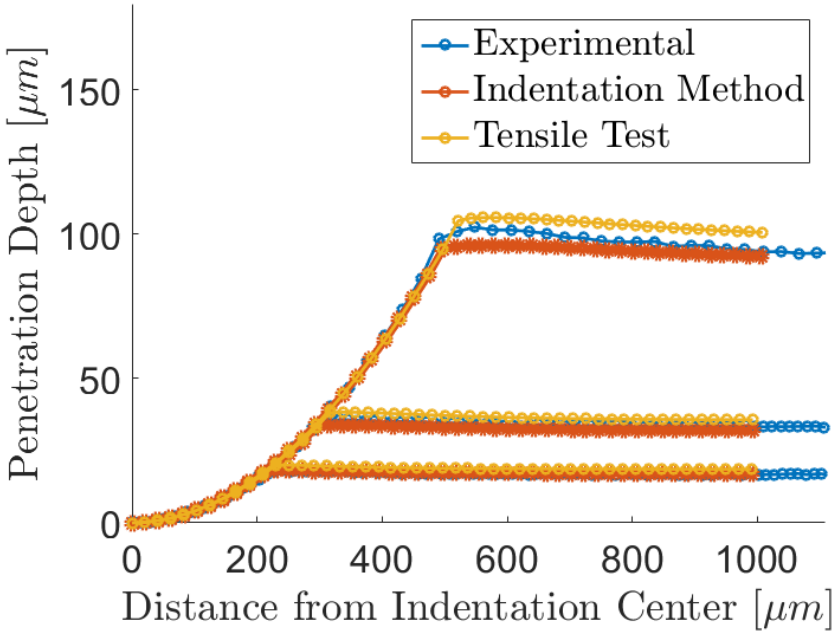

Figure 53. Predicted indentation profiles generated through the parameters generated from the tensile test (yellow), the indentation method (orange) in comparison with the experimental profiles (blue) for the SAE 4340 A.

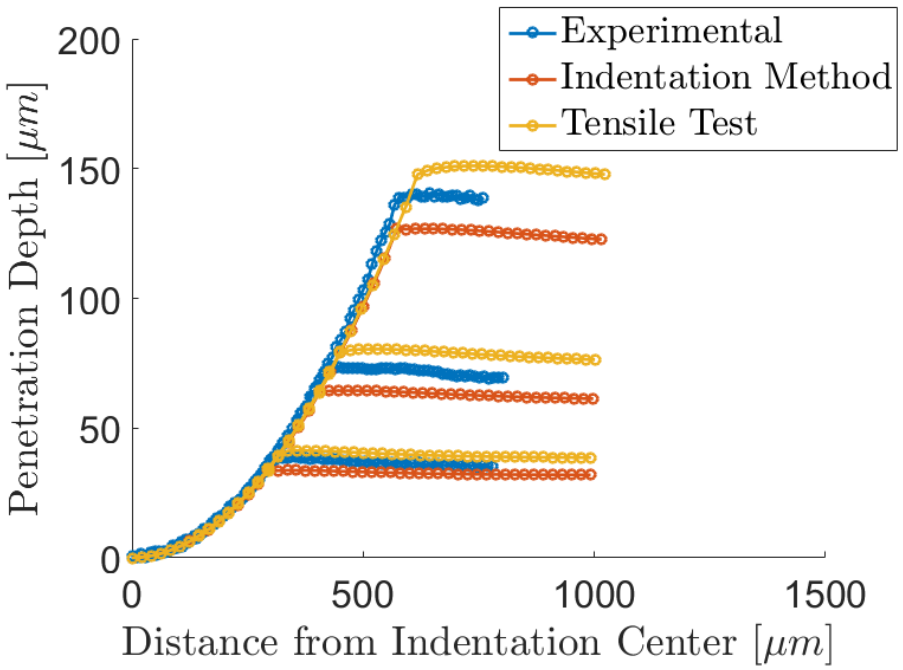

Figure 54. Predicted indentation profiles generated through the parameters generated from the tensile test (yellow), the indentation method (orange) in comparison with the experimental profiles (blue) for the Aluminum 6101.

6.2 Extraction of plasticity parameters from indentation profiles.

So far, the predicted indentation reaction curve has been used to determine the hardening parameters of some ductile materials as an alternative for the tension tests. For the cases where an instrumented indentation machine is not available, the trial methodology adopted to overcome this limitation consisted in correlating the maximum applied load to the final indentation depth of three Brinell Hardness tests performed in three different load configurations.

As the model was being developed and run, it was considered the possibility of the resulting output show some discrepancies in terms of its capability to predict the final impression mark left in the specimen due to the indentation test. The fact is that there may be different indentation profiles with the same final indentation depth. The problem was mainly based on the occurrence of material pile-up/sink. As can be seen in Figure 11, the pile-up/sink-in phenomena can lead to unprecise measurements of the indentation diameter and penetration depth. Besides that, the literature has reported that these phenomena are strongly influenced by the hardening exponent (Taljat and Pharr, 2004; Karthik *et al.*, 2012), which highly influences the shape of the hardening curve.

When measuring the indentation diameter from the Zwick Rowell Hardness Machine, it is not possible to take the pile-up effect into account because only the superior view is available. As consequence, every diameter measurement taken straight from the Zwick Rowell Hardness Machine induces inaccurate measurements of the indentation depth, since it is a function of the diameter.

The discrepancy in predicting the extent of pile-up/sink-in significantly influences the contact area and the indentation diameter. This is not surprising, since many material properties are strongly dependent on an accurate determination of the indentation contact area (Oliver and Pharr, 1992, 2004). For example, if pile-up is neglected for conical indenters, the true contact area may be underestimated up to 60 % (Bolshakov, A., & Pharr, 1998), which leads to the imprecise determination of material parameters.

Therefore, the establishment of a sound methodology for determination of material properties from load and depth indentation tests depends on accurately setting the true contact geometry. For this, pile-up/sink-in effects must be considered. This is achieved by replacing the final indentation depth as the target indentation response by the indentation profile itself, as shown in Figure 55.

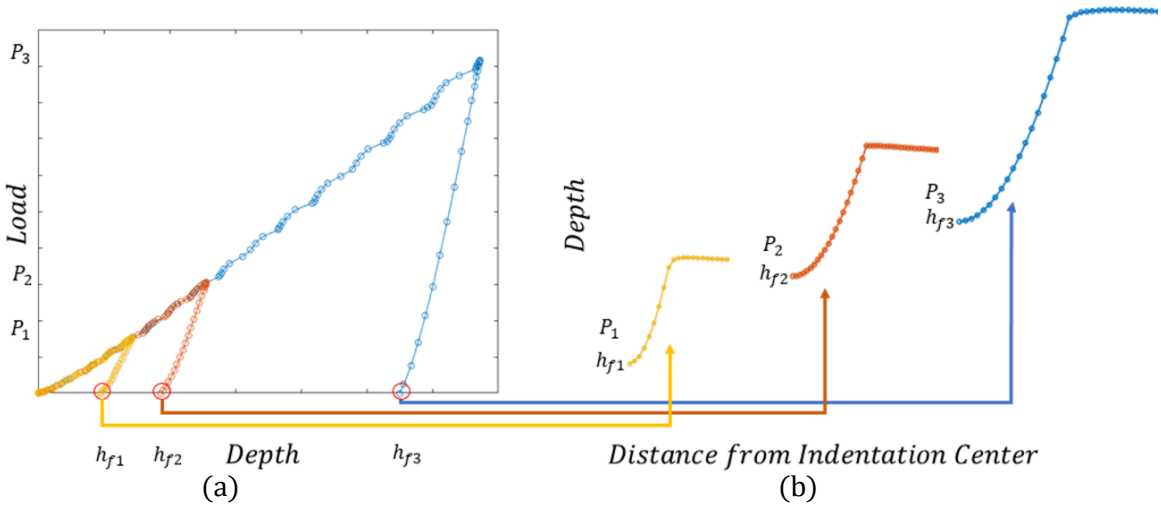

Figure 55. (a) Typical indentation loading-unloading curve and (b) adopted response for simulation.

6.2.1 Parameter identification

Again, numerical and experimental indentation responses are compared in a computational effort to extract the material hardening parameters. At this time, the indentation profiles extracted from three configurations of the Brinell hardness test (Figure 27) are used as the target information. Repeated FEM modeling is performed until the generated hardening parameters provide the best fitting between numerical and experimental indentation profiles. The best fit provided in the process is shown from Figure 56 to Figure 59 alongside with the predicted indentation profile generated using the stress-strain relationship obtained from the tensile test.

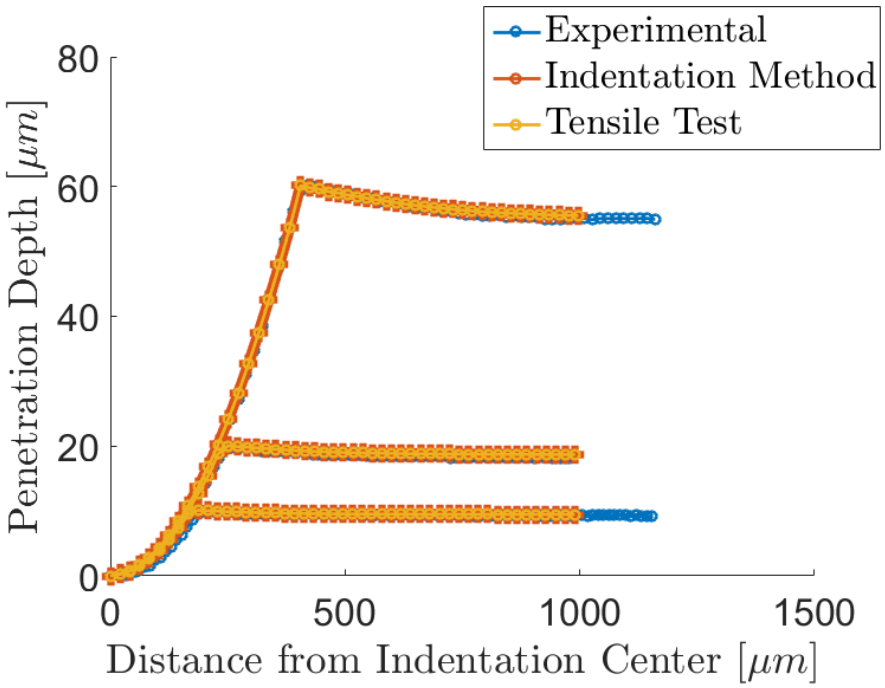

Figure 56. Predicted indentation profiles generated through the parameters generated from the tensile test (yellow), the indentation method (orange) in comparison with the experimental profiles (blue) for the SAE 1524.

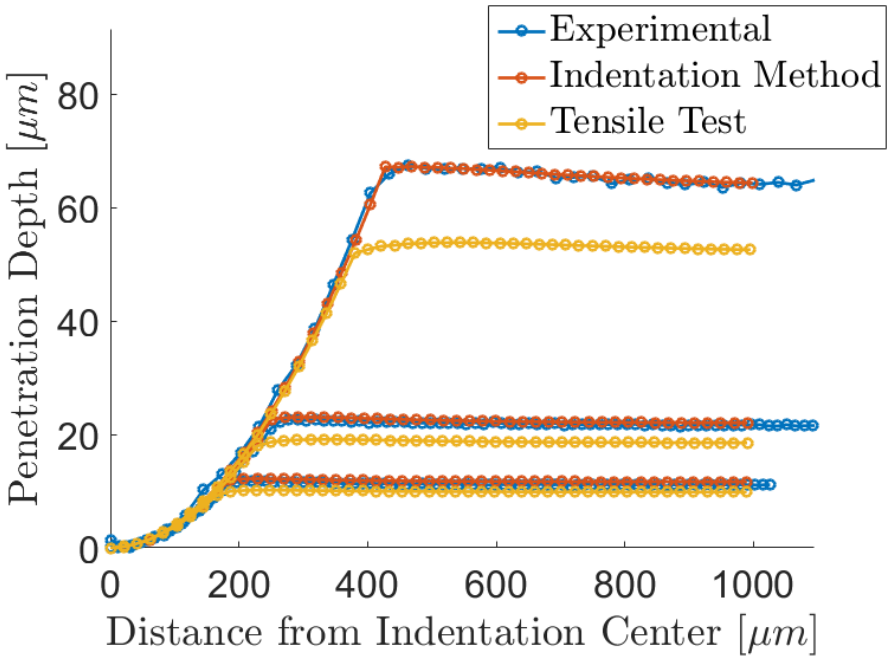

Figure 57. Predicted indentation profiles generated through the parameters generated from the tensile test (yellow), the indentation method (orange) in comparison with the experimental profiles (blue) for the SAE 4340 N.

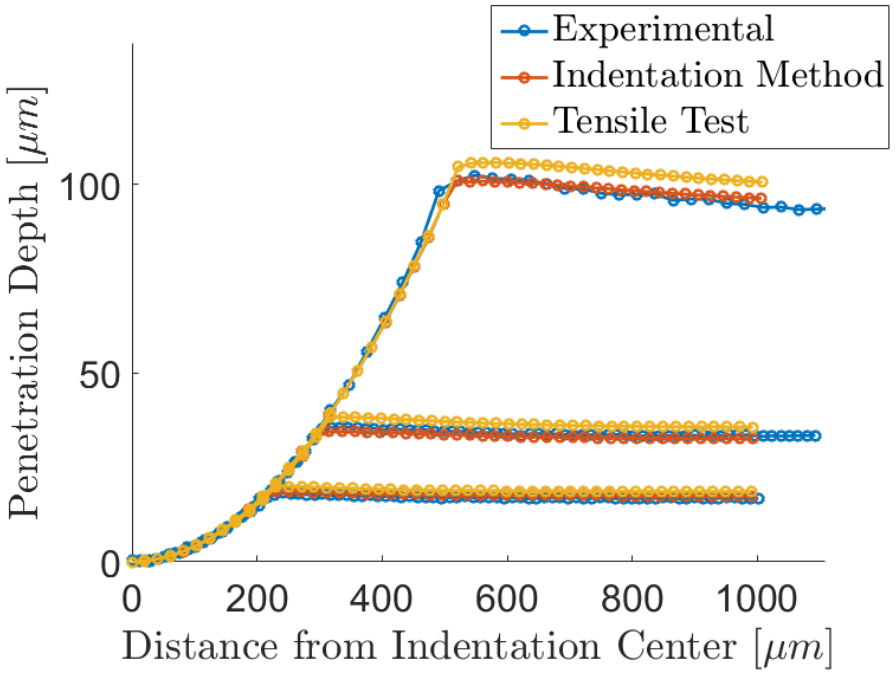

Figure 58. Predicted indentation profiles generated through the parameters generated from the tensile test (yellow), the indentation method (orange) in comparison with the experimental profiles (blue) for the SAE 4340 A.

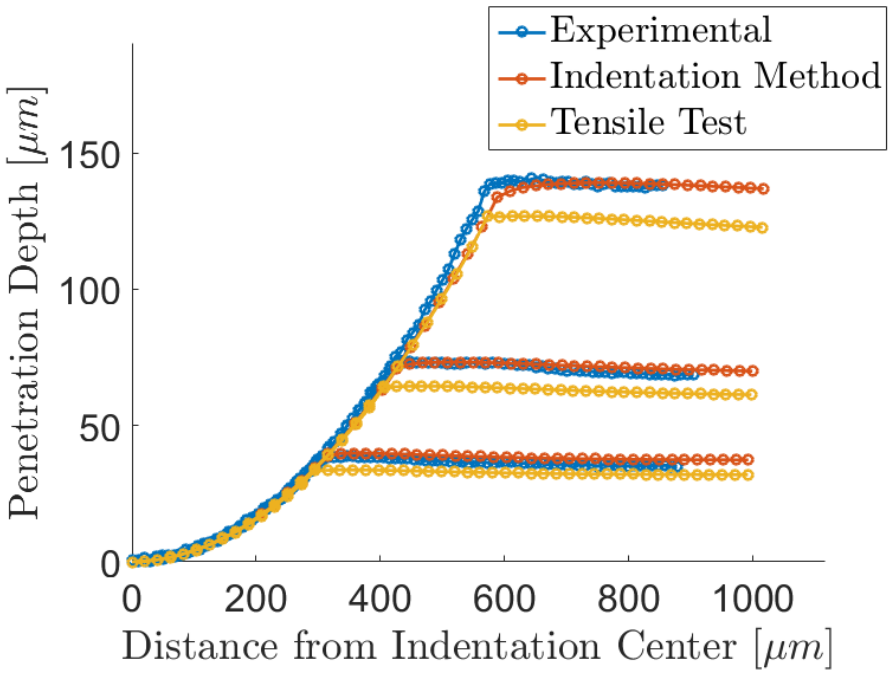

Figure 59. Predicted indentation profiles generated through the parameters generated from the tensile test (yellow), the indentation method (orange) in comparison with the experimental profiles (blue) for the Aluminum 6101.

To compare the quality of the numerical data, Table 11 lists the error in the prediction of indentation profiles from the stress-strain relationship obtained by the tensile test (TT) approach and by the indentation profile (IP) approach.

Table 12. Error in the prediction of indentation profiles from stress-strain relationship obtained by tensile test (TT) approach and by indentation profile (IP) approach.

Materials	Load 01		Load 02		Load 3	
	TT	IP	TT	IP	TT	IP
SAE 1524	1.02 %	1.05%	2.24 %	2.26 %	4.93 %	4.93 %
SAE 4340 N	18.04 %	1.37 %	14.23 %	2.57 %	11.51 %	4.86 %
SAE 4340 A	10.31 %	1.73 %	5.07 %	2.44 %	6.94 %	3.75 %
Al 6101	8.54 %	3.82 %	10.61 %	2.89 %	10.14 %	5.24 %

From the set of hardening parameters determined, stress-strain curves are generated (Figure 60). according to the Kleinermann-Ponthot hardening model (Equation 40).

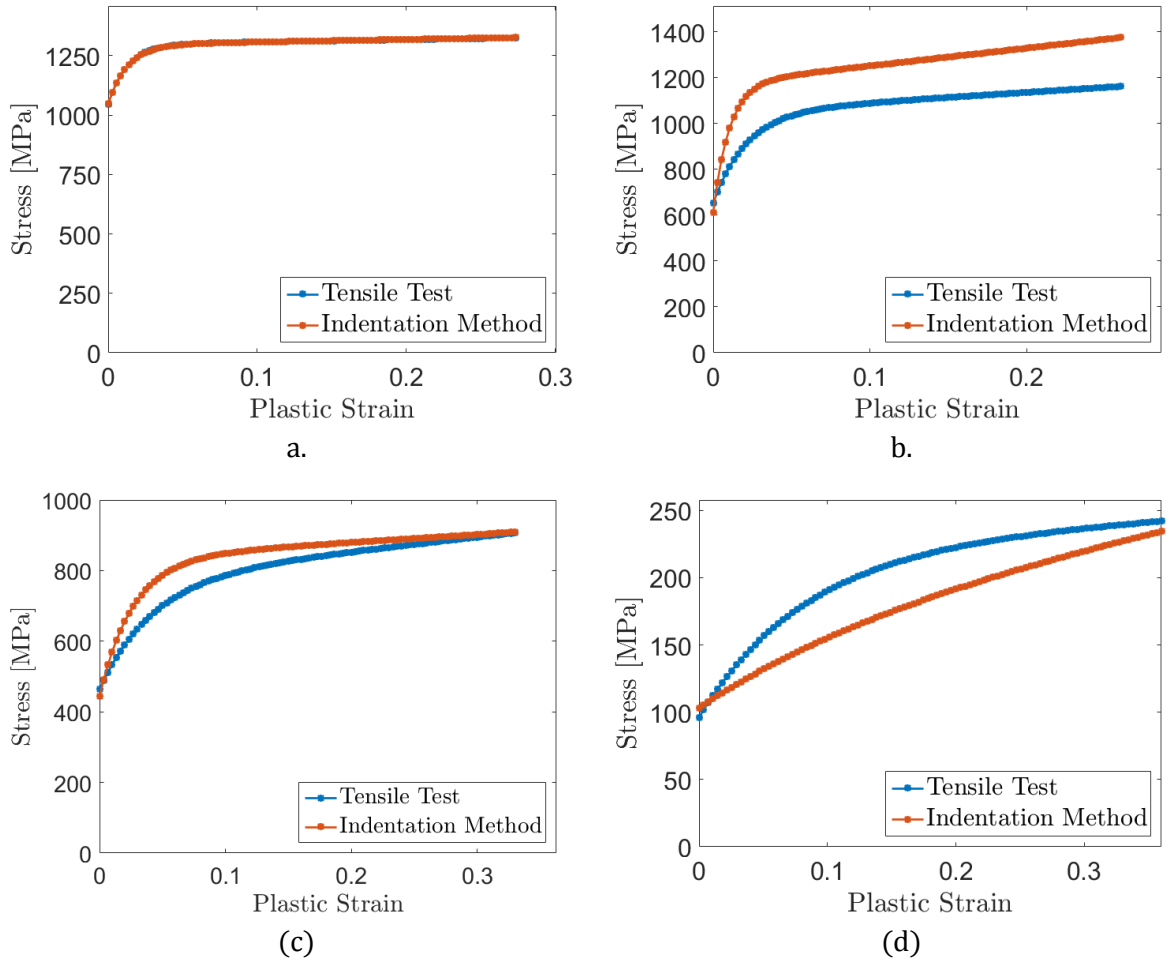

Figure 60. Comparison between hardening curves obtained from uniaxial tensile test and inverse method using the indentation profile for (a) SAE 1524, (b) SAE 4340 N, (c) SAE 4340 A, and (d) Aluminium 6101.

The ability of the method to generate the material hardening curve is evaluated by plotting the hardening curves provided by the indentation method and by the tensile test for each material assessed. Equation 69 is used to give the relative difference between both stress-strain curves shown for each material in Figure 60. The difference is nearly zero for the SAE 1524, 16.82 % for the SAE 4340 N, 5.84 % for the SAE 4340 A, and 12.61 % for the Aluminum 6101. The optimum hardening parameters determined through this approach in the optimization process are shown in Table 13 for each material under analysis.

Table 13. Material parameters obtained from the numerical inverse optimization process based on the indentation reaction curve.

$Model$	$\sigma_y(\bar{\varepsilon}^p) = \sigma_{y0} + \xi\varepsilon_p + (\sigma_\infty - \sigma_{y0})(1 - e^{-\delta\varepsilon_p})$				
Materials	σ_{y0} $[MPa]$	ξ [MPa]	σ_∞[MPa]	δ	$\bar{\varepsilon}^p_{max}$
SAE 1524	1048.6	111.2	1296.0	76.90	27.33 %
SAE 4340N	612.4	776.0	1173.5	97.58	26.69 %
SAE 4340 A	444.6	226.8	834.4	37.78	32.93 %
Al 6101	103.2	191.9	172.0	6.46	36.82 %

6.3 Comparative Analysis

From far, the best results were given for the SAE 1524. Both IRC and IP approach produced stress-strain curves that fitted the stress-strain curve obtained from the uniaxial tensile test. It is important to note that all these three stress-strain curves, obtained from different methods, yielded similar numerical indentation responses when inserted in the FEM model. Furthermore, all of them matched the experimental data. For the SAE 4340 N, both hardening curves obtained from IRC and IP approaches presented similar behavior. However, when compared to the hardening curve obtained from the uniaxial tensile test, the discrepancy between them was about 19.2 % and 16.8 % respectively to IRC and IP approaches. It is also important to note that the hardening curve obtained by means of the uniaxial tensile test was not able to predict neither the load-final depth relationship of the material nor the shape of the indentation profile. Since the optimization is done based on these aspects, it is reasonable to expect a different hardening curve if the IRC or the IP methods are applied.

For the SAE 4340 A, the hardening curves given by IRC and IP approaches overlap each other up to 4 % of plastic deformation. Beyond this point, they start to diverge. The curve generated by the IRC approach keeps parallel to the hardening curve obtained from the tensile test while the hardening curve generated by the IP approach goes toward it. Some of the same aspects listed for the SAE 4340 N can be repeated to the SAE 4340 A. First, the stress-strain curve obtained from the uniaxial tensile test was unable to predict the experimental indentation responses. Second, an interesting behavior is seen when using the parameters given by the IRC approach. Even though it was able to generate a stress-strain

curve that fitted the load-final depth response, it was not able to predict the indentation profile with high accuracy. In fact, it predicted a profile with the same final depth but with a lower amount of pile-up. This occurrence corroborates with the assumption made in section 6.2 that there are different indentation profiles with the same final indentation depth. Thus, considering pile-up/sink-in phenomena in the parameter identification task is vital to obtain realistic plasticity parameters.

Still for the SAE 4340 A, the IP approach provided a stress-strain curve with about 5.8 % of discrepancy toward the stress-strain curve obtained from the uniaxial tensile test. Again, this is acceptable since the hardening curve obtained from the uniaxial test was unable to predict the experimental indentation profile. This circumstance calls the hypothesis that the material behaves differently under tension and compression. Since the uniaxial test was performed under tension and the indentation is by nature compressive, two different hardening curves are to be extracted from these two approaches if the material is not isotropic. Therefore, a uniaxial reaction data from a compressive test would be more appropriate to evaluate the methodology for non-isotropic materials.

The greater limitations happened for the Aluminum 6101. The IRC approach was not able to match the experimental load-final depth response of the material and therefore was not able to predict a realistic hardening curve for the Aluminum 6101. On the other hand, the IP approach overcame the IRC limitation and generated a hardening curve able to fit the experimental data with a discrepancy around 5.24 % for the worst case (Figure 59 and Table 12). However, when comparing the hardening curves from the uniaxial tensile test and from the IP approach, they do not match each other. Once more, they did not match for the same reason presented for the SAE 4340: the indentation responses given when the stress-strain curve obtained from the uniaxial test is used in the model is not equivalent to the experimental data. For this reason, the same assumption made there is repeated here, which is that the aluminum does not have an isotropic behavior.

CONCLUSION

The plasticity parameters of four metallic materials were determined by indentation tests and FEM analyses. For this, two approaches were established based on the traditional Brinell indentation hardness tests. This test provided the experimental data to be used as the target curve for the FEM output. All the process was conducted by an optimization algorithm that was employed by a parameter identification routine.

Thinking of making possible the use of this technique by other researchers, a user-friendly interface was also developed in C#. Through that, the user informs the experimental indentation data, the load applied and the indenter radius. Besides the Kleinermann-Ponthot model, the Ludwick constitutive model is also made available. Throughout the process, the user is kept updated of the new parameters suggested while a new plot is generated at each iteration. A tutorial on how to use the user interface is made available in Appendix A.

The first aspect considered in this work was the dependence of the method on repetitive FEM analysis. Therefore, the primary objective was to build a numerical model with two main features: reliability and efficiency. For this, a fast running method that provides realistic predictions was built. This included understanding the effect of friction, contact formulation and meshing. The second goal was to adopt an optimization algorithm and communicate it with the FE model. This was reached by developing an optimization routine in MATLAB and the use of the built-in optimization toolbox through the function *nlinfit*. With these steps done and experimental data acquired, the method was ready to run.

Two techniques for extraction of plasticity parameters of metals were addressed, both are novelties presented here. The first uses the indentation load-final depth response while the second uses the indentation profile as the comparable data in the optimization process. Once the plasticity parameters were determined, they were used to generate the hardening curves. In order to evaluate the capability of the method in providing the material stress-strain relationship, uniaxial tensile tests were performed alongside with indentation tests. Since it is the traditional way to extract material hardening parameters, it works as a good standard to be compared with. Therefore, uniaxial tensile tests were conducted for each material assessed.

As discussed in the conclusion of the last chapter, in section 6.3, the hardening curves generated from the optimum plasticity parameters determined did not match well the ones obtained from the uniaxial tensile for most cases. With exception of the SAE 1524, the hardening curves for the SAE 4340 N, 4340 A, and Aluminum 6101 presented a considerable discrepancy when compared with ones obtained from the tensile test, going up to 37 % for the Aluminum. The fact is that the hardening curves obtained from the uniaxial test for these materials were not able to predict the experimental indentation

response. Since IRC and IP approaches are based on the fitting process of indentation responses, it was expected to that both curves did not match. The hypothesis adopted is that these materials cannot be considered isotropic, i.e., they present distinct behavior under tension and compression.

The different behaviors observed for the materials analyzed, especially for those that presented a distinct response under compression and tension, agrees with the necessity to establish a sound methodology for extraction of plasticity parameters by means of indentation tests. Even if the stress-strain curve obtained from compressive uniaxial tests were available, the indentation technique offers much more by being able to assess local quantities and, therefore, small amounts of materials. Especially the simulation of contact problems such as those present in assembled mechanical structures could benefit from this technique. If this becomes possible, even surface treatment, welds, heated affected zone, and coatings could be assessed and considered for simulation with plasticity included.

The main limitation of the model is in the optimization algorithm regarding its high dependence of the initial guess and the occurrence of local minimums. If an instrumented indentation device is available, the initial guess could be estimated from the concept of the representative stress. As this work shows, the use of this method to establish the hardening parameters still brings many uncertainties. However, its use as an initial estimation of the hardening parameters may come at hand to give a hint of the shape of the hardening curve. But in order to withdraw these limitations from the method, the best approach would be to develop an optimization routine using an unconstrained nonlinear optimization method independent of initial estimations, such as the Broyden–Fletcher–Goldfarb–Shanno (BFGS) algorithm.

APPENDIX A. USER-FRIENDLY INTERFACE

A user-friendly interface was built in C# to facilitate the use of the methodology developed in this work. It is an .exe application, so it can only be installed in windows running machines. In order to use this program, the user must extract profiles generated by ball indentations with the use of a profilometer. The user must also know the configuration of each indentation test, i.e. the load applied, and the indenter radius. Figure 61 shows the user interface.

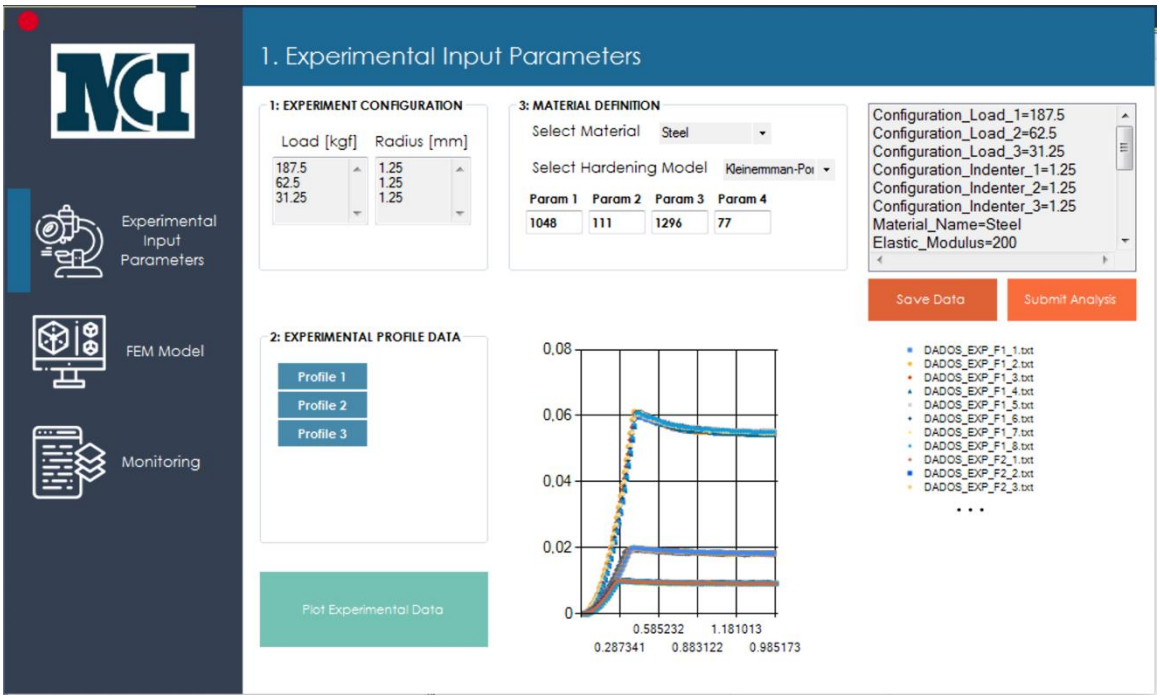

Figure 61. User interface.

As can be seen, the first panel of the user interface prompts the user for the experimental input parameters and has three fields to be filled in. The first requests the experiment configuration. Here, the user must insert the load and the indenter radius for each configuration of the indentation test conducted, as shown in Figure 62.

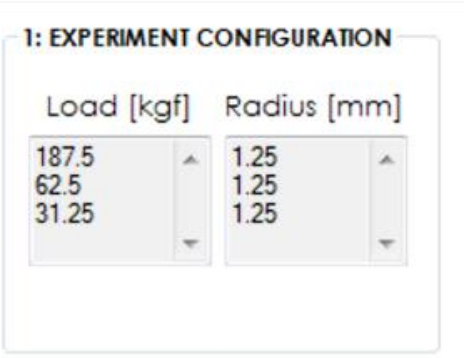

Figure 62. Experiment configuration input.

The second field requests the experiment indentation profiles. In Figure 63, the user selected profiles and pushed the 'Plot Experimental Data' button. Immediately, the profiles are plot as shown in the chart. Two important aspects: first, this information must be available in.txt the with the coordinates in mm. Second, the minimum value of the indentation valley must also be set to zero as shown in the chart of Figure 63.

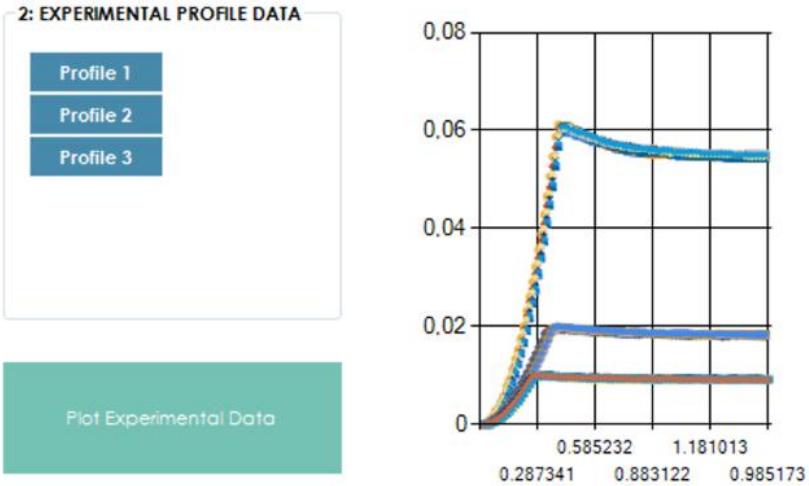

Figure 63. Experimental profile data input.

For each configuration load, the multi-profile selection is available. It means that if more than one indentation is performed for the same experiment configuration, all the measured profiles can be used during the process. Figure 64 illustrates the case where the button 'Profile 1' was selected. A window pops-up and the user selects all the profiles measured for that configuration.

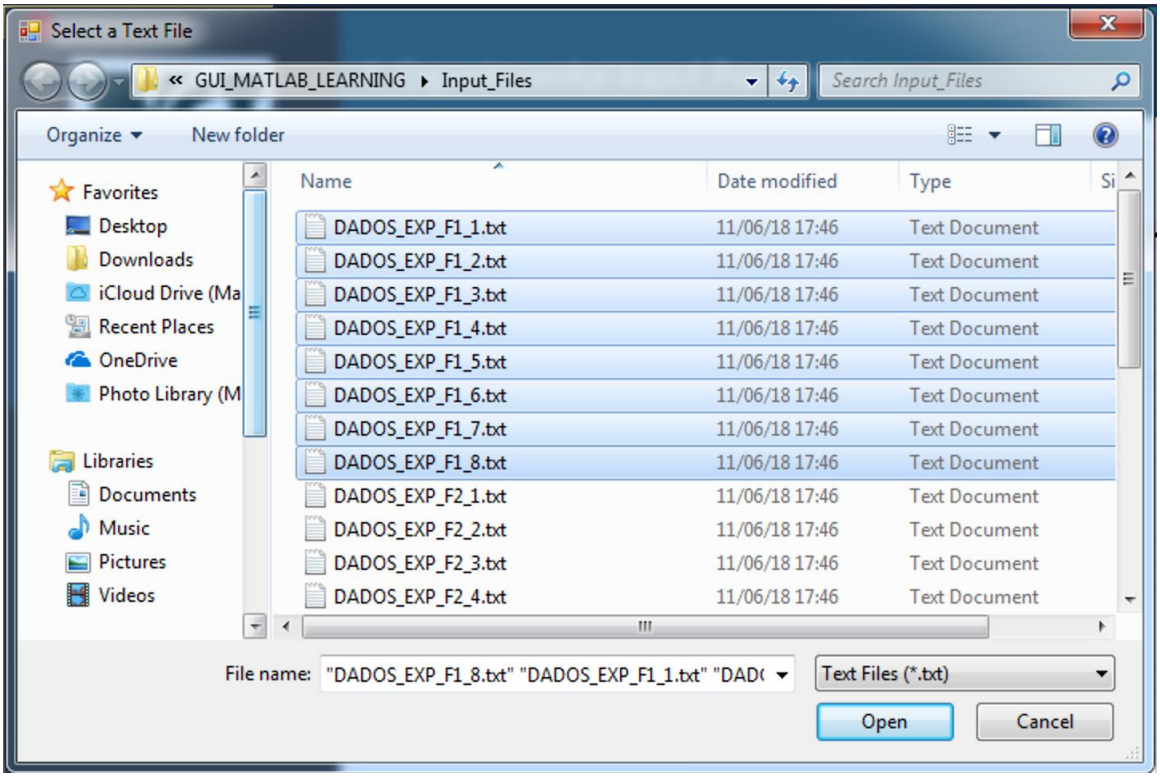

Figure 64. Selecting text files with the coordinates of the measured indentation profiles.

The last step is to fill in the blanks in the material definition field. As shown in Figure 65, three actions are required: the selection of the material, the selection of the plasticity model, and the initial guesses for the parameter identification process.

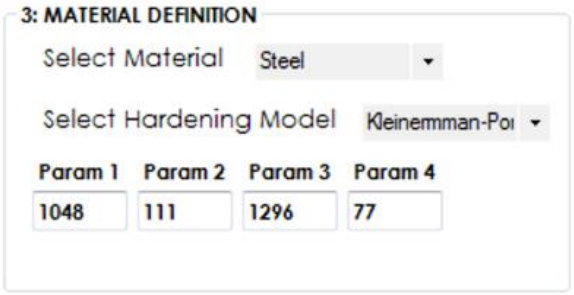

Figure 65. Material definition input.

Besides the Kleinermann-Ponthot constitutive model, the Ludwick model is also made available, which has three parameters. If this is selected the appropriate number of fields is shown.

Up to this point, all the information to perform the analysis has been given. Therefore, the user is ready to save that information by pressing the button ‘Save Data’. When this is done, all the information is saved in a .txt file and showed for the user, as listed in Figure 66. The last step is to press the Submit Analysis’ button.

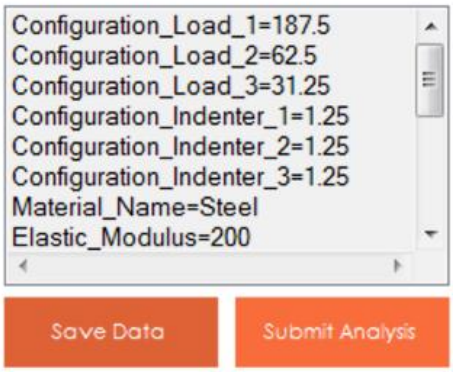

Figure 66. Save data and submit analysis buttons.

From now on, the user is kept updated through the 'Monitoring' window, which shows the development of the indentation. Furthermore, a windows pops-up at each iteration showing predicted and target curves.

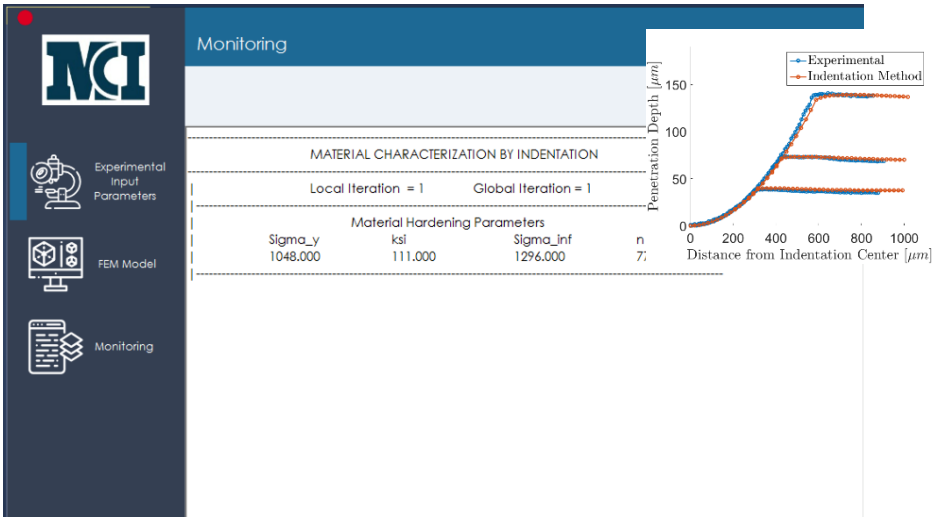

Figure 67. Monitoring window

All the data generated by the simulation is saved in the directory where the program was installed.

APPENDIX B. OPTIMIZATION ROUTINE

```
Clear

clc

close all
% Global Variables
global Iter Evals History nop nob
global sigma_y ksi sigma_inf delta scale
format longE
% Estimativa Iniciais
Estimativa_Inicial = [INSERT_PARAM1 INSERT_PARAM2 INSERT_PARAM3 INSERT_PARAM4];

scale = 1e-4*[10^(-floor(log10(abs(Estimativa_Inicial(1,1))))) ...
              10^(-floor(log10(abs(Estimativa_Inicial(1,2))))) ...
              10^(-floor(log10(abs(Estimativa_Inicial(1,3))))) ...
              10^(-floor(log10(abs(Estimativa_Inicial(1,4)))))];

sigma_y = Estimativa_Inicial(1,1);
ksi = Estimativa_Inicial(1,2);
sigma_inf = Estimativa_Inicial(1,3);
delta = Estimativa_Inicial(1,4);
% Parameters
nop = 4;

Initial_Paramenter = Estimativa_Inicial .* scale;
% Initializing
Iter = 0;
Evals = 0;
History = [];
Set_options = optimset('TolFun', 1e-12, 'TolX', 1e-12, 'MaxIter', 10000);

% Invoke Optimizer
lb = [];
up = [];

% lb = [].*scale;
% up = [].*scale;
% [x, resnorm] = lsqnonlin(@optimization_lsqnonlin, Initial_Paramenter, lb, up,
Set_options);
options = optimoptions('lsqnonlin','Display','iter');
[x,resnorm,residual,exitflag,output] =
lsqnonlin(@optimization_lsqnonlin_KLEIRNERMANN, Initial_Paramenter, lb, up,
options);
x1 = x(1)/scale(1);

x2 = x(2)/scale(2);

x3 = x(3)/scale(3);
```

```
x4 = x(4)/scale(4);

OptParam = [x1 x2 x3 x4];

parameter = fopen('parameter.txt', 'w');
fprintf(parameter, '%12.8f\t%12.8f\t%12.8f\t%12.8f', OptParam);
fclose(parameter);
% Strain data
XX = fopen('DEFORMACAO.txt', 'r');
XDATA = fscanf(XX, '%f');
fclose(XX);

% Generate hardening curve
YY = x1 + x2.*XDATA + (x3 - x1)*(1 - exp(-x4.*XDATA));

% Write hardening curve to txt
pID=fopen('Material_Hardening_Curve.txt','w+');
for jj = 1:length(XDATA)
    fprintf(pID,'%14.10f\t%14.10f\t\n', YY(jj), XDATA(jj));
end
fclose(pID);
disp('Material_Hardening_Curve.txt gerada com sucesso')
% Save the parameter evolution History in 'Parameter_history.txt'
History = [History; [Iter Evals x1 x2 x3 x4 resnorm]];
Parameter_history = fopen('Parameter_history.txt', 'w');
fprintf(Parameter_history,
'%12.8f\t%12.8f\t%12.8f\t%12.8f\t%12.8f\t%12.8f\t%12.8f\n', History);
fclose(Parameter_history);
% Run Abaqus
mo='noGUI';
% mo='script';

% unix(['abaqus cae ',mo,'=Main.py']);   %Unix system
system(['abaqus cae ',mo,'=Brinell_Hardness_Test_F1.py']); %Windows system?

disp('Brinell_Hardness_Test_F1.py executado')
```

Published with MATLAB® R2015b

REFERENCES

ABAQUS/Standard User's Manual (6.14) (2014) '36.5.1 Defining contact pairs', pp. 1–11. Available at: http://abaqus.software.polimi.it/v6.14/books/usb/default.htm?startat=pt09ch36s05aus160.html#usb-cni-aexpcontactpair.

Ahn, J. H. and Kwon, D. (2001) 'Derivation of plastic stress-strain relationship from ball indentations: Examination of strain definition and pileup effect', Journal of Materials Research, 16(11), pp. 3170–3178. doi: 10.1557/JMR.2001.0437.

ASM International (2004) 'Introduction to Tensile Testing', Tensile testing, pp. 1–13. doi: 10.1017/CBO9781107415324.004.

ASTM Int. (2009) 'Standard Test Methods for Tension Testing of Metallic Materials 1', Astm, (C), pp. 1–27. doi: 10.1520/E0008.

ASTM Int. (2012) 'Standard Test Method for Brinell Hardness of Metallic Materials', Astm, pp. 1–32. doi: 10.1520/E0010-12.2.

Bobzin, K. et al. (2013) 'Approach to determine stress strain curves by FEM supported nanoindentation', Materialwissenschaft und Werkstofftechnik, 44(6), pp. 571–576. doi: 10.1002/mawe.201300099.

Bolshakov, A., & Pharr, G. (1998) 'Influences of pileup on the measurement of mechanical properties by load and depth sensing indentation techniques', Journal of Materials Research, pp. 1049–1058. doi: 10.1557/JMR.1998.0146.

Bucaille, J. L. et al. (2003) 'Determination of plastic properties of metals by instrumented indentation using different sharp indenters', Acta Materialia, 51(6), pp. 1663–1678. doi: 10.1016/S1359-6454(02)00568-2.

Chandler, H. (1999) 'Introduction to Hardness Testing', Hardness Testing, p. 14. doi: 10.1126/scisignal.2001965.

Chaudhri, M. M. (1996) 'Subsurface plastic strain distribution around spherical indentations in metals', Philosophical Magazine A. Taylor & Francis, 74(5), pp. 1213–1224. doi: 10.1080/01418619608239721.

Conn, Andrew R.; Gould, Nicholas I. M.; Toint, P. L. (2000) Trust-Region Methods. Philadelphia, PA.

Dean, J. and Clyne, T. W. (2017) ‘Extraction of plasticity parameters from a single test using a spherical indenter and FEM modelling’, Mechanics of Materials. Elsevier Ltd, 105, pp. 112–122. doi: 10.1016/j.mechmat.2016.11.014.

Dowling, N. E. (2013) Mechanical Behavior of Materials. Fourth Edi. Pearson Education Limited.

Fu, K. et al. (2015) ‘On the determination of representative stress-strain relation of metallic materials using instrumented indentation’, Materials and Design. Elsevier Ltd, 65, pp. 989–994. doi: 10.1016/j.matdes.2014.10.018.

Gao, X. et al. (2010) ‘On stress-state dependent plasticity modeling : Significance of the hydrostatic stress , the third invariant of stress deviator and the non-associated flow rule’. doi: 10.1016/j.ijplas.2010.05.004.

Giannakopoulos, A. E. and Suresh, S. (1999) ‘Determination of elastoplastic properties by instrumented sharp indentation’, Scripta Materialia, 40(10), pp. 1191–1198. doi: 10.1016/S1359-6462(99)00011-1.

Guillonneau, G. et al. (2012) ‘Determination of mechanical properties by nanoindentation independently of indentation depth measurement’, Journal of Materials Research, 27(19), pp. 2551–2560. doi: 10.1557/jmr.2012.261.

Hertz, H. (1881) ‘Ueber die Berührung fester elastischer Körper’, Journal fur die Reine und Angewandte Mathematik, (92), pp. 156–171. doi: 10.1515/crll.1882.92.156.

Hill, R., Storakers, B. and Zdunek, A. B. (1989) ‘A Theoretical Study of the Brinell Hardness Test’, Proceedings of the Royal Society A: Mathematical, Physical and Engineering Sciences, 423(1865), pp. 301–330. doi: 10.1098/rspa.1989.0056.

Hills, D. A. (1983) ‘Some aspects of post-yield contact problems’, Wear, 85(1), pp. 107–119. doi: 10.1016/0043-1648(83)90339-3.

Hills, D. A., Nowell, D. and Sackfield, A. (1993) ‘Contact of layered bodies’, in Mechanics of Elastic Contacts. Elsevier, pp. 349–391. doi: 10.1016/B978-0-7506-0540-3.50016-7.

Hollomon, J. H. (1945) ‘Tensile deformation’, AIME Trans, pp. 1–22.

Hosford, W. F. (2013) ‘Fundamentals of Engineering Plasticity’, p. 278. doi: 10.1016/0020-7403(63)90046-8.

Huber, M. T. (1904) ‘Zur Theorie der Berührung fester elastischer Körper’, Annalen der Physik, 319(6), pp. 153–163. doi: 10.1002/andp.19043190611.

ISO (2008) NPR-TR 29381 Metallic materials - Measurement of mechanical properties by an instrumented indentation test - Indentation tensile properties, ISO Technical Report.

Johnson, K. L. (1970) ‘The correlation of indentation experiments’, Journal of the Mechanics and Physics of Solids, 18(2), pp. 115–126. doi: 10.1016/0022-5096(70)90029-3.

Johnson, K. L. (1985) ‘Contact Mechanics’, Journal of the American Chemical Society, pp. 1–17. doi: 10.1115/1.3261297.

Kang, J. (2013) Determination of elastic-plastic and visco-plastic material properties from instrumented indentation curves. University of Nottingham.

Karthik, V. et al. (2012) ‘Finite element analysis of spherical indentation to study pile-up/sink-in phenomena in steels and experimental validation’, International Journal of Mechanical Sciences. Elsevier, 54(1), pp. 74–83. doi: 10.1016/j.ijmecsci.2011.09.009.

Khan, Akjtar S.;Huang, S. (1995) CONTINUUM THEORY OF PLASTICITY. John Wiley & Sons, Inc.

Kleinermann, J.-P. and Ponthot, J.-P. (2003) ‘Parameter identification and shape/process optimization in metal forming simulation’, Journal of Materials Processing Technology, 139(1–3), pp. 521–526. doi: 10.1016/S0924-0136(03)00530-2.

Lee, H., Haeng Lee, J. and Pharr, G. M. (2005) ‘A numerical approach to spherical indentation techniques for material property evaluation’, Journal of the Mechanics and Physics of Solids, 53(9), pp. 2037–2069. doi: 10.1016/j.jmps.2005.04.007.

Leu, D. K. (2011) ‘Evaluation of friction coefficient using indentation model of Brinell hardness test for sheet metal forming’, Journal of Mechanical Science and Technology, 25(6), pp. 1509–1517. doi: 10.1007/s12206-011-0134-4.

Li, Y. et al. (2016) ‘Improvement of predicting mechanical properties from spherical indentation test’, International Journal of Mechanical Sciences. Elsevier, 117, pp. 182–196. doi: 10.1016/j.ijmecsci.2016.08.019.

Mahnken, R. (2002) Theoretical, numerical and identification aspects of a new model class for ductile damage, International Journal of Plasticity. doi: 10.1016/S0749-6419(00)00105-4.

Mesarovic, S. D. J. and Fleck, N. A. (1999) ‘Spherical indentation of elastic-plastic solids’, Proceedings of the Royal Society A: Mathematical, Physical and Engineering Sciences, 455(1987), pp. 2707–2728. doi: 10.1098/rspa.1999.0423.

Njeugna, E. et al. (2016) ‘An Instrumented Macro-Indentation Method for Determining the Mechanical Properties of Coconut Shell (Coco Nucifera of Cameroon)’, Mechanics, Materials Science & Engineering, (July). doi: 10.13140/RG.2.1.1447.3846.

Oliver, W. C. and Pharr, G. M. (1992) ‘An improved technique for determining hardness and elastic modulus using load and displacement sensing indentation experiments’, Journal of Materials Research, pp. 1564–1583. doi: 10.1557/JMR.1992.1564.

Oliver, W. C. and Pharr, G. M. (2004) ‘Measurement of hardness and elastic modulus by instrumented indentation: Advances in understanding and refinements to methodology’, Journal of Materials Research, 19(01), pp. 3–20. doi: 10.1557/jmr.2004.19.1.3.

Olsson, E. and Larsson, P. L. (2013) ‘On the appropriate use of representative stress quantities at correlation of spherical contact problems’, Tribology Letters, 50(2), pp. 221–232. doi: 10.1007/s11249-013-0114-1.

Osgood, W. R. and Ramberg, W. (1943) Description of stress-strain curves by three parameters. Washington, DC, United States. Available at: https://ntrs.nasa.gov/search.jsp?R=19930081614.

Smithells, C. J. (2004) Smithells Metals Reference Book. 8th edn. Edited by W. F. Gale and T. C. Totemeier.

de Souza Neto, E. A., Peri, D. and Owen, D. R. J. (2008) Computational Methods for Plasticity. Chichester, UK: John Wiley & Sons, Ltd.

SWIFT, H. W. (1962) ‘Plastic instability under plane stress’, Journal of the Mechanics and Physics of Solids, p. 18.

Tabor, D. (1948) ‘A Simple Theory of Static and Dynamic Hardness’, Proceedings of the Royal Society A: Mathematical, Physical and Engineering Sciences, 192(1029), pp. 247–274. doi: 10.1098/rspa.1948.0008.

Tabor, D. (1951) The hardness of metals. London.

Tabor, D. (1970) ‘The hardness of solids’, Reviews of Physics in Technology, 1(3), pp. 145–179. doi: 10.1088/0034-6683/1/3/I01.

Taljat, B. and Pharr, G. M. (2004) ‘Development of pile-up during spherical indentation of elastic-plastic solids’, International Journal of Solids and Structures, 41(14), pp. 3891–3904. doi: 10.1016/j.ijsolstr.2004.02.033.

Voce, E. (1948) ‘The relationship between stress and strain for homogeneous deformation’, J Inst Met. doi: 74: 537−562.

Williams, J. a and Dwyer-Joyce, R. S. (2001) ‘Contact Between Solid Surfaces’, Modern Tribology Handbook, 1, pp. 121–162. doi: doi:10.1201/9780849377877.ch3\n10.1201/9780849377877.ch3.

Wriggers, P. (2006) Computational contact mechanics, Computational Contact Mechanics. doi: 10.1007/978-3-540-32609-0.